December 2016

Corrosion of Aluminum Current Collector in Cost Effective Rechargeable Lithium-Ion Batteries

Shengyi Li
University of Wisconsin-Milwaukee

CORROSION OF ALUMINUM CURRENT COLLECTOR IN COST EFFECTIVE RECHARGEABLE LITHIUM-ION BATTERIES

by

Shengyi Li

A Dissertation Submitted in

Partial fulfillment of the

Requirements for the Degree of

Doctor of Philosophy

in Engineering

at

University of Wisconsin-Milwaukee

December 2016

ABSTRACT

CORROSION OF ALUMINUM CURRENT COLLECTOR IN COST EFFECTIVE RECHARGEABLE LITHIUM-ION BATTERIES

by Shengyi Li

The University of Wisconsin-Milwaukee
Under the Supervision of Professor Benjamin Church

Rechargeable lithium ion batteries (LIB) have been widely used as commercial energy storage systems for portable equipment, electronic devices and high power applications (e.g. electronic vehicles). One issue with the commercialized LIB is that expensive, highly toxic and flammable organic solvents are used in the electrolyte and the fabrication process of electrodes. The toxic organic based solvents increase the production cost and lead to significant safety concerns in the event of a battery overcharge or short circuit. The recent development of "green manufacturing" technology allows manufacturers to replace the organic solvents used in the cathode coating process by aqueous based slurries. In addition, the further transition from organic based LIB system to completely aqueous based lithium ion battery (ARLB) has attracted a lot of attention recently because of its potential to significantly reduce manufacturing cost and eliminate the risks and environmental issues associated with the commercialized, organic based lithium ion batteries. Such new aqueous-based technologies often use basic aqueous solutions with high pH value, which brings concerns on the possible occurrence of aluminum current

collector corrosion. The corrosion of aluminum current collector in lithium ion batteries is one of the possible factors that affect the long-term performance and safety of lithium-ion batteries. In this work, the corrosion phenomenon of aluminum current collector in lithium ion batteries that use aqueous-based chemistries is explored experimentally and theoretically. Here, the corrosive aqueous media defined in lithium-ion battery systems includes the aqueous based slurry used in the fabrication of cathode coating, aqueous lithium nitrate electrolyte and aqueous lithium sulfate electrolyte. This research aims to reveal the corrosion behavior, corrosion mechanisms and corrosion kinetics of aluminum in exposure to aqueous environment during the fabrication and service life of aqueous-based lithium-ion battery systems, and shed light on the management of corrosion in the design of cost effective lithium ion batteries.

Corrosion of aluminum can occur during the manufacturing of lithium ion batteries when aqueous-based cathode slurries is used during cathode coating process. The corrosion mechanism of AA1085 in exposure to aqueous based cathode slurry was investigated by surface characterization on aluminum after exposure tests and measuring electrochemical characteristics. In exposure tests, the alkaline pH value of aqueous-based cathode slurries and immersing time were revealed as the principle factors that control the corrosion of aluminum during the cathode manufacturing process. The nickel manganese cobalt oxide active material used in the slurry does not have a direct impact on corrosion of the aluminum current collector. The initiation and evolution of localized corrosion on aluminum are closely related to the formation of galvanic cells between aluminum matrix and intermetallic particles. X-ray photoelectron spectroscopy

confirmed that the pH of cathode slurry was the only factor that influence the surface composition of aluminum. The oxide passive film gradually degraded into hydroxide with the elapsing exposure time. Electrochemical characterizations showed that aluminum electrodes gave remarkably different response to the different pH of test solutions. The time-pH-variant electrochemical response was ascribed to the change of passive film and electric double layer properties.

The electrochemical stability of high-purity aluminum in 2 M Li_2SO_4 and 5 M $LiNO_3$ ARLB electrolytes was evaluated over a range of pH conditions by cyclic voltammetry, linear sweep voltammetry and chronoamperometry. Aluminum presented high corrosion resistance at pH 5, pH 7 and pH 9 within the stability windows of both electrolytes. At the pH 11 condition, 2 M Li_2SO_4 is capable of inhibiting aluminum from pitting, although the inhibiting effect is not sustainable and crystallographic pitting occurs under a continuously applied anodic potential. Aluminum was well passivated against pitting in 5 M $LiNO_3$ electrolyte at pH 11 due to the formation of a thick corrosion product barrier layer. Raman spectra showed the presence of sulfate and nitrate anions on aluminum surface after cyclic voltammetry at pH 11. The chemical adsorption mechanisms of sulfate and nitrate anions on aluminum were proposed to explain the dependency of electrochemical stability of aluminum on pH, anodic potential and type of anions. The applicability of aluminum as current collector in ARLB using the 2 M Li_2SO_4 and 5 M $LiNO_3$ electrolytes was discussed.

The corrosion kinetics of AA1085 in Li_2SO_4 and $LiNO_3$ aqueous rechargeable lithium-ion battery electrolytes at pH 11 under the influence of various experimental variables was studied using chromoamperometry. AA1085 is susceptible to crystallographic pitting corrosion in Li_2SO_4 electrolytes. The rate of pit nucleation and the rate of pitting growth on AA1085 both decreased at higher Li_2SO_4 concentrations or at lower anodic potentials. In $LiNO_3$ electrolytes, AA1085 was passivated against pitting corrosion due to the formation of a thick, uniform corrosion product layer. The repassivation rate was slightly enhanced by increasing the electrolyte concentration and anodic potentials. X-ray photon electron spectroscopy spectra showed the formation of a thin sulfate-incorporated passive film, which comprises $Al_2(SO)_418H_2O$, $Al(OH)SO_4$ and $Al(OH)_3$ on electrode before the occurrence of pitting growth in 2 M Li_2SO_4 electrolyte. The thick corrosion product layer formed in 5 M $LiNO_3$ electrolyte is composed of $Al(OH)_3$ and $AlOOH$. Raman spectroscopy on deionized water, LiOH solution, Li_2SO_4 and $LiNO_3$ depicted changes of solution structure with increasing electrolyte concentrations. The influence of extrinsic factors, including the alkaline solution and the anodic potential, and intrinsic factors, such as the surface chemical adsorption of anions, chemical state of passive films and dissolubility of electrolytes, on the corrosion kinetics of AA1085 in slightly alkaline Li_2SO_4 and $LiNO_3$ electrolytes are revealed.

The intermetallic particles containing Fe and Si in aluminum alloys have electrochemical potentials that differ from that of aluminum matrix, resulting in the formation of galvanic couples and detrimental pitting corrosion. The electrochemical characteristics of AA1100,

surface treated AA1100 with "intermetallic-free" surface, home-synthesized Al_2Fe and $Al_2FeSi_{0.67}$ alloy were measured by potentiodynamic polarization in alkaline solutions with the addition of Li_2SO_4 and $LiNO_3$. In general, intermetallic alloys presented noble corrosion potentials compared to AA1100 specimens. The addition of sulfate anions in the solution does not suppress the selective dissolution of aluminum on intermetallic alloys in 0.001 M and 1 M LiOH solutions, which increases the cathodic efficiency of intermetallic alloys and promotes the galvanic corrosion. The corrosion potential difference is significantly reduced when 2 M $LiNO_3$ is added into the alkaline solution. Meanwhile the anodic dissolution rate that corresponds to the preferable dissolution of Al also decreases. Raman spectra revealed that the inhibiting effect of $LiNO_3$ on selective dissolution of aluminum is due to the formation of Fe_3O_4 passive film above the corrosion potential. the cathodic polarization curves showed that the intermetallic alloys sustain higher cathodic current than AA1100 and surface-treated Al. The magnitude of cathodic current density measured on the electrodes follows the following order: $Al_2Fe>Al_2FeSi_{0.67}>AA1100>$surface-treated AA1100. The change of composition and structure on the intermetallic surface during anodic polarization influences the selective dissolution process, the passivity status and in turn affects the cathodic efficiency of the intermetallic.

TABLE OF CONTENTS

LIST OF FIGURES

xiii

LIST OF TABLES

LIST OF NOMENCLATURE

R	Resistance
L	Inductance
Q	Capacitance
C_{eff}	Effective capacitance
R	Resistance
ω	Frequency
$E^0_{H^+/H_2}$	Standard hydrogen potential
$E^0_{O_2/H_2O}$	Standard oxygen potential
E_{H^+/H_2}	Theoretical hydrogen evolution potential
E_{O_2/H_2O}	Theoretical oxygen evolution potential
E_O	Oxygen evolution potential
E_H	Hydrogen evolution potential
J_c	Current corresponds to the charging of the electric double layer
J_{gr}	Current corresponds to the growth of passive film layer on aluminum due to repassivation
J_{diss}	Current corresponds to the dissolution of passive film or electro-dissolution of metal matrix
J_{pit}	Current corresponds to the rapid dissolution of aluminum by pitting
t	Time
A	Rate of pit growth coefficient

ACKNOWLEDGEMENTS

I would like to express my deep appreciation and gratitude to my advisor, Professor Ben Church for his patient guidance, support and mentorship throughout the course of my studies at UW-Milwaukee. His profound knowledge and encouragement has made my PhD study a learning and thoughtful and experience. I'm truly fortunate to work on research together with him.

I would also like to thank my committee members, Professor Pradeep Rohatgi, Professor Nidal Abu-Zahra, Professor Junhong Chen and Professor Ilya Avdeev for serving on my doctorial committee. Their kind guidance, thought-provoking suggestions have helped me complete my dissertation successfully.

I'd like to give special thanks to Professor Deyang Qu and his post-doc Dong Zheng from UWM Mechanical department for their assistance in ICP set ups and analysis. I'm grateful to Mr. Steve Hardcastle from UWM AAF for his assistance in XPS analysis and Professor H.A. Owen from UWM Biology department for her guidance on SEM and BSE imaging. Their valuable input has led this more research insights into this work.

I am grateful to my dear colleagues and friends for sharing the time at UW-Milwaukee. Particularly, I'd like to thank Yangping Sheng, Aruna, P Wanninayake, Yihan Xu and Robert Lee Hanson for their encouragement and assistance in work.

At last, I would like to express my greatest appreciation to my wife and my parents, for their unconditional love and support to me in this wonderful journey.

CHAPTER 1 Introduction

1.1 Background and motivation

Aluminum is the most abundant metal element in earth and it is also the second most consumed metal in the world. Aluminum and its alloys are well known for lightweight, high reflectivity, high electrical and thermal conductivity.[1] A thin layer of oxide passive film is naturally formed on aluminum surface, protecting aluminum from corrosive media attack. These unique properties make it a perfect material for both conventional and novel applications.

Depending on the amount of impurities, aluminum is classified into extreme high purity aluminum and commercial purity aluminum (primary aluminum). The aluminum purity level affects many of its properties especially upon electrical resistivity and thermal conductivity.[1] In lithium ion batteries (LIB), commercial grade aluminum is extensively used as the current collector for lithium oxide cathode electrode. Compared to stainless steel, nickel mesh etc., it has many advantages, such as relatively low cost, high electronic conductivity and availability as high purity thin foils or plates.[2] The current collectors has to be electrochemically stable in contact with the cell components over the operating potential window of the battery. In most electrolytes, aluminum is also stable up to 4.5V vs. Li+/Li. Aluminum may also be coated on insulating substrates by physical deposition, which allows much less use of metal. Thus commercial aluminum is commonly considered as the material of choice for high voltage (>3.5 V) lithium ion batteries.

In lithium ion batteries, current collector is not involved in the lithium intercalation/de-intercalation reactions so it is considered as an inactive component, which is among the many factors influencing the cell gravimetric energy densities. Recently, the studies

carried out on current collectors are mostly focused on its degradation in contact with various chemistries of LIB components. The standard redox potential for Al/Al^{3+} is -1.676V (SHE) in acidic solutions.[2] Although aluminum is expected to be thermodynamically stable due to a thin layer of oxide passive film, it may subjected to corrosion during the continuous contact with complex chemistries in LIB systems. The degradation of Al current collector may result in a series of problems, including adversely increase the electrical resistance, generate corrosion products that contaminate active materials, leading to the attenuation of the battery's electrical performance, life or even safety.

The development of renewable energy requires new energy storage systems with high energy density, high cycling rate, high round-trip efficiency, long service life, enhanced safety performance and reduced manufacturing cost. To meet these requirements, the materials selection and materials design is important during the development of the new technologies. Aluminum, as the most abundant metallic material, with lightweight, low cost, high conductivity, corrosion resistance and considerable mechanical strength, has been widely adopted as conductive substrate material in energy storage systems. Any sudden failure or long-term degradation of the aluminum current collector is big concern because it'll adversely affect the electrical performance, capacity, life, and safety. The factors that might bring such issues include: (i) the electrical resistance increases to a point that the continuity is lost. (ii) the active electrode materials are attacked by the corrosion products. (iii) introduction of contaminants that will react with active materials.[3] Understanding the electrochemical stability, corrosion mechanisms and corrosion kinetics of current collectors in the service life environment it's exposed to, helps ensure the proper use and selection of aluminum and its alloys, avoid possible catastrophic

failure caused by the corrosion in cost-effective lithium ion batteries. This study is also rendered very necessary by the vast use of aluminum and its alloys in aerospace, automotive and structural applications. The objective of this work was to understand how the continuity of aluminum current collector is affected by aqueous based cathode slurry and ARLB electrolytes, and if the reliability and the service life of batteries would be compromised. The corrosion behavior and explain the corrosion mechanism of current collectors exposing to aqueous slurries and electrolytes was investigated. As it is very difficult to conduct experiment process in functional cells, simulated electrochemical conditions were applied without considering more complex situations with the active electrode materials involved. Excess electrolyte is used to minimize the influence from effects from concentrated corrosion product but notably it might exaggerate the effects of aqueous solutions.

1.2 The role of structural and compositional features on Al corrosion

1.2.1 The protective surface passive film

Although aluminum is one of the most active metals (-1.67V vs. SHE), the oxidation rate is extremely low at room temperature or even up to 600 ℃.[4] This is due to the fact that a layer of oxide passive film is naturally formed on aluminum surface under ambient conditions, which is so called passivation phenomenon. Passivation plays important role in various technological applications, such as catalysts, sensors, lubrication, dielectrics and corrosion protection. From a corrosion point of view, passive films should be stable or exhibit very low rate of dissolution in the passive potential range. The break down potential for the passive films should be as high as possible. The oxide layer formed on aluminum is non-uniform, very thin, only a few nanometers thick.[5] It is crucial for the corrosion resistance property of aluminum. On aluminum alloys, this

protective film is, however, very susceptible to pitting corrosion due to the existence of intermetallic particles, which leads to accelerated corrosion of underlying aluminum matrix.

J. D. Baran et al. described that the reason for the limited thickness of aluminum passive film is due to the decreased oxygen absorption energy, which prohibit the supply of oxygen molecules.[4] The oxidation of aluminum at low temperature relies on an electrochemical mechanism as opposed to thermal activation for high temperature oxidation. Aluminum oxidation starts with the dissociative chemisorption of O_2 from gas phase and charge transfer from metal to the oxygen. The subsequent passive film growth involves the absorption and dissociation of oxygen on bare aluminum metal surface. Upon the oxide film is covered on aluminum surface, cations and anions as well as electrons transport through the growing oxide film. The ionic diffusion through the oxide film is controlled by the electric field established by tunneling electrons due to the potential difference across the passive film (Mott potential). As the rate of electron transport through the oxide film decreases exponentially with the film thickness. The charge neutrality of coupled currents of electrons and cations means that the thickness of oxide film is limited at low temperatures.

The aluminum oxide layer formed at low temperature is amorphous alumina film. Bulk Al_2O_3 is an insulator with a band gap of 8-9 eV. The passive film on aluminum exhibits a band gap of 3 eV. During the oxidation process oxygen anions are close packed with the aluminum cations over the octahedral and tetrahedral interstices. The passive film shows a deficiency of Al cations thus it is considered that the oxide-film growth is limited by the cation migration under the influence of Mott potential V_M. The oxide film growth rate is described by:

$$\frac{dL}{dt} = \Omega \ n \ \nu \ \exp(\frac{-U + qaV_M/L}{kT})$$

4

Where L represents the film thickness at time t, Ω is the volume of oxide film formed per transported cation, n is the number of cations per unit area that jump through the diffusion barrier U, q is the charge of migrating ions, a is the distance between two adjacent potential minima, ν is the attempt frequency for ion migration, k is the Boltzmann constant and T is the temperature. The effective limiting thickness of the oxide film L_{lim} is defined as when $\frac{dL}{dt} \leq 10^{-5}$Å/s, which means the oxide growth rate is less than one oxide monolayer per 10^5 s. The limiting oxide layer thickness L_{lim} is given by,

$$\frac{1}{L_{lim}} = -\frac{kln(10^{-15}/\Omega\ n\ \nu)}{qaV_M}T - \frac{U}{qaV_M}$$

Generally, the Mott potential V_M, is determined by the potential difference between the metal-oxide work function Φ_m and the oxygen-oxide work function Φ_o. $V_M = (F_m - F_O)/e$, where e is the electron charge.[4] In a recent work of Na Cai et al., it is described that the mobility of Al cations is affected by the oxygen pressure, thus influence the overall oxidation kinetics.[6] Depending on various environmental chemistries and conditions, the passive film formed on aluminum may consists of oxides, oxy-hydroxides, hydroxides.[7] The role of aluminum intermetallic particles

As the major impurities in pure aluminum, Fe and Si are usually dissolved in aluminum matrix or forms intermetallic phases. These particles are formed during solidification and are not dissolved in the following thermal-mechanical processing.[8] Intermetallic in aluminum are either natural impurities or intentionally developed to achieve desired mechanical properties. Because some particles do not play a pivotal role in the mechanical properties of aluminum alloys, the precise mechanical properties of these particles are still not well known. However, it was described that the existence of these impurities results in high hardening rate in aluminum.

1xxx alloys contain Al_6Fe and Al_3Fe as natural impurities. Some intermetallic adversely affects pitting resistance, such as intermetallic with Cu and Fe in 2xxx and 1xxx alloys. The influence of the intermetallic primarily depends on the potential difference between the particle and the matrix metal in a solution. Intermetallic that is more electrochemically stable than matrix act as cathode and the matrix metal undergoes anodic dissolution.[9] In high-purity aluminum, Al-Fe and Al-Fe-Si are identified as the primary intermetallic particles. There are three equilibrium phases in Al-Fe-Si ternary phase diagram, they are Al_3Fe, α and β phase.[10] But over then different metastable phases could be formed under actual solidification conditions. The composition, size, distribution and volume fraction of intermetallic phase will affect the mechanical properties of foils significantly. β phase transforms into α phase during intermediate annealing, resulting in a favorable decrease of particle size. The precipitation formed during annealing also contributes to an impurity concentration change in aluminum matrix, which at the same time results in matrix lattice parameter change.

The alloying elements in intermetallic particles make them electrochemically different from the surrounding phases. The electrochemical response and activity of most metals and alloys are remarkably different with the change of solution pH due to the existence of intermetallic particles.[11] It results in ramifications in the corrosion morphology on aluminum alloys with various types and composition of intermetallic particles, which is known as galvanic corrosion. Galvanic corrosion is ranked as the leading cause of all corrosion experienced by aluminum in electrical applications. It occurs when two metals come to direct contact with one another while immersed in an electrolyte. The difference in electromotive force between metal

and its intermetallic phase results in current flow from the cathode to the anode, which lead to the oxidation of anode.

In near neutral solutions, the pitting corrosion is influenced by the intermetallic particles. There are mainly two types of corrosion that were detected, one is called "circumferential", appear as a pit around more or less inert particle, with the corrosion happened mostly in the matrix (trenching).[12] Another type of pit is grown deep in matrix and may contain some intermetallic particles remnants inside, which is caused by the preferable dissolution of the intermetallic particle. Intermetallic affects the homogeneity of passive film on aluminum and serve as cathodic sites for pit nucleation. The intermetallic particles dissolve selectively and the remnants after the particle dissolution such as Fe and Cu, are even more cathodic than the intermetallic. At a potential below the pitting potential, the deterioration of passive film properties results in the rupture of passive film and produces metastable pits. During pit growth, the interface events influence growth process, while the physical and chemical properties of passive film influence the initiation of pits but play a secondary role in pit growth. Noble intermetallic particles act as cathodic sites even when the electrolyte is deaerated, reduction of residual oxygen and a low level of hydrogen evolution occur and cause anodic dissolution of Al adjacent to the intermetallic particles. The magnitude of the corrosion potential difference between the intermetallic and aluminum matrix can be used to estimate the corrosion behavior of aluminum alloys. But the corrosion potential is not adequate for the understanding of corrosion mechanisms. Additional information on the electrochemical behavior, the structure of the alloy is required.

The influence of the Al_3Fe intermetallic on aluminum pitting was studied in prior works. Rajan et.al reported that the anodic and cathodic reactivity of Al-Fe alloys are both dominated by the distribution of Al_3Fe intermetallic particles, even the Fe is at a very low compositional level of 0.04%.[13] The greater the number of intermetallic particles, the higher the cathodic reactivity. The cathodic reactivity increases with the iron content of the alloy. Nisancioglu reported that at a potential close to the corrosion potential, aluminum in Al_3Fe preferably dissolves and the surface of Al_3Fe became rich in iron.[14] A transient behavior for the corrosion potential of Al_3Fe during the first 30-200 min of immersion was found in 0.1 M NaOH. A protective layer of Fe_3O_4 formed on the intermetallic. The iron rich layers are highly porous, which can act as catalytic sites for oxygen reduction. The presence of Mn or Si in the phase reduce the effect of iron on both anodic and cathodic reaction rates. In general, the results show that Al_3Fe and Al-Fe-Si presents an increased cathode activity due to the selective dissolution of Al. Hassan et. al reported that Al, Al6061 and Al-Cu alloy presented different corrosion resistance in alkaline solutions, which is associated to the effects of alloying elements. The high percentage of Cu (4.8%) in the Al-Cu alloy decreased the corrosion resistance of the alloy. In Al6061, the presence of Mg and Si leads to the formation of Mg_2Si phase, which has no pronounced influence on electrode potential.[15] The general effect of Mn and Si in intermetallic is to reduce both the anodic and cathodic currents significantly due to passivating effect. The addition of Si reduces the anodic oxidation peaks, reduces the rate of hydrogen evolution, and shifts the corrosion potential to more negative potentials. [14]

1.3 Aqueous based lithium-ion battery system

Rechargeable lithium ion batteries have been widely used as commercial energy storage systems for portable equipment, electronic devices and higher power applications (e.g. electronic vehicles). Due to its advantages in superior performance, flexibility in design and high energy density etc., LIB has been considered as the best option for energy storage system used in electric vehicle (EV) or hybrid electric vehicle (HEV).[16] Beck and Ruetschi proposed the "three E" criteria as the requirements for good energy storage systems, which highlights energy, economics and environment. Specifically, the energy storage system should have high energy density (high energy content with respect to unit weight and volume), economic (with low fabrication costs and long cycling life), environment (safe to be used, nontoxic and high reliability).[17]

The reason that lithium ion batteries could work is because of the ability of Li ions to be inserted or extracted from positive materials. Lithium atoms are inserted into a host solid as guest atom with only slight and reversible changes in the host material. The host materials are usually layered material like graphite or tunnel structure compounds e.g. $LiMnO_4$ and $LiFePO_4$. The intercalation is happened because of the lowered chemical potential of lithium during its insertion into the host material. When the cell is discharged, the intercalated lithium dissociates into ions and electrons move to the positive electrode through the electrolyte and the electrical circuit. The ions and electrons meet at the surface of host material and they will be intercalated into the material. The cell voltage can be calculated by the difference between the potential of Li in intercalation hosts divided by the charge.[18]

1.3.1 Advantages of aqueous based lithium ion battery system

During the fabrication of lithium-ion battery positive electrodes, solid active materials are blended with binders, solvent, and conductive carbon. The slurry paste is then coated on aluminum foil, dried and compressed to generate a cathode coating of controlled loading of active materials. The commercial lithium-ion batteries employ an organic solvent, n-methylpyrrolidone (NMP) to prepare the slurry. But for the concerns of processing requirements, production cost and environmental issues, manufacturers may move away from organic NMP solvents and instead utilize aqueous based slurries. The most commonly used aqueous binder is the aqueous emulsion of styrene butadiene rubber (SBR) blended with water-soluble sodium carboxymethyl cellulose (CMC) [19]. The use of aqueous slurry brings distinct advantages for lithium ion battery manufacturing, such as elimination of toxic, volatile organic binder, and lower production cost.

Organic electrolyte is extensively used in commercialized lithium ion batteries. In commercial lithium ion batteries, the most commonly used electrolyte is derived from solutions of lithium salt in non-aqueous solvents, such as alkyl carbonates or solvent blend.[20] However, the organic based electrolyte system has a lot of drawbacks. First of all, the organics are highly toxic and flammable, which may cause safety hazards if the battery is overcharged or self-circuited. Besides, the ionic conductivity of the organic electrolyte is poor, which is two orders of magnitude lower compared to aqueous electrolyte. Generally, the conductivity of organic electrolytes dissolving $LiPF_6$ is 20 mS/cm at room temperature, however the conductivity of aqueous based electrolytes are close to 1 S/cm. Due to the limited conductivity, the electrode in organic based lithium ion battery must be thin. More importantly, the fabrication cost of organic

based LIB is high. These drawbacks have limited its application in large-scale energy storage systems.[21]

In such scenario, the possibility of producing lithium ion battery with aqueous based system has been considered. In 1994, Dahn's group first introduced the concept in which VO_2 is used as negative electrode and $LiMn_2O_2$ as positive electrode in 5M $LiNO_3$ aqueous electrolytes.[18] Aqueous electrolytes own several advantages over organic electrolytes. They are non-flammable thus offers much better stability and safer performance. Electrolyte of water solution and the separator sheets used are both much cheaper compared to organic electrolytes. In addition, the conductivity of aqueous electrolytes is significantly higher, which brings higher rates and lower voltage drops due to electrolyte impedance. It has attracted wide attention because its good cycling performance and super-fast charge performance, which can be comparable with filling gasoline for engine cars. One challenge in aqueous based lithium ion battery technology is the H_2/O_2 evolution reactions in aqueous electrolyte. It is known that capacity of the electrode material should be used as much as possible before electrolyte decomposition. But the evolution of H_2/O_2 inevitably happens at full charge stage.[22] It results in pH change nearby the electrode and affects the stability of the electrode materials. In organic electrolyte systems, although it was reported that the decomposition of electrolyte occurs at high voltage, a protective film (SEI layer) is formed between the active material and the electrolyte and reduce the further decomposition. But there are no such protecting mechanisms in aqueous based LIBs.[23] Due to the limited operating potential range within the electrochemical window of water, the main disadvantage of aqueous lithium ion battery is the low energy density compared to the conventional lithium ion battery.

1.3.2 Stability window of aqueous electrolytes aqueous based lithium ion battery

Theoretically, an aqueous lithium-ion battery can be assembled by combining a lower potential lithium-accepting anode and a higher potential lithium-source cathode within the O_2/H_2 evolution potential range.

From basic thermal dynamics, the equilibrium of H^+ and H_2 in aqueous solution is described as the following equation:

$$2H^+ + 2e^- \rightleftharpoons H_{2(g)} \uparrow$$
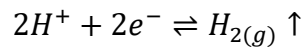
In high pH solution, the equilibrium relationship is as follows:

$$2H_2O + 2e^- \rightleftharpoons H_{2(g)} \uparrow + 2OH^-$$
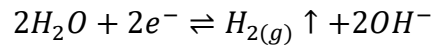
Thus, for hydrogen evolution, the dissociation potential can be illustrated by Nernst equation:

$$E_{H^+/H_2} = E^0_{H^+/H_2} + \frac{RT}{nF} ln \frac{[H^+]^2}{P_{H_2}}$$

In equilibrium condition at 25°C, the equation becomes:

$$E_{H^+/H_2} = E^0_{H^+/H_2} - 0.059 \text{pH}$$

The decomposition of water into hydrogen is favored when the potential is lower than the hydrogen evolution potential. But when potential becomes more positive or noble, water will decompose into its other constitute oxygen, as illustrated in equations for the acid form of the process,

$$O_2 + 4H^+ + 4e^- \rightleftharpoons 2H_2O$$
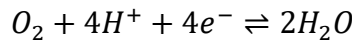
A Nernst equation is used to describe the potential in standard conditions of temperature and oxygen partial pressure of value unity.[24]

$$E_{O_2/H_2O} = E^0_{O_2/H_2O} + \frac{RT}{nF} ln(P_{O_2}[H^+]^4)$$

$$E_{O_2/H_2O} = E^0_{O_2/H_2O} - 0.059\text{pH}$$

The potential range of the stability window is shown in figure 1.1. According to the operating potential range, the possible candidate materials for cathode and anode electrodes in aqueous based lithium ion battery are shown in the following graph (figure 1.2).
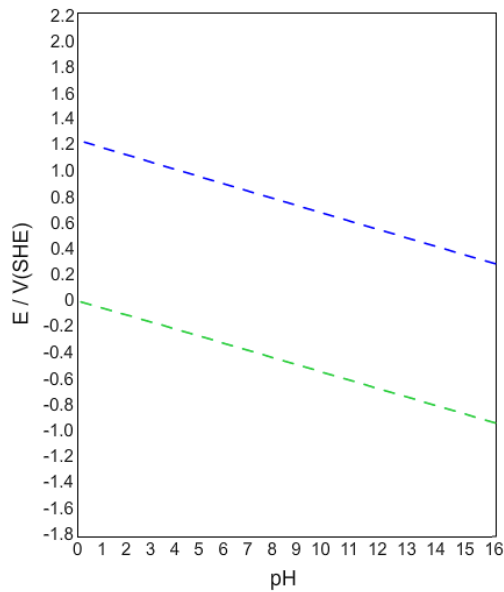
Figure 1.1 Calculated stability window of water with respect to pH values.
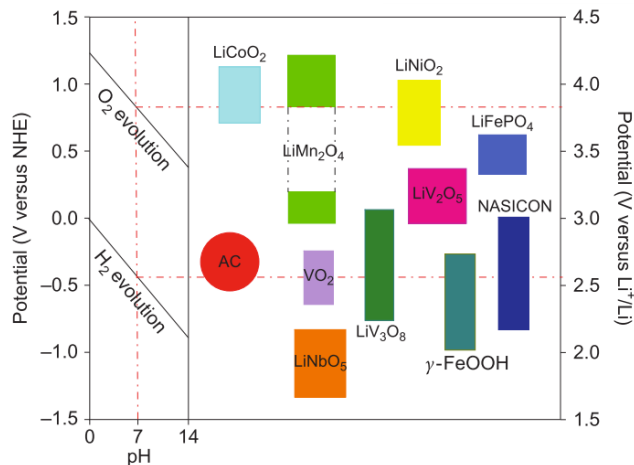
Figure 1.2 The intercalation potential of some electrode materials that could possibly be used for aqueous lithium-ion batteries. Left: theoretical O_2/H_2 evolution potential versus NHE for different pH in 1M Li_2SO_4 aqueous solution. Right: lithium-ion intercalation potential of various electrode materials versus NHE and Li/Li$^+$.[25]

13

Previous study shows that materials with voltage versus Li/Li$^+$ higher than 3.3 V are generally stable. The intercalated potential of lithium-ion is below 3.3V versus Li/Li$^+$ when being as negative or anode materials. As the aqueous based LIB operates in air, the intercalated lithium may react with H_2O and O_2 in the following way,

$$Li(intercalated) + \frac{1}{4}O_2 + \frac{1}{2}H_2O \Leftrightarrow Li^+ + OH^-$$
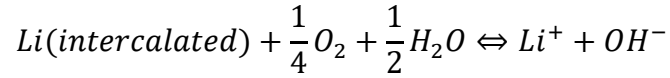
The potential of a LIC, V(x) can be calculated with the equation: $V(x) = -\frac{1}{e}(u_{Li}^{int}(x) - u_{Li}^0)$,

Where $u_{Li}^{int}(x)$ is the chemical potential of intercalated Li in cathode, u_{Li}^0 is the chemical potential of Li in Li metal.[18]

1.3.3 Recent progress on development of aqueous based lithium ion batteries

In 1999 Mohan Rao et al. reported for the first time that the lithium deficient $Li_{1-x}NiO_2$ has a chemically reversible electrochemical proton intercalation in alkaline aqueous electrolytes. It is also reported that the electrochemical stability of $LiCoO_2$ is dependent on the hydrogen ion concentration a lot. The cathode material is stable when pH is less than 9 or when it is higher than 11. The electrochemical performance of $LiNi_{1/3}Co_{1/3}Mn_{1/3}O_2$ in aqueous solution is also similar to that of $LiCoO_2$. Yuan et al. studied the electrochemical behavior of $LiMnO_4$ electrodes in 2M Li_2SO_4, 1M $LiNO_3$, 5M $LiNO_3$ and 9M $LiNO_3$ aqueous electrolytes. The results show that the $LiMnO_4$ electrode in 5M $LiNO_3$ electrolyte shows good electrochemical performance in terms of specific capacity, rate ability and charge/discharge cyclability.

Recently Mentus et al. reported that the addition of vinylene carbonate into aqueous $LiNO_3$ solution effectively improved the cycle life of $Li_{1.05}Cr_{0.1}Mn_{1.85}O_4$ in aqueous electrolyte solution. Nurhaswani alias described the intercalation of lithium ions for carbon coated $LiFePO_4$

in an aqueous lithium ion battery. The electrochemical behavior of LiFePO$_4$/C vs. air electrode as counter electrode was also evaluated in a 5M LiNO$_3$ solution.[26]

Riccardo Ruffo et al. reported that lithium insertion and extraction can occur in LiCoO$_2$ in LiNO$_3$ aqueous solutions. With a concentration of 5 M LiNO$_3$, fast kinetics and good cycling behavior at high rates were found.[27] In the above aqueous based lithium ion battery research, instead of aluminum, nickel mesh, stainless steel mesh are applied as the current collectors. The possible reason is due to the severe degradation of aluminum with the adding of aqueous based electrolyte.

1.4 Corrosion of aluminum current collector in lithium ion battery

Corrosion is typically defined as the deterioration of metals. In a simple term, corrosion is the inherent tendency of a metal to revert from processed, metallic state into more nature state. For example, iron and steel tends to combine with other elements to return to their lowest energy states. Generally, the corrosion process can be described as chemical reaction or electrochemical reaction between metal and the contacting media, which leads to loss of material and its properties. Corrosion results in wasting away of materials or sudden failure of metal components so it has great impact on economy. In USA, the cost of corrosion on economy is in the vicinity of 3-4% of Gross National Product. These costs are possible to be reduced by application of broader materials design and corrosion protection technologies. The primary methods for protecting material from corrosion include careful material selection, coating, inhibitors, cathodic protection and improvement on part designing.

1.4.1 Requirements for current collectors in lithium-ion battery

Current collector is not involved in the oxidation/reduction battery reaction thus it is considered as inactive mass and volume in lithium ion batteries. A few properties are required for material to be used as qualified current collector. First, to achieve high gravimetric volumetric energy densities, current collectors that are thinner, lighter with compatible mechanical strength are usually preferred. The shape and mechanical property requirements might be costly depends on the material selected and the processing method. Secondly, within the entire operating potential, current collector must be chemically and electrochemically stable. Ideally current collector should not react with any other components in the battery. Third, it has to be adhesive to cathode mix, including the cathode material, binder and conductive material.[2] Evaluation on the stability of current collectors is usually carried out on bare current collectors in direct contact with media using electrochemical methods. Various methods, such as EIS, cyclic voltammetry and potential step measurements have been applied in these studies although there is no standard upon the evaluation methods.

A. H. Whitehead et. al[2] reviewed the materials that haven been studied and used for cathode electrode in lithium based batteries. In the design of these battery devices, a current collector is used to make current flow between electrodes. Most of the materials studied were metallic, as listed in figure 1.3. Some metallic materials in the table are not suitable as current collector due to low conductivity, high cost and instability. A rough comparison of the weight-conductivity-cost of these materials is presented in table 1.1.

Figure 1.3 Elements that have been investigated as candidate materials for cathode current collector in lithium based cells.

Until now aluminum is considered as the best candidate materials as current collectors for cathode compared to other materials such as Ni, stainless steel, Ti etc. From thermodynamic basics, aluminum will corrode during battery cycling because the standard electrode potential of aluminum (1.39V vs Li/Li$^+$) is lower than the operating potential of the cathode electrode. Due to the formation of passive film, however, aluminum is kinetically stable in many conditions. Aluminum could withstand without corrosion until high voltage. However, it could not be used as anode current collector because of its reaction with lithium at potentials near the intercalation potential.

Iwakura et al.[28] compared the electrochemical stability of different metal foils (Al, Cu, Fe, Ni SUS304 and Ti) in 1M solution of LiClO$_4$ and EC/DMC (1:1) electrolytes using cyclic voltammograms and EIS. The anodic current on Al and Ti foils are both very small over the measured voltage range compared to Fe and Cu in the electrolytes. The anodic current on aluminum current collector is also correlated with the impurity level and there is a proportional relationship between the current and impurity level. The content of metal ion in the electrolytes were examined after polarized at 4.5V vs Li/Li$^+$ for 10h. Detectable amount of metal ions was only found on Fe foil, which indicates the deterioration of Fe electrode. The study also showed

that the content of aluminum ion after the polarization test increases with higher impurity levels. Aluminum of different purity level, from 96.9% to 99.9% was tested in $LiClO_4$/EC/diethyl carbonate electrolyte. Aluminum with Fe, Mg, and Mn as impurities showed higher chronoamperometric current compared to aluminum with higher purity level. Thus it draws to the conclusion that electrochemically aluminum with high purity is the most suitable material as current collector for the positive electrode.

Table 1.1 Comparison of conductivity-weight-cost of possible materials used for current collector in lithium-based battery.

Material	Relative conductivity per unit volume	Relative Conductivity per unit mass	Relative conductivity per unit cost
Ag	1.05	0.9	0.01
Cu	1	1	1
Au	0.7	0.33	0.00008
Al	0.4	1.3	2
Mo	0.31	0.27	0.01
W	0.29	0.13	0.02
Zn	0.28	0.36	0.8
Ni	0.24	0.25	0.05
Fe	0.17	0.2	2
Pt	0.16	0.067	0.000008
Cr	0.13	0.16	0.05
Ta	0.13	0.072	0.001
304SS	0.1	0.1	0.1
316SS	0.1	0.1	0.07
Ti	0.04	0.079	0.02
SiC	0.012	0.032	0.001
Mn	0.009	0.01	0.01
C pyrolytic graphite	~0.007	~0.03	—
C graphite	~0.0003	~0.0012	~0.0005
C black	~0.00001	~0.00004	~0.00002

Corrosion of aluminum may occur when it is exposed to electrolytes or electrolyte solvents in lithium ion batteries. Current collector is assumed well protected when cathode material is coated on current collectors, but the cathode material is manufactured into us structure intentionally to increase the cathode/electrolyte interfacial area so intercalation and deintercalation of lithium ions can proceed during the discharge/charge cycling. The localized corrosion of current collector is also ascribed to the through thickness porosity.[29] Although the air formed aluminum oxide passive layer is somewhat protective, it is not capable of protecting aluminum against oxidation at high potentials. For instance, in aqueous solution of 1 M $NaNO_3$, KSCN, and 1 M NaCl, pitting corrosion of aluminum was found to start at 5.0V, 4.5V and 2.6V respectively. The passive layer may not form or dissolved under some conditions. Aluminum is found to dissolve above 3.7 V vs Li/Li^+ in $LiAlCl_4/SO_2$. Passive film may also form and be stable in anhydrous organic solvents, such as $LiBF_4$ or $LiClO_4$ in ethylene carbonate (EC)/propylene carbonate (PC) with $LiMn_2O_4$ as the cathode.[30]

1.4.2 Factors that influence aluminum corrosion in non-aqueous based lithium-ion battery

High reliability and longer service life is required for advanced lithium ion batteries. For long-term applications, the degradation of cell materials has been an issue because of its possibility of adversely affecting the electrochemical performance, capacity, life and safety. Corrosion of aluminum current collector in lithium ion batteries is considered to be a factor that affects the long-term stability of lithium-ion batteries. The degradation of Al current collector, especially localized corrosion, may greatly affect the calendar life and cycling performance of the batteries.[31] The corrosion of current collector cause many problems: (i) the corrosion passivates the cathode active material, (ii) the non-soluble corrosion products increases the

electrical resistance, (iii) soluble corrosion products contaminate the electrolyte thus increase self-discharge rate and (iv) Al^{3+} ions result from anodic dissolution migrate into the cell and reductively deposit on anode.[31]

Generally, the corrosion of aluminum current collector may be caused by electrochemical reactions between aluminum and other components in the battery, such as the electrolyte solvent, lithium salt and the cathode active materials. A lot of studies have been done on corrosion of aluminum current collector in organic based lithium ion batteries. The intrinsic corrosion resistant properties of aluminum are usually evaluated in simulated electrochemical conditions that are not encumbered by more complex conditions with the presence of active electrode materials. The corrosion of aluminum was extensively evaluated in non-aqueous LIB system with different combination of electrolyte and electrolyte solvents.

(i) Effect of electrolyte salt on corrosion of aluminum current collector

Most of the commercial lithium-ion battery use $LiPF_6$ as electrolyte salt. Corrosion of aluminum current collector due to $LiPF_6$ salt was detected in many studies. One possible mechanism for the aluminum corrosion in $LiPF_6$ contained electrolytes is proposed to be crevice corrosion ascribed to the cathode coating. The ratio of surface area of metal inside the crevice and the volume of solution in the crevice is closely related to the severity of corrosion.[32] The inevitable existence of traceable amount of water in $LiPF_6$ was also proposed to be the cause of corrosion problems. PF_6^- can react with trace water and generate HF, which react with the active materials thus bring in more water and also continuously corrode aluminum current collector.

Krause et al reported very high corrosion rates of aluminum was found in PC electrolyte containing $LiCF_3SO_3$ and $LiN(CF_3SO_2)_2$ salts when aluminum is potentiostatically polarized at

+4.2V. H. Yang et al.[33] further investigated the stability of aluminum current collector in propylene carbonate (PC) solutions containing 1M of different lithium salts with electrochemical quartz crystal microbalance (EQCM). The mass of aluminum electrode and the charge transfer involved in the corrosion process was measured as a function of potential and time. The results showed that aluminum corrosion occurred in PC containing $LiN(CF_3SO_2)_2$, $LiC(CF_3SO_2)_3$, and $LiCF_3SO_3$. In $LiPF_6$ or $LiBF_4$ contained electrolytes, corrosion barely happens due to the formation of protective film. Anodic polarization tests in EC/DME electrolyte showed that the corrosion resistance of aluminum current collector in contact with different salts ranks in the following order: $LiCF_3SO_3 < LiN(SO_3CF_3)_2 < LiClO_4 < LiPF_6 < LiBF_4$.

The reason for the lower corrosion rates of aluminum in $LiPF_6$ and $LiBF_4$ is probably due to the alternation of passive films by electrolyte salts. It was proposed that the stabilizing effect of salt is due to the predominant absorption of Li and P on aluminum surface in $LiPF_6$ contained electrolyte. However, in some studies it was described that the passive film is altered by F species. Behl et al. reported that fluorides in $LiPF_6$ and $LiBF_4$ might stabilize aluminum in Li-ion battery electrolytes. It was reported that aluminum is passivated in electrolyte containing $LiClO_4$ and $LiPF_6$ salts.[31] By electron spectroscopy for chemical analysis, a layer of compound containing F is found on the foils in $LiPF_6$/EC/DEC electrolyte, providing better protection compared to $LiClO_4$. It was believed that formation of AlF_3 layer happens due to the decomposition of $LiPF_6$ or $LiBF_4$ salts in trace water. In $LiCF_3SO_3$/PC, a trace of HF results in the formation of AlOF and AlF_3 formed on surface, which remarkably improve the corrosion resistance. In EC/EMC electrolytes with different salts, the ranking of corrosion resistance of aluminum is found to be LiBOB (lithium bis(oxalate)borate)$>LiBF_4>LiPF_6>LiN(CF_3SO_2)_2$,

21

which suggests that P and B species deposition offers more stability for aluminum compared to F species.[2,34] Research was also carried out on evaluating the stability of aluminum passive film in LiTFSI contained electrolytes. Due to the acid-base property of LiTFSI and the stereochemistry of the anion, it lowers the stability of aluminum.[35]

(ii) Effect of cathode materials on corrosion of aluminum current collector

The extent of aluminum corrosion is influenced by the type of cathode active material in LIB. For instance, compared to $LiFePO_4$, $LiNi_{1/3}Co_{1/3}Mn_{1/3}O_2$, higher rates of corrosion occurred on $LiMnO_2$ cathodes.[32] It was reported that severe corrosion was detected on aluminum foils in $LiMnO_2$ and $LiFePO_4$ cathodes. Comparable less corrosion is found on $LiFePO_4$ electrode because the operating voltage is lower than that of $LiMnO_2$. The reason still relies on the corrosive electrolyte salts. $LiPF_6$ is expected to decompose more at higher voltage thus higher operating voltage will deteriorate aluminum during the long term battery cycling.

(iii) Effect of electrolyte solvent

J. W. Braithwaite et al.[3] studied the corrosion of aluminum current collector in 1:1 propylene carbonate and diethylene carbonate (PC:DEC) electrolyte and 1:1 mixture of ethylene carbonate and dimethyl carbonate (EC:DMC) with 1M $LiPF_6$ solvent. After 40 cycles, both general corrosion and scattered localized corrosion are found on aluminum surface in both electrolytes. Higher rate of corrosion occurs in EC:DMC electrolyte condition. Under increased charge potential condition, corrosion resistance of aluminum is found decreased. Possible factors that influence the pitting behavior of aluminum was proposed, including cycling aging, charge potential, alloy composition, water contamination and temperature. Aluminum current collector

22

was proved to have excellent corrosion resistant performance in 1M $LiPF_6$ in 1:1 EC+DMC and in other electrolyte systems, including EC+EMC, EC+EMC+PC.

1.4.3 Adverse effect of corrosion of current collector on lithium-ion battery performance

Deterioration of battery performance is a function of many factors, including operating temperature, coating quality of active materials and electrolyte composition, etc. Corrosion of aluminum current collector results in corrosion pitting, cracks in aluminum foil, contamination of aluminum ions released into electrolyte (as high as 2700 ppm) and even possible mechanical degradation of cathode. There is no doubt that the corrosion will lead to a continuous increase in the internal resistance of the battery, with considerable loss of apparent capacity. Thus it is expected corrosion will significantly affect the capacity fade and power fade in lithium ion batteries. Many studies have been carried out to evaluate the performance of individual parts of lithium ion batteries, however, few have been found on influence of aluminum current collector corrosion.

Xueyuan Zhang et. al[30] evaluated the corrosion of current collector in lab assembled cells which use different types of cathode materials using $LiPF_6$ as the salt. The cells are disassembled after life cycling test and the corrosion on current collector surface were observed by optical microscope. It is found that a small amount of corrosion may trigger significant capacity loss (as high as 20%), which might due to the loss of contact between cathode material and current collector. The charge/discharge performance is not directly proportional to the corrosion extent. However, the cells with poor performance with severely corroded current collectors were cycled only a few times and then failed (less than 200 charge/discharge cycles). Zhang et. al also found that the corrosion of Al plays an important role in the self-discharge of $Li/LiMn_2O_4$ cell.

T. C. Hyams et al[29] reported that the corrosion of aluminum current collector results in battery's power fade and capacity fade. The experiments were performed on 18650 cell with $LiNi_{0.8}Co_{0.15}Al_{0.5}O_2$ as cathode and ethylene carbonate (EC) + ethylmethyl carbonate (EMC) with 1.2 M LiPF6 as the electrolyte. Battery cycle-life tests were conducted at 25 ℃ for times ranging from 4 weeks to 140 weeks. Also five cells were cycle-life tested at 45 ℃ for time period ranging from 0 weeks to 68 weeks. A correlation between aluminum current collector corrosion and battery performance fade was found, as listed in table 1.2. Corrosion of aluminum is also confirmed by ICP tests, which shows around 2500 ppm of aluminum ions in electrolytes after cycling for 52 weeks.

Table 1.2 Cycling parameters for tested cells at 25 °C and 45 °C.

Cycling time	Temp ℃	Corroded area (%)	Pit density (pits/cm²)	Power fade (%)	Capacity fade (%)	Al concentration (ppm)
4	25	6.9	9.6×10^5	2	2.9	
20	25	8.7	9.6×10^5	9.38	5.89	
36	25	8.3	1.1×10^5	15.56	7.69	
52	25	13.6	1.9×10^5	19.77	10.2	2529
68	25	10.9	1.3×10^5	25.28	11.55	2669
140	25	17.5	2.0×10^6	46.15	31.75	
0	45	1.66	3.59×10^5	0	0	
0	45	5.16	6.1×10^5	0	0	
4	45	8.53	2.4×10^6	9.56	3.2	
32	45	9.32	9.0×10^5	22.9	30.77	
40	45	8.69	1.8×10^6	28.8	13.7	
68	45	7.98	1.1×10^6	51.8	10.9	

The results indicate that the corrosion is a significant cause of performance degradation. There is a strong correlation between the fractions of area corroded and the power fade and capacity fade of the tested batteries. Notably, corrosion is not only the factor that may cause

degradation of battery performance. Solid electrolyte interface deterioration, phase separation of cathode and increased impedance could also be the reasons for capacity and power fade.

It is expected that the corrosion of aluminum current collector will impose at least three adverse effects on the battery performance. First, the corrosion of aluminum will decrease the effective interfacial area. Second, the corrosion products increase resistance of the interface of cathode material and current collector. Last, the higher concentration of aluminum ion in electrolyte may significantly impair the performance of cathode and anode.

1.5 Methods for protecting aluminum current collector from corrosion

1.5.1 Inhibitor

Physical adsorption and Chemisorption are two principle interactions between inhibitors and the protected metal surface. Physical adsorption is due to the electrostatic attractive force between inhibiting ions or dipoles and the electrically charged metal surface. The surface charge on metal surface is ascribed to the electric field at the outer Helmhaltz plane of the electrical double layer existing at metal/solution interface.[36] The surface charge is defined as the potential difference between E_{corr} and zero charge potential (ZCP, $E_q=0$) of the metal. The adsorption behavior is related to the charged compounds and the dipoles whose orientation is determined by the surface charge. In chemisorption process, charge sharing or charge transfer happens from inhibitor molecules to the metal surface.

Y. Li described a method of protecting aluminum current collector from corrosion in electrolyte containing $LiN(CF_3SO_2)_2$ (LITFSI).[37,38] LiTFSI is an appealing salt compared to $LiPF_6$ and $LiBF_4$ as it is more thermally and chemically stable. However, it could not be applied in lithium ion battery because of its corrosive effect on

aluminum current collector. The fumed silica nanoparticles have hydrophilic silanol surface groups, which makes the particles effective absorbents. It was presumed that the protection is due to the enhanced adhesion of passive film or protective salt film to aluminum surface compared to liquid without fumed silica. When fumed silica particles are blended into the electrolyte to form gel electrolytes, the electrolytes exhibit desirable properties of both solid and liquid, yet have high conductivity. The composite is shown to attenuate lithium dendrite growth and improve charge-discharge performance. In open circuit potential measurements, the Al/electrolyte interface shows more stability with the adding of fumed silica. The inhibiting effect is attributed to higher viscosity of the composite electrolyte and it assist in immobilizing pitting reaction product.

1.5.2 Growth of oxide passive film

Essentially there are two ways to alter the passive film to achieve better protection. One is simply make the passive film thicker so it takes longer to destroy the passive film. For instance, the pitting potential of aluminum is found to be 3.2V vs Li/Li^+ in an EC/dimethyl ether (DME) system containing different salts. The current density drops to much lower values when the electrode is swept to 5V after heat treating at 480 Celsius for 24 hours, which might due to the growth of passive film layer.[31] But the treatment does not change the kinetic state and thermodynamically the corrosion of aluminum still occurs.

Another is to change the composition of passive films and make it more resistant to corrosion, which is a more effective way. The solubility of passive layer is the determining factor in the stability of the current collector. Some research was carried out to identify the passive films formed on aluminum current collector in contact with various combinations of electrolytes

and lithium salts. The effectiveness of these passive films on protecting aluminum was evaluated.

With EQCM and cyclic voltammetry, X. Zhang studied the passive film formed on aluminum when it is polarized above 4.5V in 1:1 EC/DMC with 1M LiBOB. The results show that the passive film is comprised of $AlBO_3$, which may protect aluminum against pitting corrosion in corrosive 1M LiTFSI.[39]

Wang et al. reported that addition of $LiPF_6$ into electrolytes containing LiTFSI effectively suppress aluminum corrosion. The anodic current decreases with the amount of $LiPF_6$ added. Although $LiPF_6$ usually contains moisture and is less thermally stable compared to LiTFSI, it is essential to lower the corrosion of aluminum at high potentials. Similar inhibiting effects was also found by adding $LiBF_4$ salts. The pits on aluminum decreases with increasing amount of $LiBF_4$ salt. The non-corroded part of aluminum was protected by AlF_3 instead of $Al(BF_4)_3$.

X. Zhang identified the film formed on aluminum anodically polarized in 1:1 EC+DMC with 1M $LiPF_6$ and in 1:1 ethylene carbonate+dimethyl carbonate （EC+DMC）with 1.2M $LiPF_6$ with a combination of three techniques, electrochemical quartz crystal microbalance measurements (EQCM), electrochemical impedance spectroscopy (EIS), and X-ray photoelectron spectroscopy.[30] The results indicates that the films formed on aluminum is comprised of two parts with the out layer as AlF_3, which is about 1nm and the inner layer as aluminum oxide formed in air. Mass increase is found during anodic polarization, indicating a film formation process happens at higher polarized potentials. The anodic polarization behavior of aluminum is almost the same in the two electrolytes thus the small difference in concentration of $LiPF_6$ barely effects aluminum corrosion.

Addition of a small amount of HF into the LITFSI/PC electrolyte was also found to alter the passive film of aluminum. The chemical composition of aluminum changed from Al_2O_3 to AlF_3 and AlOF in the XPS spectra.[40]

1.5.3 Protective coating

Aluminum can be protected by physically separating aluminum from the electrolyte chemistries by a uniform layer of coating. As the coating is applied in a battery, some important properties, such as low resistance, good adhesion to aluminum, thin and lightweight must be required. The coating act as a barrier layer between aluminum and the corrosive media but meanwhile the coating is highly conductive so it does not impair the electron transfer process through current collectors.

Italo Doberdò et al.[41] described a type of carbon coating on aluminum to resist corrosion in contact with aqueous based cathode slurries. The aqueous based cathode slurry is blend of NMC active material and sodium-carboxymethylcellulose (CMC) as binder. A 5 μm carbon film was coated by casting active carbon dispersion on aluminum using profile bar coater and then dried at elevated temperature. It avoids the contact between aluminum and alkaline NMC slurry and thus impedes corrosion although it rises up the additional weight issue. The sweep voltammetry scans of coated aluminum in EC/DMC containing 1M $LiPF_6$ showed much lower current compared to bare aluminum between 3.0 V and 4.5 V, suggesting the protective effect of the carbon layer. M.C. Kimble et al. described a corrosion protective method for aluminum current collector in by conductive bipolar plating in fuel cells. [42] Several potential failure modes of the cell due to the bipolar plate corrosion are assumed, such as pin-hole formation through the bipolar plates, catalyst poisoning because of corrosion products, metal-ion exchange and

passivation effects. To solve the problem, two feasible approaches are described, including the

use of multi-layer coatings on aluminum or sacrificial anode

CHAPTER 2 Effect of Aqueous-based Cathode Slurry pH and Immersion Time on Corrosion of Aluminum Current Collector

2.1 Introduction

Rechargeable lithium ion batteries are widely applied in portable electronic devices. They are considered as one of the most promising options to power hybrid electric and electric vehicles because of its high voltage, joined with high specific capacity and low manufacturing costs.[43,44] In the lithium ion battery manufacturing process, active materials and conductive agents are blended with polymeric binders to form a slurry. Then the slurry is coated on an aluminum current collector foil, dried and calendared to produce the cathode electrode sheet. The time required for the coating process varies from several minutes to longer time periods depending on the coating methods. To make the slurry materials homogeneously mixed, a polymeric binder solvent is added during the blending process. Based on the solvent used, the electrode slurry can be classified into two types, organic solvent based system and aqueous based system.[45] Traditionally, organic n-methylpyrrolidone (NMP), a polar aprotic solvent, is usually used for the organic based slurries. But for the concerns of processing requirements, production cost and environmental issues, manufacturers may move away from organic NMP solvents and instead utilize aqueous based slurries. The most commonly used aqueous binder is the aqueous emulsion of styrene butadiene rubber (SBR) blended with water-soluble sodium carboxymethyl cellulose (CMC).[19] Although the use of aqueous slurry brings distinct advantages for lithium ion battery manufacturing, the transition may introduce additional issues, for instance, the aqueous condition may cause corrosion of aluminum current collectors.

Corrosion of aluminum current collector in lithium ion batteries is considered to be one of the factors that affect the stability of lithium-ion batteries. Recent studies in current collector corrosion are mainly focused on understanding the corrosion mechanism and developing protective methods for current collectors in organic electrolyte with different chemistries [30,32,35,38]. The degradation of the Al current collector may result in a series of problems. The insoluble corrosion products would increase the interfacial electrical resistance and may cause cathode cracking; while the soluble corrosion products might contaminate the active materials and impair the stability of the electrodes. These problems would lead to the attenuation of the battery's electrical performance, life or even safety.[46] Aluminum is kinetically stable in many conditions due to the formation of a passive oxide film on the surface. However, the aluminum oxide passive film is soluble in high pH conditions and dissolution of the passive oxide layer on aluminum alloys strongly depends on the environmental chemistries, including pH and specific active ions.[47,48] Besides, the unavoidable intermetallic particles present in commercial grade high purity aluminum alloys also plays an important role in aluminum corrosion. These particles often have corrosion potentials that are different from that of the aluminum matrix resulting in local galvanic micro-cells. In different corrosion systems, an intermetallic particle can act as an anode or cathode or even both, as a result it determines the galvanic coupling model on pitting initiation and propagation.[11,12,49] In lithium ion battery fabricating process using aqueous slurries, cathode materials are mixed with excess lithium sources such as lithium oxides or lithium hydroxides, which results in an alkaline pH condition in the slurries. Although passivation happens on aluminum and a uniform layer of protective oxide film (Al_2O_3) can be formed on the surface in ambient conditions, the aluminum is sensitive to corrosion, especially localized corrosion in

contact with these slurries with alkaline pH values. Kaminski et.al studied the aluminum current collector corrosion in exposure to $LiNiCoAlO_2$ (NCA), and $LiNi_{1/3}Co_{1/3}Mn_{1/3}O_2$ (NMC) aqueous slurries and reported that even a short period time of exposure to aqueous based slurry cause localized corrosion of high purity aluminum current collectors [50]. The extent of aluminum corrosion was proposed correlated to the alkaline pH values of the slurries. The corrosion on aluminum might also evolve with time during the coating process. Understanding the formation and evolution of aluminum current collector corrosion could shed light on improving the coating process of lithium ion battery using aqueous based slurries. This research aims to further discuss the corrosion of aluminum current collectors under the effect of aqueous based slurries during the coating process and investigate how pH value of aqueous based slurries and the immersion time influence the aluminum passive film composition and structure. Based on the results and analysis, the possible solutions to solve the aluminum corrosion issues caused by aqueous cathode slurry are discussed.

2.2 Experimental

High purity AA1085 aluminum foils were obtained from a commercial supplier (Table 2.1) with 20 μm thickness were punched into 12.7 mm diameter disk samples, cleaned with isopropyl alcohol and dried. The AA1085 is a high-purity aluminum that is commonly used in commercial lithium-ion batteries.[51] NCA and NMC active materials were obtained from a commercial vendor. The active materials were fully mixed with carbon black, carboxymethyl cellulose, aqueous based SBR solvent and distilled water to create slurries of 70 wt% solids content. Another batch of NMC slurry with reduced-lithiation content was also prepared, during which the NMC powder was mixed with distilled water to dissolve any residual lithium species

(e.g. LiOH), rinsed, filtered, and dried at 60°C for 10 hours. The "washed" NMC was then used as the raw ingredient in another slurry as described. The pH of these cathode slurries was measured by Ag/AgCl pH electrode (Mettler FE20), the pH value were 12.98 (NCA), 11.56 (NMC) and 10.00 (washed NMC). Immersing tests were performed in simulated sodium hydroxide solutions with same pH conditions as the aqueous based slurries. Sodium hydroxide solutions of three target pH conditions: pH=10, 11.56 and 12.98 were prepared by dissolving specific amount of sodium hydroxide (Aldrich, analytical grade) into distilled water. Under room temperature, aluminum disk samples were immersed in the sodium hydroxide solutions for five different time periods: 30s, 100s, 300s, 1,000s, and 10,000s separately. This range encompasses the time during manufacturing that the cathode slurry is in contact with the aluminum current collector prior to the slurry being dried. To investigate if other components of the slurry have any effect on the corrosion process, another immersion test was conducted by immersing aluminum in NMC slurry with pH value of 11.56 for 1000 seconds and 10,000 seconds. After immersion, samples were cleaned with distilled water followed by ultrasonic agitation for 5 seconds, rinsed with isopropyl alcohol and then by acetone, finally dried in air. Surface morphology and the elemental composition information of the immersed aluminum foils were examined with a Hitachi S-4800 scanning electron microscopy (SEM) and Energy dispersive spectroscopy (EDS). X-ray photoelectron spectroscopy (XPS) was performed using a HP 5950 A Element and Chemical Analyzer with Mg Kα as the source. The carbon *1s* peak with a binding energy of 284.6 eV was used as the reference for calibration. The core peaks were analyzed using a Tougaard-type background. The peak positions and areas were optimized by using a weight least-squares fitting method with 80% Gaussian, 20% Lorentzian line shapes.

Table 2.1 Composition of AA1085 high purity Aluminum applied as cathode current collectors in lithium ion batteries.

Grade	Composition Specification (maximum values, in wt%)								
1085	Si	Fe	Cu	Mg	Zn	Ga	V	Other (each)	Al (minimum)
	0.1	0.1	0.03	0.02	0.02	0.03	0.05	0.01	99.85

Electrochemical tests were conducted separately from the immersion testing. Aluminum electrodes were ground and polished by standard metallographic techniques to 1 μm alumina. Electrochemical testing was performed using a PARSTAT-4000 in a conventional three-electrode system containing a piece of platinum foil as the counter electrode. The reference electrode was Hg/HgO immersed in 0.1 M KOH (0.171V vs. SHE). It was separated from the body of cell by using a Luggin tube so as to minimize the IR drop. Attempts were made to measure the electrochemical response of aluminum electrode in cathode slurry but the obtained data were out of order and non-usable possibly due to the existence of solid active materials and the high viscosity of the slurry. Measurements were performed in sodium hydroxide solutions of three pH values of pH=10, 11.56 and 12.98 under aerated conditions to simulate the pH values of the NCA and NMC slurries. Open circuit potential testing was carried out with duration of 10,000 seconds. Potentiodymanic polarization was conducted at a scan rate of 1 mV s^{-1}. Electrochemical impedance spectroscopy tests were carried out on aluminum 1085 electrodes that were immersed 1000 seconds and 10000 seconds in the slurries of three pH conditions. After immersion the electrode surface were rinsed with isopropyl alcohol and dried. Measurements

were taken over the 0.01-10,000 Hz frequency range with perturbation amplitude of 10mV root mean square (RMS) and sampling rate of 10 points per decade at open circuit potentials. All the potentials in this paper are shown in Hg/HgO, 0.1M KOH scale. Each measurement was repeated three times and the representative result is reported. Temperature is considered to be constant at 25 °C.

2.3 Results and analysis

2.3.1 Immersion test

By examining the aluminum foils in the as-received condition (figure 2.1), typical mill-finish surface texture was found on the foil but the aluminum surface was free of any forms of corrosion. At high magnifications, some intermetallic particles around the size of 3 μm were found embedded in the aluminum matrix. EDS analysis (figure 2.2) shows that the intermetallic particles were mainly composed of Al-Fe and Al-Fe-Si phases, which are commonly detected impurities in 1xxx aluminum alloys.[50]
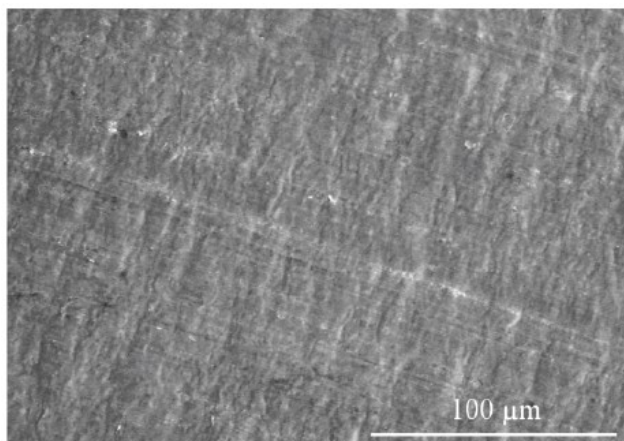
Figure 2.1 High-resolution SEM image of aluminum surface before testing.
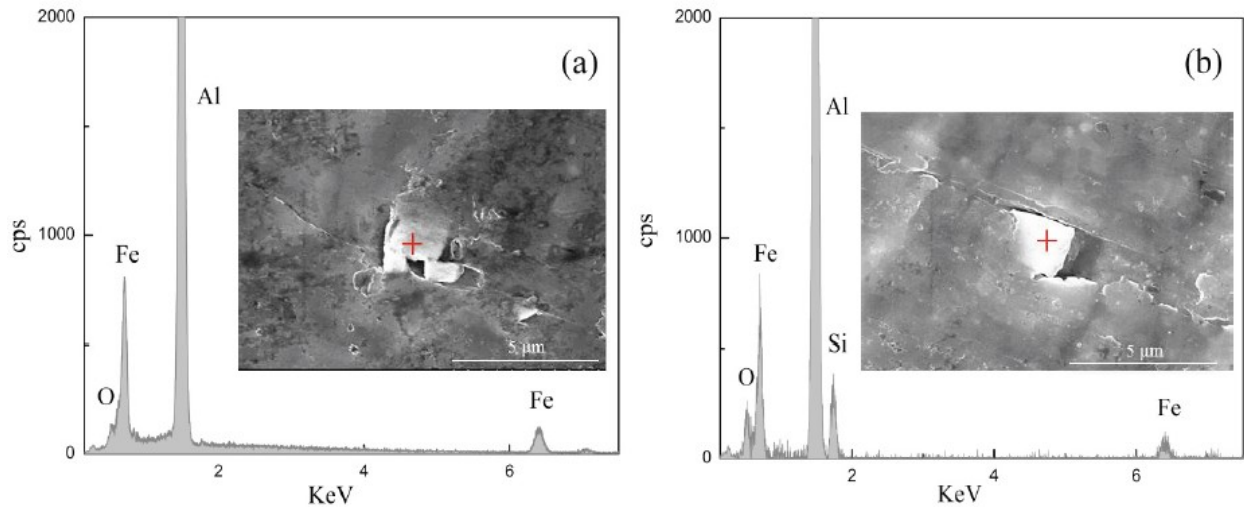
Figure 2.2 EDS analysis shows the elemental composition of (a) intermetallic A, Al-Fe phase; (b) intermetallic B, Al-Fe-Si phase.

Aluminum foils were immersed in sodium hydroxide solutions for different time periods and the surface morphology of the samples were compared (figure 2.3). SEM observation shows that no corrosion was detected after immersing from 30s up to 300s in pH=10 and pH=11.56 conditions. But as it is shown in Figure 2.3a, only after immersed 30s in pH=12.98 solution, some cracks around intermetallic particles, spreading out into random directions, were found on the sample surface, which indicates the initiation of pitting formation at these spots.

Further immersion for 1,000s, as it is shown in figure 2.3b and 2.3c, shows that the samples under pH=10 condition was still free of corrosion but a considerable amount of pitting was detected on both pH=11.56 and pH=12.98 samples. These pits are uniformly distributed on the surface with the size of around 5 μm. Most of the pits were found with a second phase particle located at the center, typically described as trench or circumferential pits.[52] These pits always appear as a ring of attack around a more or less intact particle or particle colony. During the continuous immersion these particles will increase the rate of aluminum dissolution by acting

as cathodes of local cells and finally result in pit formation around these particles. Unique morphologies of the intermetallic particles were observed on the sample in pH=12.98 solution (figure 2.3c). Instead of cubic shapes that were originally found embedded in the aluminum matrix, the intermetallic particles appear as stick-like shape instead, indicating that the aluminum matrix around these intermetallic particles was corroded and the particles were fully exposed to the corrosive media. Figures 2.3d and 2.3e shows the SEM images of samples after immersion for 10,000 seconds. Pits started to form on pH=10 sample surface (figure 2.3d) although the corrosion was comparably modest. Pitting on pH=11.56 sample (figure 2.3e) continued to grow around intermetallic particles, with pit diameters exceeding 50 μm, which were as much as ten time larger than that observed in the same pH at 1,000 seconds. Notably, in pH=11.56 condition, intermetallic particles were fully exposed and some of them exceed 10 microns in its radial direction. Observing the topography of pitting in figure 2.3e proves that general corrosion also occurred on aluminum surface and a thick layer of corrosion product was formed. A single layer of corrosion product was found covering the sample but it was not uniform in the central pitting area where a few cracks on the pit edges were formed. The aluminum foil sample that was immersed in the pH=12.98 sodium hydroxide solution, however, completely degraded and dissolved into the solution such that no SEM observation was possible. Although the above immersion tests were performed in simulated sodium hydroxide solutions, the size, distribution and morphology of pitting evolved in the same way as the results described by Church et al[15] when aluminum foil was in contact with aqueous slurries containing NMC or NCA active materials. This is clear evidence that the pH value is a significant factor on the corrosion of aluminum current collectors in contact with aqueous based cathode slurry. The presence of active

materials in direct contact with the aluminum does not appear to be a prerequisite for pit formation to initiate or develop.
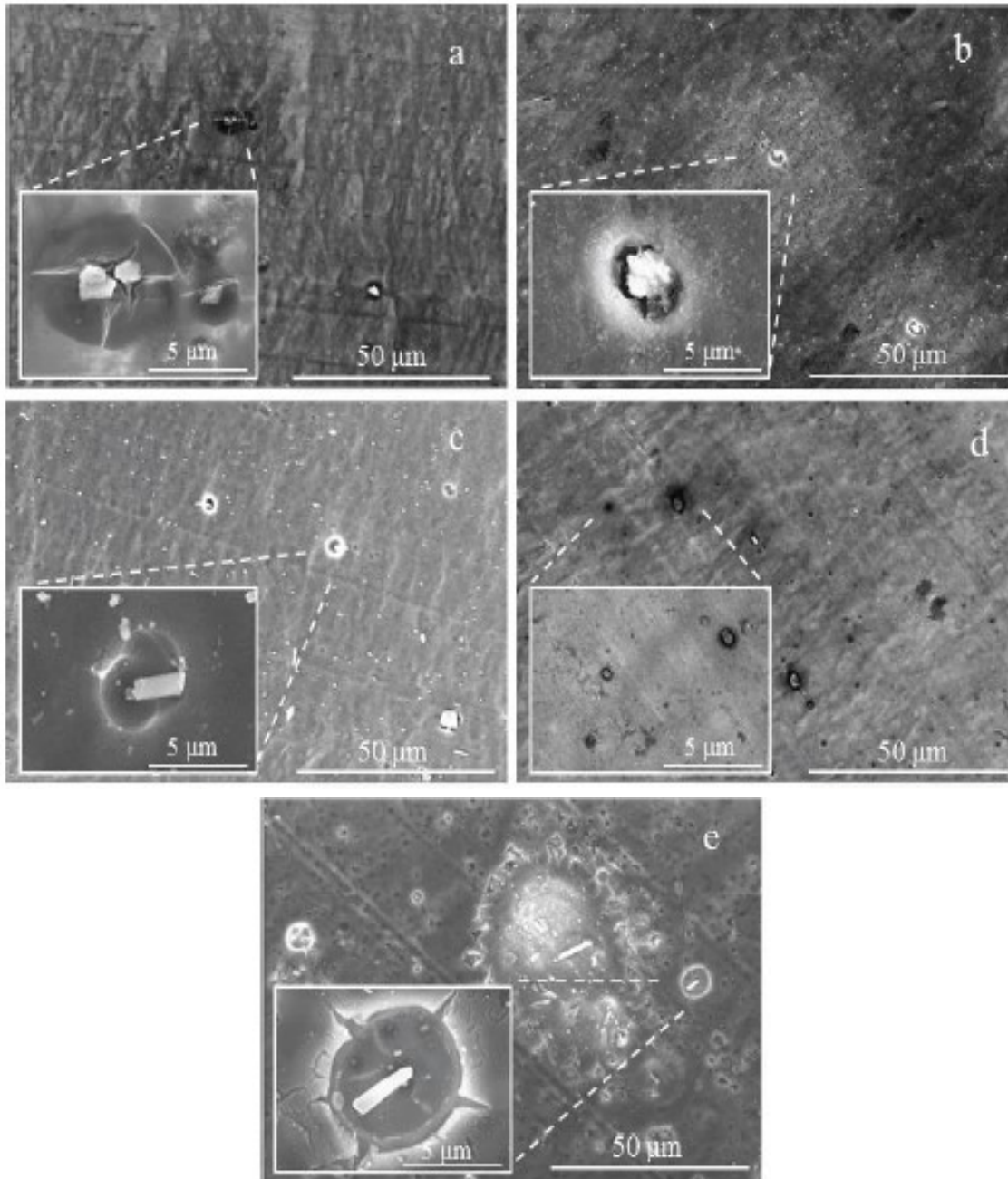
Figure 2.3 High-resolution SEM images of aluminum surface after immersion tests, (a) 30 seconds at pH=12.98, (b) 1000 seconds at pH=11.56, (c) 1000 seconds at pH=12.98, (d) 10,000 seconds at pH=10, (e) 10,000 seconds at pH=11.56

The composition of the passive film formed on aluminum might be altered during its exposure to the aqueous-based slurries thus its ability to protect aluminum may be changed. Since the cathode slurry is composed of lithium metal oxide, active carbon, aqueous binder and water, it is important to determine how the aluminum passive film is affected by these complex chemistries. To study the change of passive film composition during the coating process, XPS was carried out on aluminum current collectors after immersion in aqueous cathode slurries. Aluminum foil was immersed in NMC slurry with pH value of 11.56 for 300 and 10,000 seconds and XPS analysis was performed on the samples after being gently cleaned and dried. Figure 2.4 shows the XPS survey scans after immersion in NMC slurries (pH=11.56) for 10,000 seconds. As evident in the spectra, carbon, aluminum and oxygen are present on the surface. The considerable amount of carbon is due to absorbed carbon dioxide. It is worthy to note that the presence of only Al and O peaks in the surface films proves that there is no chemical interaction between the aluminum passive film and the complex slurry chemistries, such as the active material and aqueous binders. Thus when the aluminum is in contact with the aqueous slurries, the pH of aqueous cathode slurry is considered as the controlling factor on the aluminum corrosion process.

High-resolution XPS scans of Al *2p* and O *1s* core-level peaks of a bare aluminum foil and the foils immersed in NMC slurry with pH value of 11.56 for 300 and 10,000 seconds were obtained and compared in figure 2.5. The curves are fitted into the most probable components needed for corresponding chemical assignments. The Al *2p* core-level peak of bare aluminum was curve fitted into two peaks while the O *1s* core-level peak was fitted into only one peak (figure 2.5a). Comparing the binding energy positions of the peaks to literature values, the two Al *2p* peaks were assigned to Al_2O_3 and Al.[53] Thus the passive film formed on bare aluminum is

confirmed to be only Al_2O_3. For the sample immersed in aqueous slurry for 300 seconds, the Al *2p* and O *1s* core-level peaks were deconvoluted into two Gaussian-Lorentzian sub peaks (figure 2.5b). Combining the fitted results of Al *2p* and O *1s* and considering the reported corresponding value from literature, the two sub peaks are assigned to Al_2O_3 and $Al(OH)_3$. [53–56] After 10,000 seconds of immersion, the Al_2O_3 component disappears and the core-level peaks are fitted into one $Al(OH)_3$ peak (figure 2.5c). The absence of a pure aluminum peak in the Al *2p* core level indicates that the films formed after the immersion process were thicker than the XPS analysis depth. The fitted results show that within the XPS analysis depth the oxide passive film was partially dissolved after 300 seconds and completely degraded into hydroxide after longer period of immersion. The change in composition of the surface films indicates that degradation of the oxide layer occurred due to the high pH condition so aluminum gradually lost the protective passive layer under the effect of alkaline slurries.
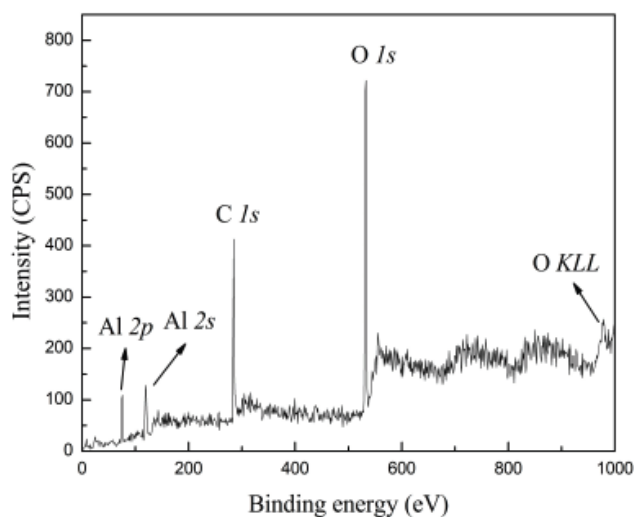
Figure 2.4 Scan survey of aluminum foil immersed in NMC slurry for 10,000 seconds.
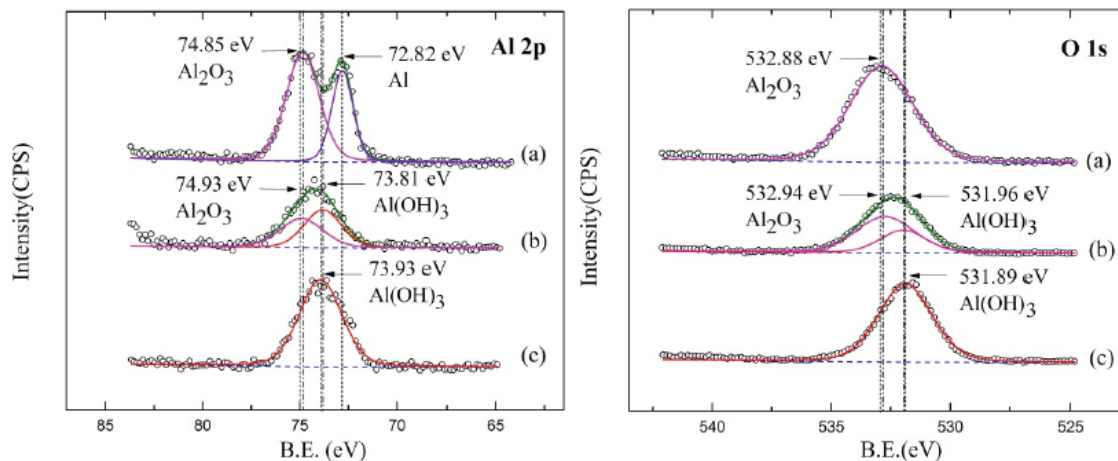
Figure 2.5 Fitted XPS peaks of (a) bare aluminum and aluminum foils immersed in NMC slurry for (b) 300 seconds, (c) 10,000 seconds.

To study the pH effect on aluminum surface layer composition, XPS was also carried out on aluminum foils immersed in simulated sodium hydroxide solutions that are not encumbered by the complex chemistries of the aqueous cathode slurries. The samples were immersed for 1,000 seconds and 10,000 seconds at the same pH values of the three slurries, pH 10, 11.56 and 12.98. As shown in Figure 2.6, fitted high-resolution spectra of Al $2p$ and O $1s$ shows the coexistence of Al(OH)$_3$ and Al$_2$O$_3$ on the surface of aluminum immersed in pH 10 solution after immersion for both 1,000s and 10,000s. The fitted curves also show a decreased intensity ratio of the Al$_2$O$_3$ sub peak to the Al(OH)$_3$ sub peak, which indicates that thinning of oxide film also occurs after longer periods of immersion. Although generalized corrosion is happening and the passive film is partially dissolved due to the light alkaline pH condition, the oxide layer remains on the surface so the aluminum matrix is well protected. The fitted curves for aluminum immersed in pH 11.56 and pH 12.98 solutions, however, show only one compound, Al(OH)$_3$, on the aluminum surface, which indicates that the oxide passive film across the analyzed region has completely degraded into hydroxide. To further confirm the surface composition and fitted results, the atomic ratios of Al/O

41

elements were obtained as shown in table 2.2. The atom ratios were calculated by the area under the fitted peaks of Al *2p*, O *1s*, and C *1s* and applying the standard single element sensitivity factors of 0.6, 2.49 and 1 obtained from the instrument for the respective peaks. The Al/O atomic ratios for the surface film formed in pH 11.56 and pH 12.98 solutions are very close to the theoretical Al/O ratio of $Al(OH)_3$ (0.33). A possible reason for the small difference is the light hydration of the Al_2O_3-surface with the humidity in air. The Al/O molar ratio for the sample surface in pH 10 solution is between the theoretical Al/O ratios of Al_2O_3 (0.67) and $Al(OH)_3$ (0.33), which proves again that the passive film is partially corroded into hydroxide. The attenuation of the oxide passive film at high pH values would allow easier charge transfer; promote the electrochemical reaction process, and finally result in vigorous aluminum dissolution.

2.3.2 Electrochemical test

The open circuit potential (OCP) of 1085 aluminum in sodium hydroxide solution with pH 10, pH 11.56 and pH 12.98 conditions are shown in figure 2.7. The results suggest a remarkable difference in electrochemical driving force for the corrosion of aluminum 1085 with the change of pH values. In pH 10 solution, aluminum shows the highest OCP with an initial ennoblement toward -355 mV, followed by a potential decrease and gradually stabilization at -410 mV. The shape of the curves at the other two pH conditions are identical; both initiate with a comparably negative OCP, then increase with time for a few minutes before the potential is finally stabilized at a specific value. For pH 11.56 condition, the OCP varies within a very small window close to -1.15 V after 1,000 seconds. In the case of pH 12.98 solution, the OCP reveals the most negative value, commencing at -1.573 V and then increasing with time toward -1.317 V. The initial potential shift to noble direction in these curves could be associated to the depletion of OH^- ions near the

aluminum surface.[48] In pH 11.56 and 12.98 solutions, gas bubbles were found on the electrode surface after a few thousand seconds, suggesting the release of hydrogen gas because of aluminum matrix dissolution.
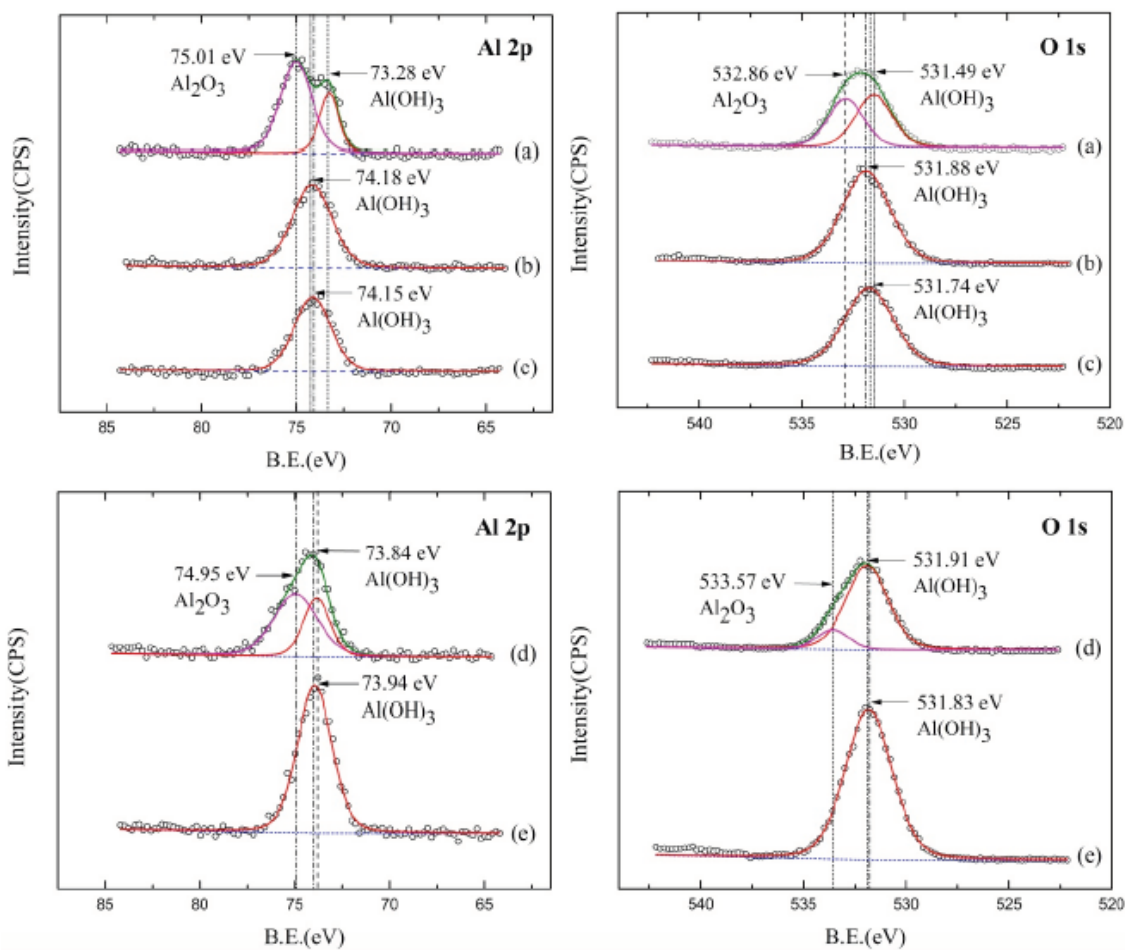
Figure 2.6 Fitted XPS peaks of aluminum foils immersed in sodium hydroxide solutions with (a) pH=10, (b) pH=11.56, (c) pH=12.98 after 1,000 seconds and (d) pH=10, (e) pH=11.56 after 10,000 seconds.

Table 2.2 Surface aluminum/oxygen elemental ratio calculated from XPS peaks.

Sample	(a)	(b)	(c)	(d)	(e)
Al/O ratio	0.467	0.325	0.306	0.437	0.298
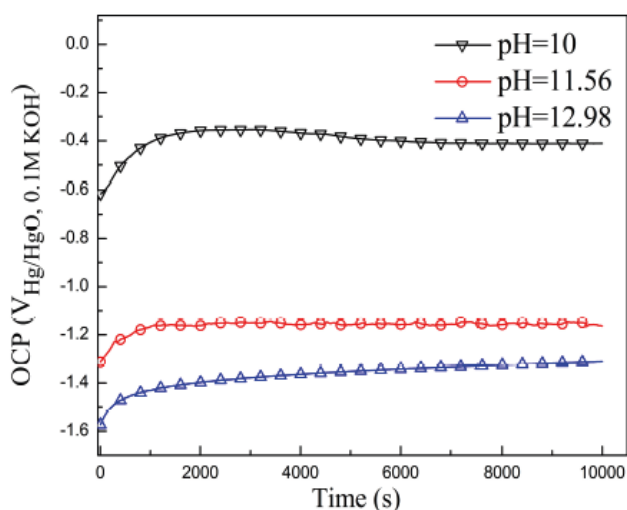
Figure 2.7 OCP vs time for 1085 aluminum in sodium hydroxide solution at pH 10, 11.56 and 12.98.

Figure 2.8 shows the potentiodynamic polarization response of aluminum 1085 in the three pH conditions. The results show apparent thermodynamic stability differences under the effect of pH. An obvious trend obtained from this curve is that the corrosion potential (E_{corr}) reduces with increasing pH value. The E_{corr} changes from vicinity of -739 mV at pH 10 to -1280 mV at pH 11.56, and to a comparable lower value of -1434mV at pH 12.98 solution. Typical passivation process is found in anodic polarization above E_{corr} in both pH 10 and 11.56 solutions. In the case of pH 10 condition, the curve displays passivation within a range of close to 350 mV and pitting potential at 201 mV before a clear "breaking down". The passive window is extended to about 1400 mV at pH

11.56, notably although the pitting potential at pH 11.56 is slightly increased to the vicinity of 280 mV, it's still very close to that of pH 10 condition. Upon increasing the pH, however, the logarithm value of the current density during passivation increases from -5.67 at pH 10 to the vicinity of -5.14 at pH 11.6. Under pH 12.98 condition, the reasonable high current density value (about 3mA cm^{-2}) within its anodic curve range indicates that aluminum dissolution still occurs through the oxide or hydroxide film that allows charge or ion transfer, which is defined by Baroux as pseudo-passivity.[57] The remarkable difference of the aluminum corrosion potential shows that aluminum has a higher tendency of corrosion at higher alkaline pH values. Also, the current density values indicate that kinetically aluminum will suffer more corrosion with the raise of pH value.
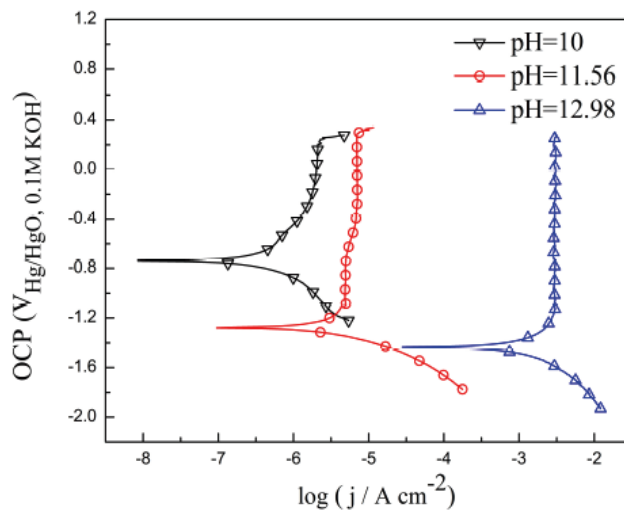
Figure 2.8 Potentiodynamic polarization curves of aluminum electrode under simulated sodium hydroxide solutions at pH=10, 11.56 and 12.98.

EIS tests were taken on aluminum electrodes that were pre-immersed in slurries of three pH value for 1000 seconds and 10,000 seconds. The measured and fitted Nyquist plots of the results

are presented in figure 2.9. The electrodes immersed in pH 10 and the one in pH 12.98 slurry for

10,000 seconds showed a depressed capacitive loop at the high frequency and a capacitive loop at

the low frequency. There exists an induction loop in the medium frequency domain in pH 11.56

slurry and the one in pH 12.98 for 1000 seconds. The induction loop may be related to the

relaxation process obtained by the absorption of corrosion products on electrode surface, which is

similar to the findings for aluminum behavior in acidic solution and concentrated alkaline

electrolytes.[58,59] With increasing pH value and immersion time, the radius of the capacity loop at

the high frequency decreases.

The equivalent circuit model in figure 2.9d was employed to characterize the electrodes

that presented an induction loop in medium frequency. The parameters were obtained by fitting

circuit analogs to the experimental data. In this model, the passive film is considered to have a

non-homogeneous structure and shows non-ideal capacitive behavior, represented by constant

phase element (CPE). The constant phase element is a "distributed" element that produces

impedance with a constant phase angle in the complex plane. It is a mathematical construct that

characterizes the response of a process with a constant phase shift over a large frequency range.

The impedance of the CPE (Z_{CPE}) has the mathematic form of:

$$Z_{CPE} = \frac{Q}{(j\omega)^{1-\alpha}}$$

where Q is the frequency-dependent magnitude of a pseudo-capacitance, and ω is the angular

frequency. The exponent α is constrained to $0 \leq \alpha \leq 1$, which describes the ideality of the electric

double layer capacitance.[60]
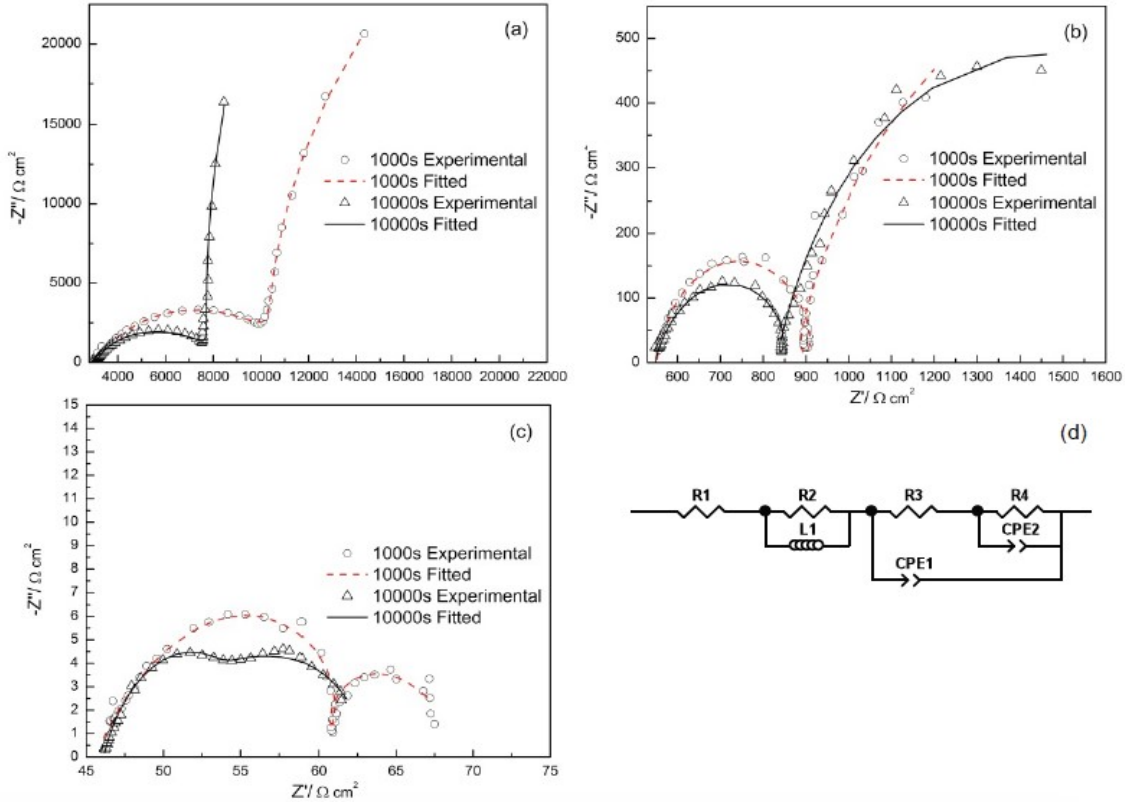
Figure 2.9 Nyquist plots for aluminum 1085 immersed in slurries of (a) pH=10, (b) pH=11.56, (c) pH=12.98 and relevant equivalent circuit model used to simulate the EIS spectra (d).

In the equivalent circuit model (figure 2.9d), R_1 represents the uncompensated electrolyte resistance. R_2 and L_1 are the resistance and inductance corresponding to the absorption of corrosion products. CPE$_1$ is constant phase element associated with the oxide film. R_3 is the charge transfer resistance of the electrochemical process between the passive film and the aluminum matrix. CEP$_2$ was used instead of a capacitor due to the non-linear response of the electric double layer capacitance across passive film/substrate interface. For the Nyquist plots without the induction loop at medium frequency, the induction loop elements R_2 and L_1 are removed from the equivalent circuit during fitting.

The fitted parameters and the calculated effective capacitance are presented in table 2.3. The effective capacitance of the constant phase element is calculated with Brug's model [60]. The

behavior is explained based on the idea of electric double layer capacitance distribution along the interface caused by surface inhomogeneity. For a faradaic system, C_{eff} is expressed as

$$C_{eff} = [Q * (\frac{1}{R_s} + \frac{1}{R_{ct}})^{\alpha-1}]^{1/\alpha}$$

With the increasing pH and prolonged immersion time from 1000 seconds to 10,000 seconds, the fitted resistance associated to the passive film (R_3) and charge transfer resistance (R_4) has an obvious decreasing trend, which proves that the passive film is less protective at high pH values or when immersed longer. On the other hand, the effective capacitance of the passive film (C_{eff-1}) and double layer (C_{eff-2}) follow an opposite increasing trend, which indicates the change in its ability to storage charges. It is known that the capacitance is inversely proportional to the thickness of passive film. Thus with the increase of pH and immersion time the attenuation of the passive film occurs. The α values for the passive film and the electric double layers are close to unity, which present properties close to capacitors, despite that the fitted α_2 at pH 10 and pH 12.98 condition are 1 thus the CPE behaves as an ideal capacitor. The property change of the passive film elements at higher pH condition and prolonged immersion time is proved to be a consequence of the degradation of the protective oxide passive films

Table 2.3 Parameters obtained by fitting equivalent circuit model of 1085 aluminum immersed in slurries of three pH values for EIS tests.

pH	Time s	L_1 H cm^2	R_2 Ω cm^2	R_3 Ω cm^2	Q_1 S$^\alpha$ Ω^{-1}	α_1	R_4 Ω cm^2	Q_2 S$^\alpha$ Ω^{-1}	α_2	C_{eff-1} F cm^{-2}	C_{eff-2} F cm^{-2}
10	1000	-	-	13131	2.77E-06	0.89	99867	1.49E-04	1	1.50E-06	1.49E-04
	10000	-	-	4984	6.92E-06	0.84	78130	1.86E-04	1	2.96E-06	1.87E-04
11.56	1000	2.28	73.92	394.9	1.13E-05	0.87	1697	3.17E-03	0.80	4.74E-06	3.19E-03
	10000	1.90	84.31	377.2	2.83E-05	0.77	1221	5.50E-03	0.84	6.45E-06	5.99E-03
12.98	1000	0.73	38.01	36.67	7.70E-04	0.65	25.33	2.13E-04	1	4.91E-05	2.13E-04
	10000	-	-	29.9	2.04E-03	0.82	8.202	1.90E-03	1	9.22E-04	1.91E-03

2.4 Discussion

Combining the above results, the corrosion process of aluminum during exposure to cathode slurry is described as follows. Since the aluminum matrix and passive film that are in contact with intermetallic particles are relatively less stable, when aluminum is exposed to alkaline slurries, the localized corrosion begins from the breaking down of initial air-formed alumina around intermetallic particles in the form of the following reaction:

$$Al_2O_3(s) + 2OH^- + 3H_2O \rightarrow 2Al(OH)_4^- \tag{1}$$
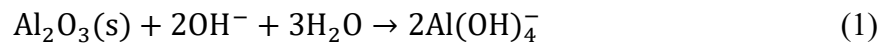
Generalized corrosion that results in the attenuation of the passive film across the aluminum surface also follows this reaction path. The later localized corrosion of aluminum matrix surrounding the intermetallic particle is mainly caused by the formation of a galvanic cell between aluminum matrix and second phase Al-Fe and Al-Fe-Si particles. From the evolvement of pitting in the immersion test, the aluminum matrix acts as the anode and the embedded second-phase particles act as cathode thus the following electrochemical reaction is built up:

$$\text{Anode reaction: } Al(s) \rightarrow Al^{3+} + 3e^- \tag{2}$$

$$\text{Cathode reaction: } 2H_2O + O_2 + 4e^- \rightarrow 4(OH)^- \tag{3}$$
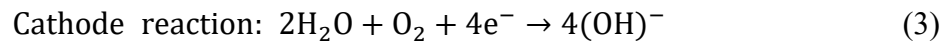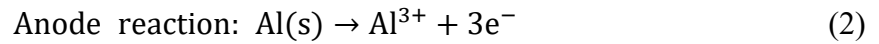
The overall oxidation and reduction reaction are combined to be:

$$4Al(s) + 6H_2O(l) + 3O_2 + 4e^- \rightarrow 4Al(OH)_4^- \tag{4}$$
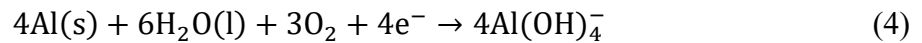
The aluminate ion $(Al(OH)_4{}^-)$ in the product can be written in forms of $Al(OH)_3$ and OH^-. It is known that $Al(OH)_3$ is amphoteric, that is, it dissolves in both acid and bases. In neutral non-complex solutions, it is relatively stable with the pH range of $4 - 8$. But at extreme pH values, sodium hydroxide solution may cause super-saturation and rapid precipitation of

aluminum hydroxide [7]. The aluminate ions are transformed into aluminum hydroxide after crystallization. The transformation reaction is as follows:

$$Al(OH)_4^- \rightarrow Al(OH)_3(s) + OH^- \tag{5}$$
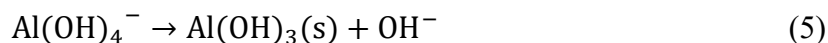
During the galvanic cell reaction, the anode aluminum dissolves away from surrounding matrix, reacts with hydroxide ions and water and finally deposits as Al(OH)₃ corrosion products. This electrochemical reaction between the anode and cathode runs continuously during the immersion test. As revealed in the immersion tests, the passive film loses its protectiveness to aluminum when the oxide passive film is transformed into hydroxide corrosion products in strong alkaline solutions. The degradation of the protective oxide film leads to the property change corresponding to the passive film elements thus aluminum is prone to more corrosion at higher pH conditions, which was proved by the electrochemical results.

It was observed that some of the intermetallic particles are not present in the central area of a pit because of depleting of aluminum matrix around the particle, leaving only the pitting on sample surface. When the aluminum corrosion happens during the cathode coating process in lithium ion battery fabrication, it is possible that the corrosion products and intermetallic particles may migrate into the aqueous based slurries and be intercalated inside the coating after drying and calendaring. This contamination of the cathode active materials could increase the resistance, generate extra heat and impair the stability of active materials during operation of the battery, which is harmful for battery performance; or even cause irreversible damage to the battery. Elimination of the intermetallic particles by using higher purity aluminum is a possible strategy to reduce these adverse effects from corrosion. This would effectively reduce the amount of localized galvanic corrosion although it would also introduce extra production cost. In

the future, more work on optimizing the composition of aqueous based cathode slurries is necessary to make it less corrosive for aluminum current collector. As pH was proved to be the controlling factor on corrosion, the optimization can be achieved by adjusting the pH value of the cathode slurry by adding acid-based buffers. Kazunari et.al reported that the use of alginic acid as the aqueous binder enables the preparation of pH controlled NMC slurries and the corrosion of aluminum current collector could be prevented.[61] In a recent patent, 0.1%-0.5% by weight of pH modifier were introduced in to aqueous cathode slurry during coating process to adjust the pH value of cathode slurry below 9 so the corrosion of degradation of current collector may be mitigated. The pH modifiers could be organic acids including, but not limited to carboxylic acid derivatives. It is expected that addition of the mild organic acid into cathode slurry could modify the pH close to neutral values where aluminum is thermodynamically and kinetically stable so the corrosion issue could be resolved.

2.5 Conclusion

The pH value of aqueous based cathode slurry significantly affects the corrosion of aluminum current collectors used in lithium ion batteries. In simulated sodium hydroxide solutions, the aluminum current collector suffers more localized corrosion when in higher pH solutions or for longer immersion times. The formation of localized galvanic cell causes a higher rate of aluminum dissolution around intermetallic particles and the growth of pitting. After immersion in cathode aqueous slurry, the existence of only C, Al and O elements on surface indicates that the aluminum surface film composition was only altered by the alkaline pH condition rather than other components from aqueous based slurry such as the cathode active material. The electrochemical characterization describes similar aluminum corrosion behaviors

in response to solution pH change. High-purity aluminum presents less electrochemical stability when the passive film is attenuated under the alkaline pH and longer immersion time periods. The EIS analysis proves that the instability is attributed to the change in resistance and capacitance associated with surface passive film and electric double layers. The possible strategies to mitigate the corrosion during cathode coating process include using aluminum foils with higher purity or modifying the pH value of the slurry to more neutral values with mild organic acids.

CHAPTER 3 Electrochemical Stability of Aluminum Current Collector in Aqueous Rechargeable Lithium-ion Batteries

3.1 Introduction

Lithium ion batteries are considered as one of the most promising power sources for electric vehicles and large-scale energy storage applications. Commercial lithium ion battery uses organic electrolytes, which provides a wide stability window of around 4 volts. However, the organic solvents in the electrolyte are highly toxic and flammable, which raises significant safety concerns in the case of improper uses, such as overcharging or short-circuiting.[43] An alternative approach to the organic-based lithium ion battery is aqueous rechargeable lithium ion battery (ARLB), which was first introduced by Dahn's group in the 1990s.[18] The use of aqueous electrolytes brings several benefits. It eliminates the safety issues caused by the organic electrolytes and is much more environmental friendly. Additionally, the conductivity of aqueous electrolytes is around 1 S/cm, which is orders of magnitude higher than the typical organic electrolytes containing $LiPF_6$. This allows higher round-trip efficiency and more flexible design of electrodes whose design thickness is often limited due to the low conductivity of the organic electrolytes. Using aqueous electrolytes could also eliminate the strict humidity controlled assembling environment required for traditional organic electrolytes thereby reducing manufacturing costs.[26,62,63] ARLB has not been commercialized primarily because of the narrow stability window of aqueous electrolytes, which limits energy density of the battery. The theoretical stability or operating window of an aqueous solution is 1.23 V, although the stability window was found extended to 2 volts or wider due to kinetic barrier effects.[64] However, the aqueous-based battery has attracted more attention recently because the advantages of ARLB

make it very competitive for large-scale stationary energy storage applications where the energy density of the system is not a primary performance target.[17,24]

High purity aluminum is preferred as the current collector material in energy storage systems such as lithium ion batteries and super capacitors partially because of its particular physical properties such as low density, high conductivity and low cost [28]. Degradation of the aluminum current collector may occur in organic electrolytes. For instance, serious corrosion was found on aluminum current collectors when lithium bis(trifluoromethanesulfonyl)imide [$LiN(CF_3SO_2)_2$] was used as the electrolyte salt due to its acidic nature [38]. Corrosion of the current collector would significantly degrade the battery performance in the following ways, (i) it reduces the effective interfacial area between electrolyte and cathode electrode; (ii) solid corrosion products might deposit on the electrode and increase the internal impedance of battery; (iii) the dissolved species, Al^{3+} for instance, would contaminate electrolytes, increase self-discharge rate and impair the stability of electrodes.[31,46,65] Evaluating the corrosion-resistance of the aluminum current collector in potential electrolytes is needed to design for battery safety and long-term performance. In the past decade, the focus of research in this area was on the corrosion behavior of aluminum current collectors under the influence of organic electrolyte chemistries, including the effects of various lithium salts, electrolyte solvent and cathode materials.[2,30,31,33,34,40,46,66] To the best of our knowledge, no evaluation has been made on the electrochemical stability of aluminum current collectors in ARLB electrolytes. Recent work has identified both 5 M $LiNO_3$ and 2 M Li_2SO_4 as high performing aqueous electrolytes tested at pH 7.[67] The reported pH values of aqueous electrolytes range from 5 to 11 so as to maintain the stability of various cathode materials, which add concerns on the risk of

possible corrosion of the aluminum current collector at the higher end of the pH range.[24] Some authors speculated that the existence of sulfate and nitrate anions could inhibit the pitting corrosion of aluminum in aggressive aqueous solution by competitive adsorption.[68] An examination of the stability of aluminum in ARLB aqueous electrolytes over a range of pH values is needed to define an acceptable application window. In the present paper the effects of pH value, applied potential and the type of anions in aqueous electrolyte on the corrosion behavior of high purity aluminum are presented. The electrochemical stability of aluminum foils in 2 M Li_2SO_4 and 5 M $LiNO_3$ ARLB electrolytes is examined and the management of component corrosion during the design of energy storage systems is discussed.

3.2 Experimental

3.2.1 Electrolyte preparation

The electrolytes with different concentration and pH value were prepared in three steps. First, an aqueous solution with target pH value was prepared by dissolving specific amount of LiOH or acid into distilled water. The acid used to adjust the pH was sulfuric acid (Macron) for the Li_2SO_4 electrolyte and nitric acid (Acros Organics) for the $LiNO_3$ electrolyte. The specific weight of electrolyte salts, 2 M of Li_2SO_4 or 5 M of $LiNO_3$ equivalent, was added into the solution at room temperature and magnetically stirred until the salts were completely dissolved. To eliminate the effect of liquid volume expansion after the salt addition, the pH of the solution was adjusted again to the target value by gradually adding lithium hydroxide or acid until the expected pH value was achieved. The pH values of electrolytes were measured using a Mettler FE20 Ag/AgCl pH electrode.

3.2.2 Electrochemical measurements

Electrochemical tests were conducted using a PARSTAT-4000 in a plate material evaluating cell (BioLogic Science Instruments), which allows a constant electrode area of 0.5 cm^2. Ag/AgCl with saturated KCl (0.197 V vs SHE) solution was used as the reference electrode. The reference electrode was separated from the body of the cell using a Gamry reference electrode bridge tube with Vycor tip to prevent possible contamination from the reference electrode. The tip of the bridge tube was placed close to the working electrode to minimize the IR drop. Platinum wire, which served as the counter electrode, was shaped into a coil so a surface area approximately twice that of the working electrode was provided. Before each test, the platinum counter electrode was washed and cleaned repeatedly in dilute nitric acid followed by a rinse with distilled water. To determine the stability window of the electrolytes, linear sweep voltammetry (LSV) was performed using high-purity platinum foil as the working electrode scanned at 1 mV/s sweep rate from open circuit potential (OCP) either anodically or cathodically until gas evolution occurred. AA1085 of thickness 20 μm was evaluated in each electrolyte solution. As-received foil samples were rinsed with isopropyl alcohol and acetone and air dried prior to testing. Cyclic voltammetry was carried out by stabilization first at open circuit potential for 2.5-hours, followed by four consecutive voltammetry cycles, starting from the negative vertex to the positive vertex of the electrolyte stability window at a 5 mV/s scan rate. Linear sweep voltammetry was performed by scanning from open circuit potential to 2 V at 1 mV/s. Chronoamperometry was taken at an anodic potential of 0.85 V for 24 hours. Each measurement was performed three times using freshly cleaned aluminum samples and the representative results were reported. After the electrochemical tests, the aluminum electrode was

immediately removed from the cell, gently rinsed with DI water and dried using a gentle stream of nitrogen. All potential values are reported versus Ag/AgCl, saturated KCl scale.

3.2.3 Inductively coupled plasma

To further provide information on the corrosion of aluminum, the electrolyte after cyclic voltammetry was analyzed for dissolved Al^{3+} by inductively coupled plasma (ICP) using a Perkin Elmer optima 2100DV ICP-OES spectrometer. ICP multi-element standard solutions containing 10 and 1000 ppm aluminum were used to prepare a blank and five calibration standards of 0.01 ppm, 0.1 ppm, 1 ppm, 10 ppm and 100 ppm aluminum. These solutions were prepared by diluting the ICP multi element standard solution with 0.2% HNO_3 in Millipore de-ionized water.

3.2.4 Surface Characterization

The surface morphology of the electrodes after cyclic voltammetry and choronoamperometry were examined with a Hitachi S-4800 scanning electron microscopy. Raman spectroscope microscopy was performed using a Renishaw Inc. 1000B. The Raman spectrum was excited by a helium-neon laser producing highly polarized light at 633 nm and collected in the range between 200 and 4000 cm^{-1}. The spectra were calibrated using the 519.5 cm^{-1} of a piece of silicon wafer. Raman spectrum was acquired with a 10 s integration time and the power at the sample was 10 mW.

3.3 Results and Analysis

3.3.1 Electrolyte stability window

LSV was used to measure the stability window of electrolytes at various pH values. The LSV curves obtained in 2 M Li$_2$SO$_4$ at pH 7 using platinum foil as the working electrode is shown in figure 3.1. E_O and E_H denote the onset potentials at which oxygen and hydrogen evolution, respectively, becomes visible in linear sweep voltammetry. The measured onset gas evolution potentials and the stability window of electrolytes at pH values ranging from 5 to 11 are presented in table 3.1. In figure 3.2, the measured results are compared to the equilibrium stability window of 2 M Li$_2$SO$_4$ and 5 M LiNO$_3$ aqueous solutions calculated from the Nernst equation as follows:

$$E_{H^+/H_2} = E^0_{H^+/H_2} - 0.059 \times pH \qquad (1)$$

$$E_{O_2/H_2O} = E^0_{O_2/H_2O} - 0.059 \times pH \qquad (2)$$

All electrolytes exhibited overpotential due to slow kinetics effects. At a constant electrolyte concentration, the overpotentials varied at different pH values. The span of the stability window was widest at the neutral condition and became narrower at pH conditions that deviated from the neutral value. The apparent dependence of stability window span on the pH value is consistent with the stability window results obtained by Wessels *et al.* using a constant current measurement method.[23] The stability windows depended primarily on the oxygen overpotential which varied with pH. The hydrogen overpotential did not contribute as significantly to the stability window though it deviated to more negative values at pH 5 and pH 7 and it almost overlapped with the theoretical hydrogen evolution potentials at pH 9 and pH 11 conditions.
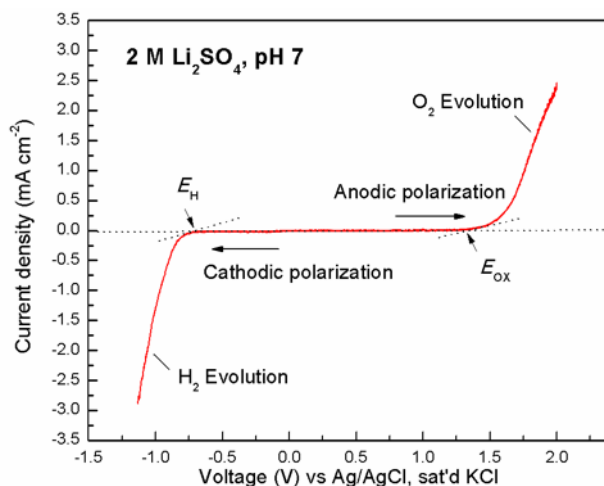
Figure 3.1 Linear sweep voltammetry measured on Pt foil in 2 M Li_2SO_4 electrolyte at pH 7.

3.3.2 Cyclic Voltammetry

Cyclic voltammetry tests were performed to evaluate the stability of the AA1085 foil within the obtained stability windows of the aqueous electrolytes. The open circuit potentials of aluminum measured in the aqueous electrolyte are presented in table 3.2. It was noticed that in 2 M Li_2SO_4 electrolytes at pH 5 and pH 7, and in the 5 M $LiNO_3$ electrolyte at pH 5, the open circuit potential was within the stability window and anodic relative to the stability window for other electrolytes. Figures 3.3 and 3.4 show the cyclic voltammetry curves measured from the first cycle to the fourth cycle. In both Li_2SO_4 and $LiNO_3$ electrolytes, non-reversible oxidation peaks were present in the first cycle but the oxidation peaks diminished or receded in the following three cycles. No cathodic peak was found in the reverse scan and there were wide current plateaus in both positive and negative scans indicating that the aluminum surface remained well passivated within the scan range.
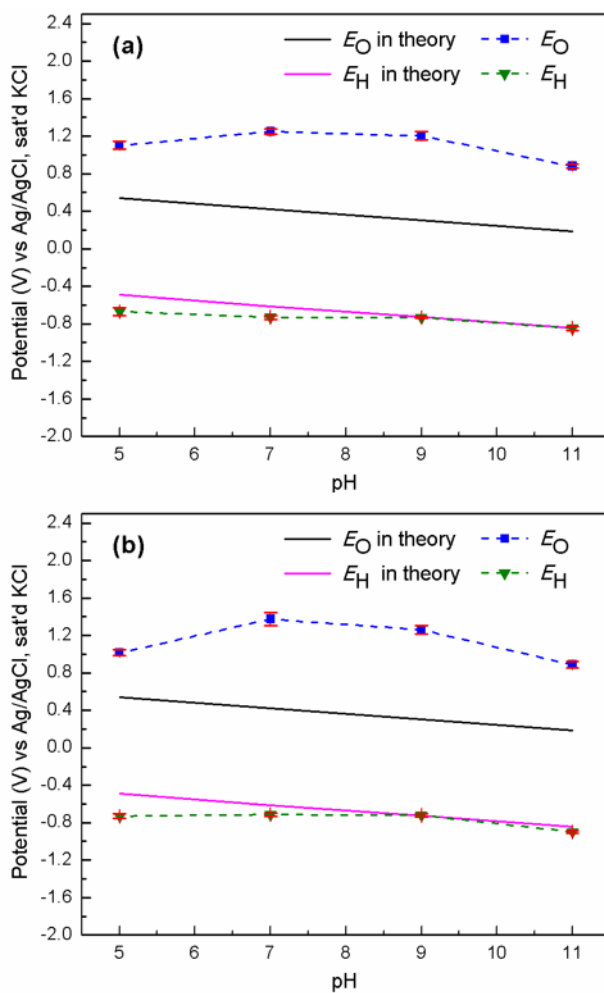
Figure 3.2 Hydrogen and oxygen gassing potentials of (a) 2 M Li$_2$SO$_4$ and (b) 5 M LiNO$_3$ electrolytes measured on Pt foil by LSV compared with theoretical values.

Table 3.1 Hydrogen and oxygen gassing potentials of electrolytes measured by LSV on Pt foil.

Electrolyte	pH	E_O (V)	Standard Deviation	E_H (V)	Standard Deviation	Stability Window (V)
2 M Li$_2$SO$_4$	5	1.1	0.042	-0.668	0.041	1.768
	7	1.25	0.026	-0.73	0.022	1.98
	9	1.202	0.046	-0.733	0.016	1.935
	11	0.88	0.022	-0.83	0.020	1.71
5 M LiNO$_3$	5	1.017	0.033	-0.731	0.024	1.748
	7	1.373	0.071	-0.712	0.018	2.085
	9	1.261	0.043	-0.722	0.016	1.983
	11	0.887	0.034	-0.898	0.016	1.785

Table 3.2 Average OCP and standard deviation for aluminum in test electrolytes.

Electrolyte	pH	Average OCP (V)	Standard Deviation
2 M Li$_2$SO$_4$	5	-0.647	0.03
	7	-0.629	0.05
	9	-0.858	0.026
	11	-1.083	0.159
5 M LiNO$_3$	5	-0.726	0.113
	7	-0.882	0.014
	9	-0.763	0.014
	11	-1.058	0.024

In the 2 M Li$_2$SO$_4$ solutions of pH 7, 9 and 11, (figure 3.3), the current density started to increase sharply in the first cycle at a specific voltage during the positive scan, followed by slight drop after a peak value was achieved and then remained at near-constant values until the positive vertex potential of the stability window in pH 5 Li$_2$SO$_4$ solution, AA1085 had slightly different behavior as the current continued to increase at a slower rate after the initial peak was reached. Although the current densities at different pH values were around the same scale, it is evident that the peak positions shifted in the negative direction when the electrolyte solution became acidic or basic.

In the 5 M LiNO$_3$ solutions (figure 3.4), aluminum exhibited a similar first cycle oxidation behavior as in 2 M Li$_2$SO$_4$ solutions except at pH 11. The current densities in solutions at pH 5 and pH 9 were slightly larger than that at pH 7 but they remained similar. The aluminum exhibited a remarkably different rate of oxidation at pH 11. The current increased sharply beginning from the negative vertex of the scanned potential range. The current density reduced after each cycle but remained around 10^{-5} A·cm^{-2}, which was one order of magnitude higher compared to that at pH 5, 7 and 9. The peak positions did not show the same pH dependency as

in the 2 M Li$_2$SO$_4$ solutions although the oxidation peak position at pH 11 had the most negative value.

Figure 3.3 Cyclic voltammetry curves measured on Al foil in 2 M Li$_2$SO$_4$ electrolytes for four consecutive cycles.
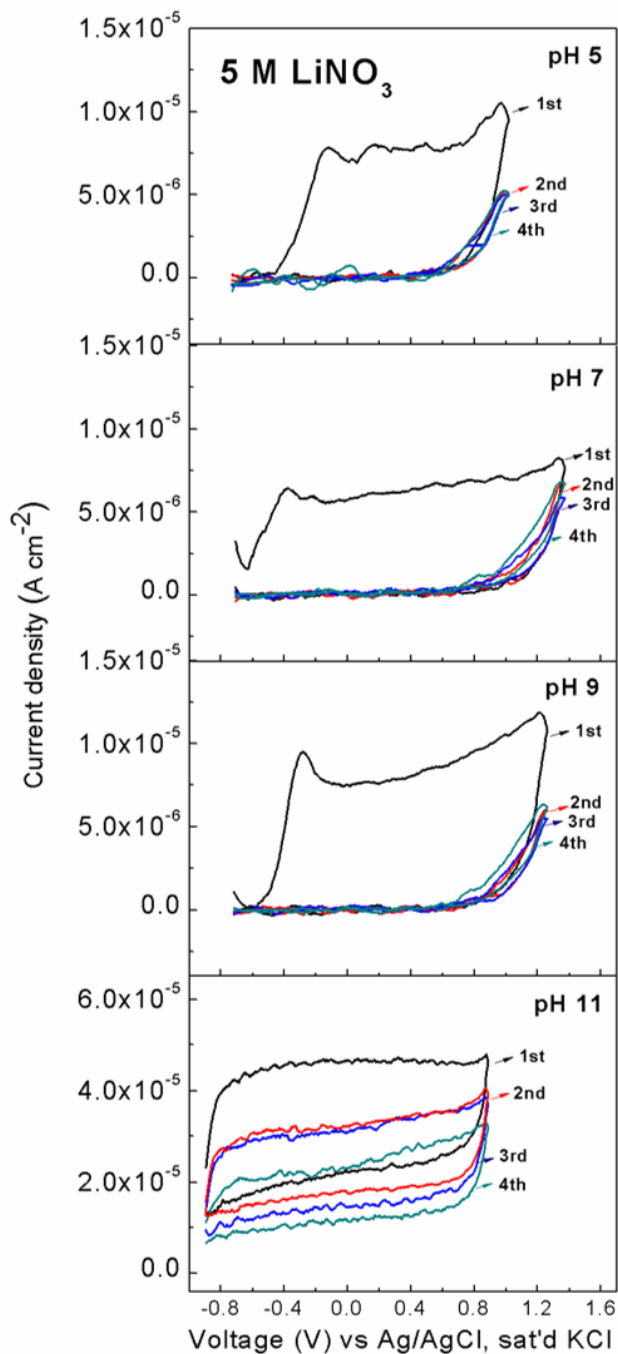
Figure 3.4 Cyclic voltammetry curves measured on Al foil in 5 M LiNO₃ electrolytes for four consecutive cycles.

In the 5 M LiNO₃ solutions (figure 3.4), aluminum exhibited a similar first cycle oxidation behavior as in 2 M Li₂SO₄ solutions except at pH 11. The current densities in solutions

at pH 5 and pH 9 were slightly larger than that at pH 7 but they remained similar. The aluminum exhibited a remarkably different rate of oxidation at pH 11. The current increased sharply beginning from the negative vertex of the scanned potential range. The current density reduced after each cycle but remained around 10^{-5} A·cm^{-2}, which was one order of magnitude higher compared to that at pH 5, 7 and 9. The peak positions did not show the same pH dependency as in the 2 M Li$_2$SO$_4$ solutions although the oxidation peak position at pH 11 had the most negative value.

The current plateaus in the cyclic voltammetry curves in both electrolytes reflect the concurrent dissolution and passivation phenomenon on the aluminum surface [33]. Dissolution starts when the current density increases due to the attacking of aggressive ions on aluminum, and passivation occurs right after the current density peaks. It is evident that the dissolution-passivation of aluminum follows a pH-responding mechanism in the 2 M Li$_2$SO$_4$ solution. When pH deviates from the neutral condition, both the dissolution and passivation processes are more easily activated, possibly due to a reduced energy barrier required for the activation process. In the 5 M LiNO$_3$ electrolytes, there was no abrupt increase in current and after each cycle the current density decreased although higher current density was found in the reversible scans at pH 11. It is reasonable to assume that a fast-growing oxide or hydroxide passive film layer was formed on the electrode surface during the reversible scans and the film protects the underlying aluminum matrix from further rapid dissolution.

3.3.3 Pitting potential measured by LSV

Many attempts have been made to obtain the critical pitting potential to evaluate the pitting susceptibility of aluminum current collectors.[31,38] The type of anions present in aqueous

electrolyte was reported to play a decisive role in determining the pitting corrosion of aluminum upon application of anodic potentials.[24] Linear sweep voltammetry was employed to measure the pitting potential at which abrupt dissolution takes place. Figure 3.5a and 3.5b depict the linear voltammetry scanned from open circuit potential to 2 V. The current density increased sharply when aluminum was polarized to an anodic potential in 2 M Li_2SO_4 solution at pH 11 and all 5 M $LiNO_3$ solutions, with severe pitting visible on electrodes after the test.
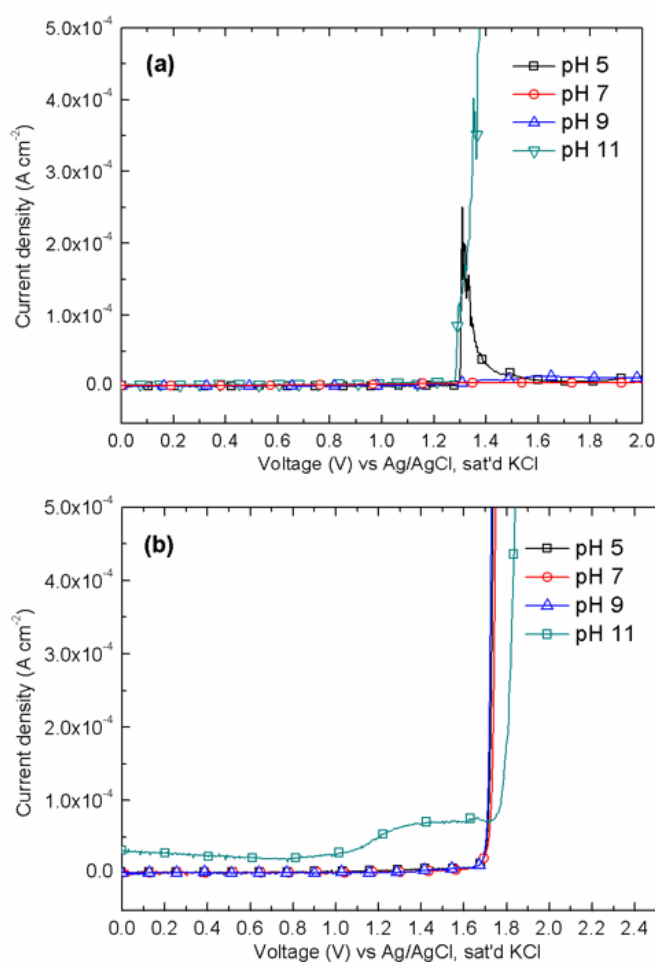
Figure 3.5 Linear sweep voltammetry measured on Al foil in (a) 2 M Li_2SO_4 (b) 5 M $LiNO_3$ electrolytes at different pH values.

In 2 M Li_2SO_4 electrolyte, pitting only occurred at pH 11 and the pitting potential was determined as 1.275 V. Although at pH 5 there is a current increase at 1.298 V, but it immediately declined to $\mu A \cdot cm^{-2}$ levels and there was no sign of pitting on the electrode. In 5 M $LiNO_3$ electrolytes, the pitting potentials for pH 5, 7 and 9 were around 1.655 V and shifted to a more positive value, 1.734 V, at pH 11. Notably, aluminum was prone to pitting beyond the stability window in neutral 5 M $LiNO_3$ solutions but pitting was not observed in neutral 2 M Li_2SO_4 solutions, which indicates a possible inhibiting effect due to the existence of sulfate anions. The inhibition of sulfate on aluminum pitting at lower pH values may be associated to the physical blocking effect at high anodic potentials.[71] The remarkable difference in pitting potential E_p confirmed that the pH, anodic potential and more importantly the type of anions in solution controlled the initiation and growth of pitting on aluminum.

3.3.4 Chronoamperometry

Chronoamperometry tests were carried out on aluminum electrodes at 0.85 V, a potential below the positive vertex of stability windows obtained from LSV, for a period of 24 hours and are presented in figure 3.6. In 2 M Li_2SO_4 solution (figure 3.6a) at pH 5, pH 7 and pH 9, the current density declined to 10^{-5} $A \cdot cm^{-2}$ levels after the first few seconds of the test and remained stable through the remainder; current density at pH 5 and pH 9 were close but slightly higher than that at pH 7. At pH 11, however, the current density gradually declined during the first 0.85 hours but then increased sharply to mA cm^{-2} levels, almost three orders of magnitude higher than the other pH conditions. Severe pitting was visible on the electrode after the test at pH 11 and even part of the 20-micron thick foil was perforated. Figure 3.6b shows the data obtained in 5 M $LiNO_3$ at the four pH values, the anodic current densities remained at a steady state of 10^{-6}

66

A·cm^{-2} level through the end of the tests. Although the current density at pH 11 was higher than other electrodes at the initial 4 hours, it gradually falls even below others. The low current intensity indicated that aluminum was well passivated under the effect of concentrated nitrate anions. AA1085 presented different pitting-resistance in 2 M Li$_2$SO$_4$ and 5 M LiNO$_3$ electrolytes. Based on the change of current density with time, the development of pitting in 2 M Li$_2$SO$_4$ electrolyte at pH 11 can be separated into three stages, which are indicated in figure 3.6a. At stage I, the hydroxide ions preferably adsorb on surface defect such as passive film flaws and intermetallic sites so metastable pits developed at a potential below the pitting potential. At stage II, stable pit growth occurs and aluminum dissolved at high rates after the incubation period at stage I. The hydrolysis of aluminum results in a reduction of pH value in aluminum pits thus the current density slowly dropped to lower values at stage III and the pitting growth is slowed down. The severe damage to aluminum foil caused by the pitting indicates that aluminum is not electrochemically stable in 2 M Li$_2$SO$_4$ solution of pH 11 when it is anodically polarized to 0.85 V within the stability window. However, aluminum presents good resistance to rapid localized corrosion in 5 M LiNO$_3$ solutions at such anodic polarizing potentials at the same pH.

3.3.5 Surface morphology

Surface morphology after CV

The surface morphology of electrodes after CV tests in 2 M Li$_2$SO$_4$ electrolytes were examined and compared in figure 3.7. At low magnification (figure 3.7a), the surfaces of electrodes tested in electrolytes at pH 7 are free of any localized corrosion, although the surfaces showed slight roughness under high magnification (figure 3.7b). The surface morphology of electrodes tested at pH 5 and pH 9 appeared similar to that at pH 7 thus the images thus were not

presented. At pH 11, small amounts of pitting were found scattered on the electrode (figure 3.7c). The pitting formed around intermetallic particles, mostly Al_3Fe or Al-Fe-Si intermetallic particles present in AA1085, which are so called "circumferential" pitting. This indicates the occurrence of galvanic cell corrosion between the intermetallic and aluminum matrix in 2 M Li_2SO_4 aqueous solutions. The electrode at pH 11 also exhibited more roughness compared to the other electrodes (figure 3.7d). The rough surface was ascribed to general corrosion that occurred during polarization in alkaline conditions.
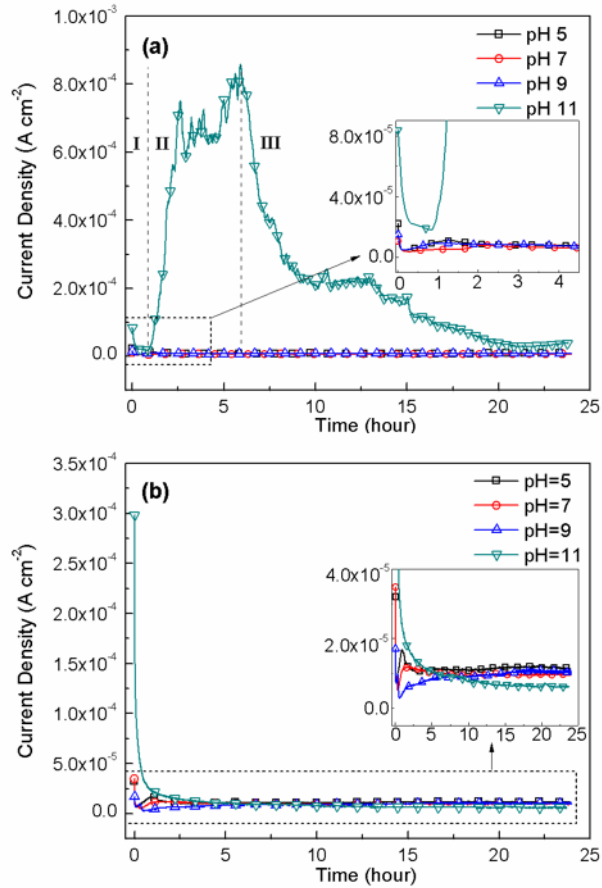
Figure 3.6 Chronoamperometry measured on Al foil in (a) 2 M Li_2SO_4 and (b) 5 M $LiNO_3$ at different pH values for a period of 24 hours.
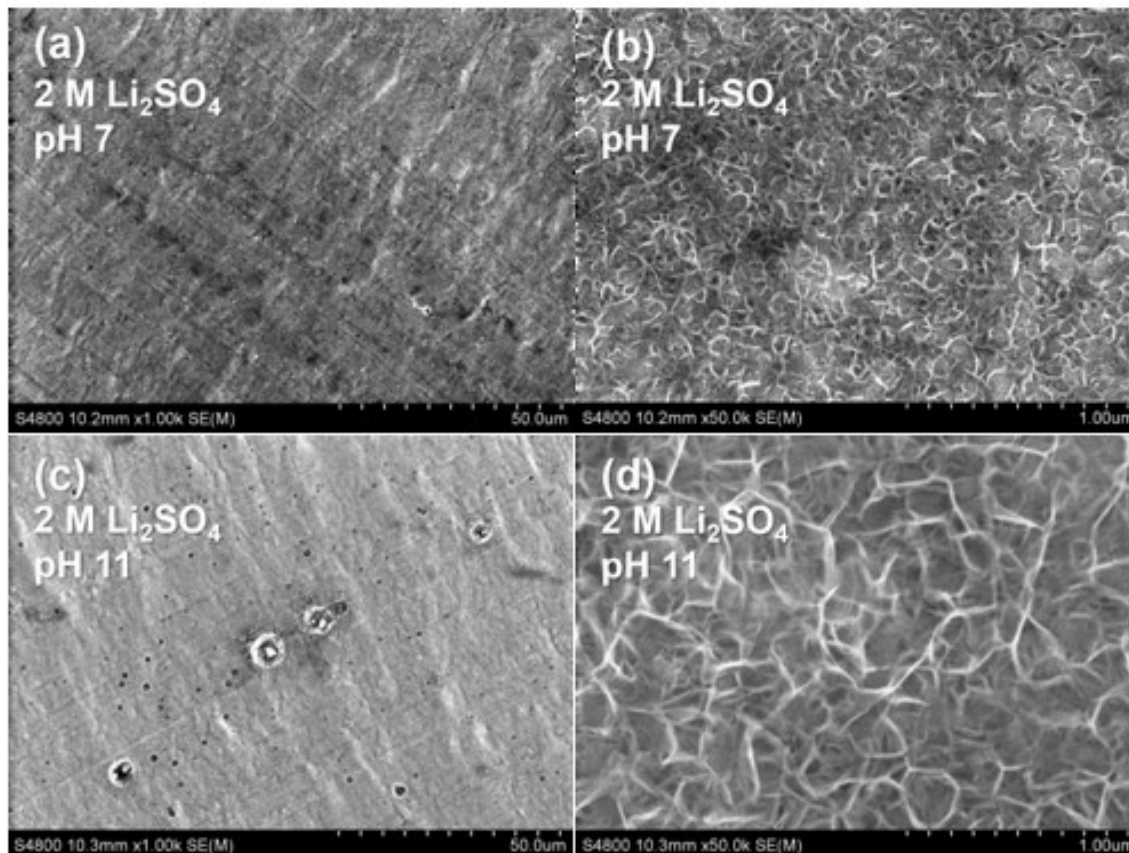
Figure 3.7 Surface morphology of Al electrodes after cyclic voltammetry in 2 M Li$_2$SO$_4$ at (a) pH 7, × 1000, (b) pH 7, × 50,000, (c) pH 11, × 1000 and (d) pH 11, × 50,000.

Small scattered circumferential pitting was detected on the electrode at pH 9 (figure 3.8a, b) after being reversibly scanned in 5 M LiNO$_3$ solution. At pH 11, a uniform layer of corrosion product was found (figure 3.8c, d). At a few locations the corrosion product layer fell off due to its expansion difference with the matrix during drying and it clearly showed that the thickness of the film was around 1 μm (figure 3.8e, f). The formation of this corrosion product layer with considerable thickness proves that considerable amounts of aluminum was oxidized during cyclic voltammetry and the corrosion product precipitated on the aluminum surface, which correlates to the high current density obtained in cyclic voltammetry tests. Since this thick corrosion product layer was only observed in 5 M LiNO$_3$ electrolyte at pH 11, it is deduced that

the corrosion product was formed due to the co-existence of nitrate and hydroxide in that electrolyte.
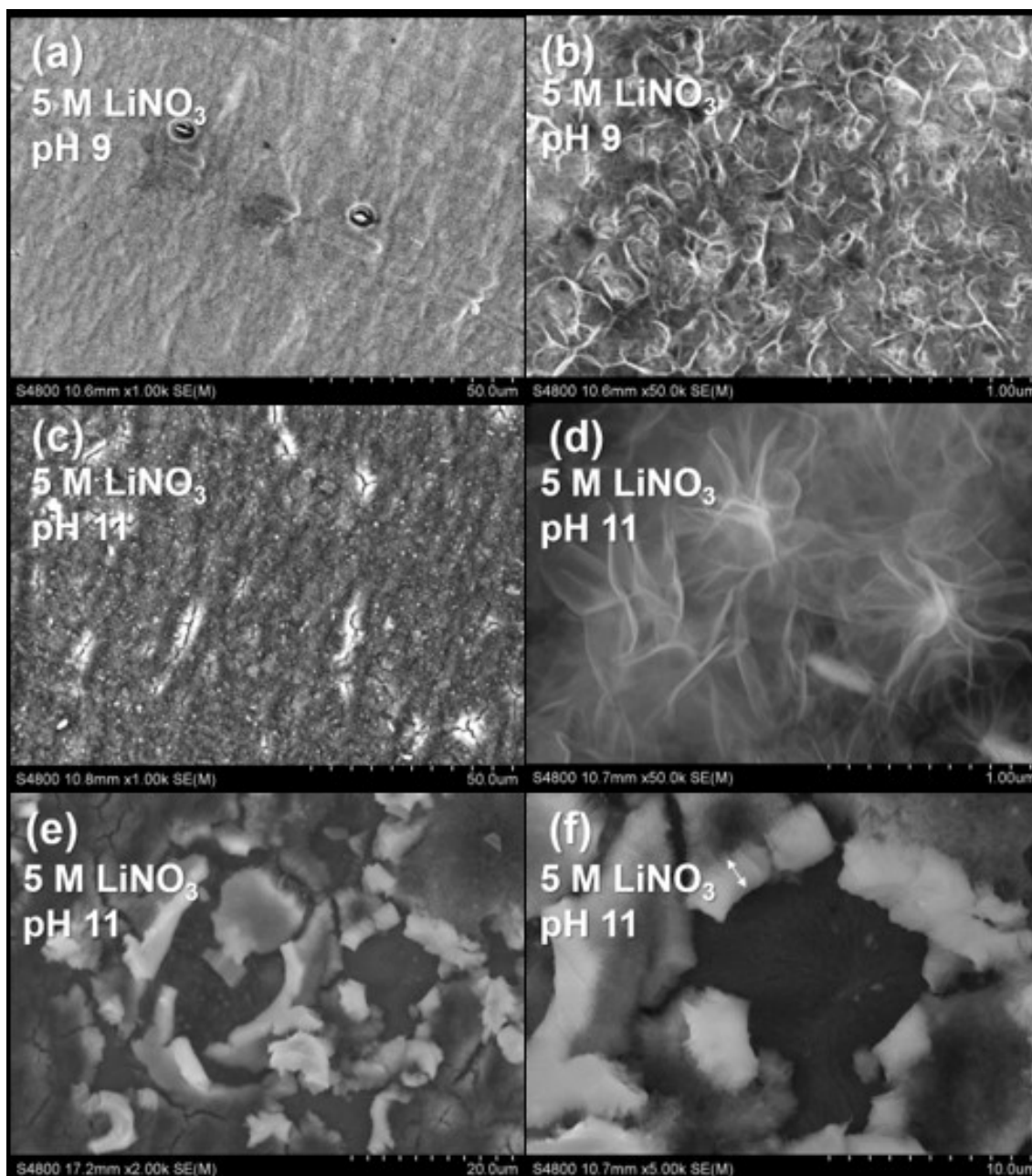
Figure 3.8 Surface morphology of Al electrodes after cyclic voltammetry in 5 M LiNO$_3$ at (a) pH 9, ×1000, (b) pH 9, ×50,000, (c) pH 11, ×1000, (d) pH 11, ×50,000, (e) surface corrosion products at pH 11, ×2000 and (f) surface corrosion products at pH 11, ×5000.

Surface morphology of pitting after chronoamperometry

After anodic polarization for 24 hours in 2 M Li_2SO_4 solution with pH 11, the perforated aluminum electrode was examined under SEM and the surface morphology is presented in figure 3.9. Severe localized corrosion occurred on the electrode tested at pH 11 and part of the foil was completely corroded away (figure 3.9a). There was clear evidence of crystallographic etching with square cross-sections observed inside the pits (figure 3.9b). The presence of the geometric facets inside pits is the result of preferable attack along well-defined crystallographic directions. This form of corrosion is identical to the crystallographic corrosion with {100} facets on aluminum or aluminum alloys in citrate solution and chloride solution reported by other authors. [72] This corrosion was presumably caused by the minimum elastic modulus, lowest intensity, and lowest interatomic bonding force in this crystallographic direction of aluminum.
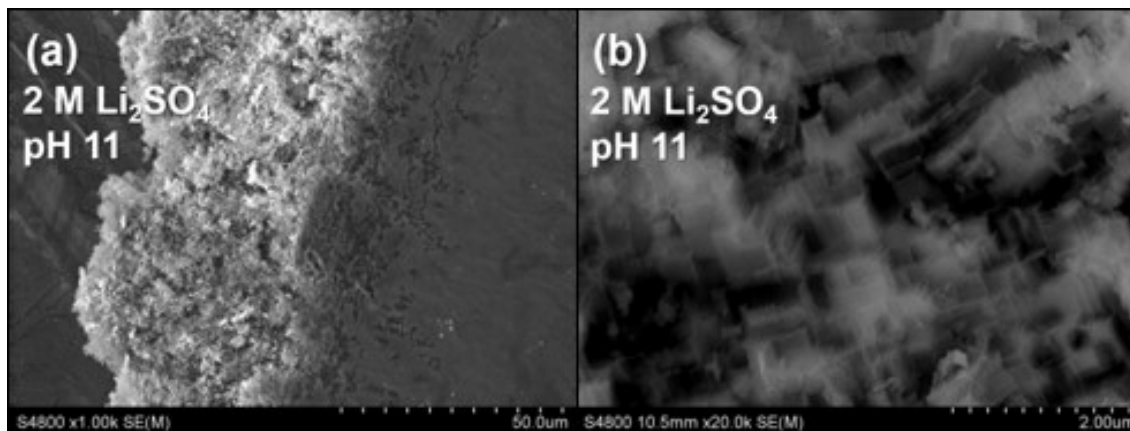
Figure 3.9 Morphology of pitting formed on Al electrode after chronoamperometry test in 2 M Li_2SO_4 electrolyte at pH 11, (a) × 1000, (b) × 20,000.

3.3.6 Raman Spectroscopy

The different morphologies observed on electrodes by SEM indicate that composition of surface passive films may be distinct under the effect of pH and electrolytes. The composition of

the surface passive layer plays an important role in determining the stability of aluminum current collectors. For instance, it was reported that aluminum suffers serious localized corrosion in organic-based lithium ion batteries containing bis(fluorosulfony) imide solvent. However, the addition of $LiPF_6$ in the solvent allows the formation of a low-solubility strong passivation AlF_3 film on aluminum that is capable of protecting the substrate from pitting corrosion.[35] Thus studying the structure and composition of aluminum passive film has been a focus of interest. Figure 3.10 shows the Raman spectra of aluminum electrodes after cyclic voltammetry measurements. The results are compared to the spectrum obtained from a cleaned as-received aluminum foil. The spectrum of the baseline aluminum foil presented a very broad band in the region between 600 cm^{-1} and 1200 cm^{-1} with relative low intensities, which indicates that the passive film on the surface is amorphous. This is in agreement with the well-accepted knowledge that an amorphous alumina with the thickness of 2 - 4 nm forms on aluminum under ambient conditions and the band is assigned to amorphous alumina. For the electrodes tested in Li_2SO_4 electrolytes (figure 3.10a), the spectra obtained at pH 5, 7 and 9 exhibited the same broad band between 600 cm^{-1} and 1200 cm^{-1}. A broad peak between 2800 cm^{-1} and 3000 cm^{-1} with low intensity was detected at pH 5 and 9, which was assigned to O-H stretching modes due to an outer layer of hydrated alumina,[5,73] The spectrum at pH 11, however, was characterized by sharp bands at 598 cm^{-1}, 983 cm^{-1}, 1067 cm^{-1}, 1389 cm^{-1} and 1519 cm^{-1}. For the electrodes tested in $LiNO_3$ electrolytes (figure 3.10b), the broad band corresponding to alumina only existed at the pH 5 condition. Bands with relatively low intensities were obtained at pH 7 and pH 9. At pH 11, sharp bands presented at 718 cm^{-1}, 1058 cm^{-1}, 1392 cm^{-1} and 1516 cm^{-1}. A broad band also existed in the wavenumber range between 3447 cm^{-1} and 3750 cm^{-1}. The band positions and

broadness are compared to band parameters reported in literatures and carefully analyzed.[73–77] The band components, the referenced literature and the tentative assignments for the spectrums are presented in table 3.3.
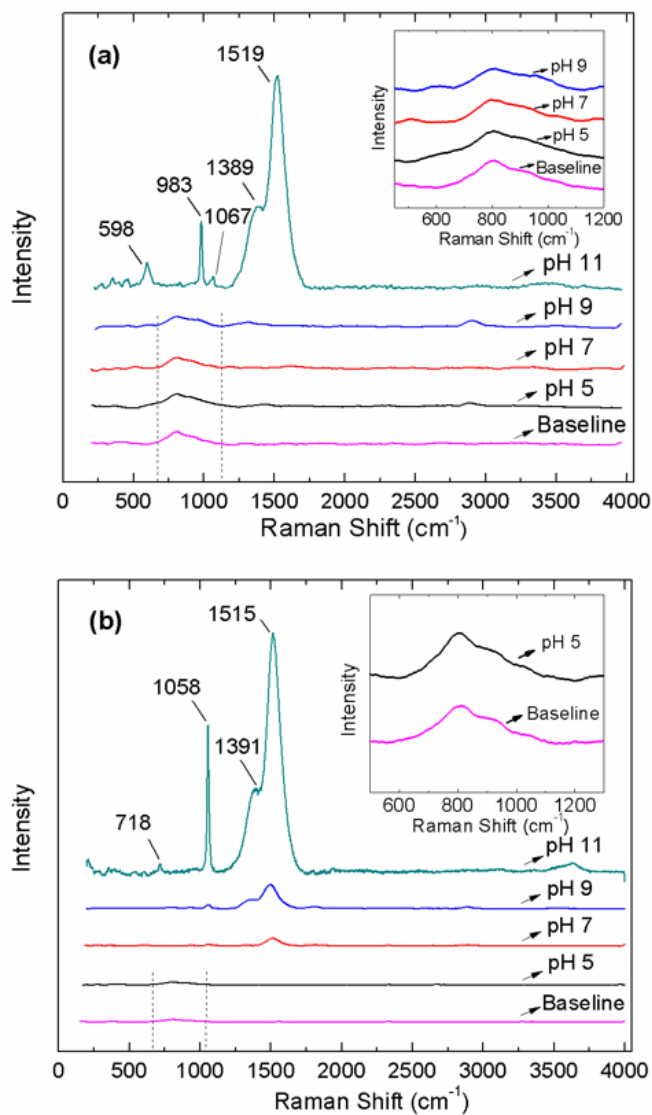
Figure 3.10 Raman spectra of Al electrodes after cyclic voltammetry in (a) 2 M Li_2SO_4 and (b) 5 M $LiNO_3$ at different pH values. The baseline samples shown are cleaned as-received foils not subjected to any electrochemical exposure.

Table 3.3 Band component analysis of Raman spectra obtained on Al electrode after cyclic voltammetry in ARLB electrolytes.

Electrode		Band Position (cm⁻¹)	Band Width (cm⁻¹)	Tentative Alignment
Plain Aluminum foil		803	466	Amorphous Al_2O_3
2 M Li_2SO_4	pH 5	805	595	
		2879	197	O-H stretching modes [73]
	pH 7	801	440	Amorphous Al_2O_3
	pH 9	808	462	
		2901	229	O-H stretching modes [73]
	pH 11	598	109	v_2 SO_4 triplet [74]
		983	63	v_1 SO_4 [74]
		1067	57	Al-O and Al-OH bending mode [73,75,76]
		1389	210	H_2O coordinated to AlO_4 [76]
		1519	312	H_2O coordinated to AlO_6 [76]
5 M $LiNO_3$	pH 5	803	461	Amorphous Al_2O_3
	pH 7	1059	64	NO_3 symmetric stretching [78]
		1511	271	H_2O coordinated to AlO_6 [76]
	pH 9	1056	65	NO_3 symmetric stretching [78]
		1354	158	H_2O coordinated to AlO_4 [76]
		1497	309	H_2O coordinated to AlO_6 [76]
	pH 11	718	45	NO_3 [78]
		1058	89	NO_3 symmetric stretching [78]
		1392	213	H_2O coordinated to AlO_4 [76]
		1516	298	H_2O coordinated to AlO_6 [76]
		3630	305	OH stretching modes [73]

The analysis of Raman spectra shows that within the stability window, the amorphous alumina layer remained stable in 2 M Li_2SO_4 electrolytes at pH 7 and was slightly hydrated at pH 5 and pH 9. Once the pH increased to pH 11 the amorphous passive film was destroyed due to the attack of OH⁻. Notably the band at 599 cm⁻¹ and 982 cm⁻¹ was ascribed to the v_2 andv_1 of SO_4^{2-}. The band assignments showed the coexistence of sulfate, hydroxyl, and Al-OH bands,

which indicates the adsorption of sulfate on aluminum surface. In 5 M $LiNO_3$ electrolytes, the surface passive film remained amorphous only in acidic pH 5 condition. The bands with strong intensity at 1391 cm^{-1} and 1515 cm^{-1} presented at pH 7, 9 and 11 conditions were assigned to H_2O associated to AlO_4 and AlO_6, which are associated to the hydrated surface and presence of hydroxide on aluminum.[76] The sharp band at 718 and 1058 cm^{-1} were due to the presence of nitrate on the corrosion product layer formed at pH 11.

3.3.7 Concentration of dissolved Al3+ after CV

Dissolved aluminum in electrolytes after cyclic voltammetry were measured by ICP and the results are presented in table 3.4. In both Li_2SO_4 and $LiNO_3$ solutions at pH 5, pH 7 and pH 9, very low concentrations of dissolved aluminum were detected in the electrolyte. At pH 11, 3.27 ppm of aluminum was measured in 2 M Li_2SO_4 electrolyte and 90.47 ppm of aluminum was measured in 5 M $LiNO_3$ electrolyte. The amount of dissolved aluminum with the change of pH of aqueous solutions presents a trend similar to the predicted aqueous stability of crystalline and partially amorphous aluminum oxides by D. Tromans,[79] where an increased aluminum solubility was expected when pH increases from 5 to 11. As calculated by the thermodynamic based model, the solubility of Al_2O_3 covered aluminum was predicted to increase at least four orders of magnitude when pH value changes from 5 to 11. The experimental results of dissolved aluminum after CV in 2 M Li_2SO_4 and 5 M $LiNO_3$ electrolytes are not showing such a large difference, which confirmed the existence of inhibition effects of nitrate anions and sulfate anions on aluminum matrix during CV.

Table 3.4 Concentration of Al3+ in electrolytes after cyclic voltammetry measured by ICP.

Electrolyte	pH value	Concentration of Al^{3+} (ppm)
2 M Li$_2$SO$_4$	5	0.15
	7	0.64
	9	0.74
	11	3.27
5 M LiNO$_3$	5	0.06
	7	0.16
	9	0.45
	11	90.47

3.4 Discussion

3.4.1 The inhibiting effect of anions

Anions acting as inhibitors could adsorb, compete with aggressive anions, and incorporate into passive films. This may repair passive film defects imparting better protective properties.[80] It was described that in aqueous solutions the pitting corrosion of aluminum might be affected by sulfate and nitrate anions. Especially when the electrode is anodically polarized, sulfate and nitrate anions would migrate toward the anode, adsorb on the aluminum surface and may even penetrate the passive film.[68] It was claimed that in solutions containing chloride ions, nitrate anions could incorporate into the oxide passive film of aluminum through chemical adsorption and impede the penetration of chloride ions and mitigate pitting corrosion. The addition of sulfate anions in chloride solution may also reduce the corrosion rate of pure aluminum and change the oxide film relaxation rate,[80] which was ascribed to the competitive adsorption between sulfate and chloride anions and possible physical blocking effect of sulfate anions, although the physical adsorption was revealed only occurring on top surface.

Based on the above results and analysis, the adsorption mechanisms of concentrated sulfate and nitrate anions on aluminum are proposed, specifically at slightly alkaline conditions. In the case of 2 M Li$_2$SO$_4$ electrolyte, severe localized corrosion only occurred at pH 11, the existence of a considerable amount of OH⁻ was considered to be a prerequisite to allow large-scale pitting growth on AA1085. OH⁻ ions can attack oxide passive film and aluminum matrix by the following reactions,[48,81]

$$Al_2O_3(s) + 2OH^- + 3H_2O \rightarrow 2Al(OH)_4^- \tag{3}$$

$$2Al(s) + 2OH^- + 6H_2O(l) \rightarrow 2Al(OH)_4^- + 3H_2(g) \tag{4}$$
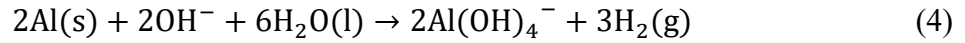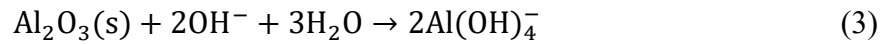
Under anodic polarization, Al metal could be oxidized into Al^{3+} and thus following reaction is also possible:

$$Al \rightarrow Al^{3+} \tag{5}$$

$$Al^{3+} + 3OH^- \rightarrow Al(OH)_3 \tag{6}$$

Due to the inevitable existence of Al-Fe and Al-Si-Fe intermetallic particles in AA1085, OH⁻ could cause the rapid depletion of Al metal at metastable sites by the formation of local galvanic cells and detrimental pitting can evolve rapidly. As it was revealed by Raman spectra, there was presence of sulfate on aluminum surface after cyclic voltammetry in 2 M Li$_2$SO$_4$ at pH 11. When sulfate ions adsorb on aluminum surface, the formation of basic aluminum sulfate may occur by the following reactions,[82]

$$Al^{3+} + SO_4^{2-} \rightleftarrows AlSO_4^+ \tag{7}$$

$$AlSO_4^+ + OH^- \rightleftarrows Al(OH)SO_4 \tag{8}$$
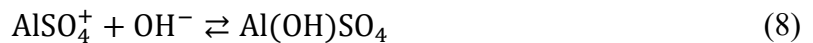
Sulfate anions carry a negative charge, which suggests that OH$^-$ anions would be repelled from the preferential adsorption sites, where pitting corrosion usually initiates. Therefore, a competitive adsorption between SO_4^{2-} and OH^- on electrode surface is expected. Under anodic polarization, the electrical energy served as the driving force to activate these reactions. Thus a corrosion product layer comprised of aluminum-hydroxide-sulfate was formed. This stable, basic salt will impede the migration of OH$^-$ and prevent the further dissolution of aluminum. However, as it was found in chronoamperometry, although the current density remained at low level initially due to the basic aluminum salt, this sulfate-incorporated passive layer is not capable of inhibiting aluminum matrix over long periods under a high anodic potential. The breakdown of the basic aluminum sulfate film may be explained by its low thermodynamic stability in alkaline solutions [83]. Sulfate alone would not be considered as an ideal inhibitor for aluminum due to its limited effectiveness on inhibition. However, when applied together with other inhibiting species it might play a role on raising the protective efficiency of the inhibitor package.

Nitrate affects the electrochemical stability of aluminum by a different inhibiting mechanism than with sulfate anions. The surface morphology of AA1085 after CV in 5M LiNO$_3$ at pH 11 showed the formation of a thick and compact corrosion product film, which could act as a barrier between aluminum metal and the electrolyte. It was reported that in alkaline conditions, nitrate reduction takes place with the presence of aluminum powder. The principle product is aluminum hydroxide and ammonia, with nitrite anion and nitrogen gas as intermediate product, [84,85]

$$3NO_3^- + 2Al + 3H_2O \rightarrow 3NO_2^- + 2Al(OH)_3 \qquad (9)$$

$$NO_2^- + 2Al + 5H_2O \rightarrow NH_3 + 2Al(OH)_3 + OH^- \qquad (10)$$

$$2NO_2^- + 2Al + 4H_2O \rightarrow N_2 + 2Al(OH)_3 + 2OH^- \qquad (11)$$
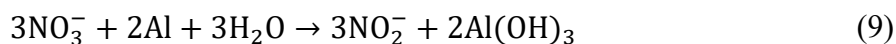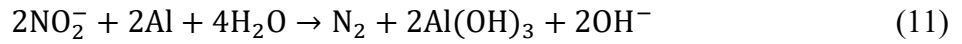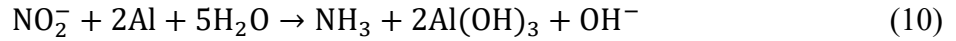
Once the passive film was dissolved by the attack of OH⁻ and fresh aluminum matrix was exposed to the electrolyte, the adsorbed NO_3^- and OH^- will react with aluminum and aluminum hydroxide forms on aluminum surface. The vigorous formation of an aluminum hydroxide layer on the surface explains the high capacitance in the cyclic voltammetry at pH 11 in 5 M LiNO₃. Growth of such a film impedes the migration of aggressive anions and results in the gradually reduced current density after each consecutive cycle. Brett et al. reported that nitrite is an effective corrosion inhibitor on aluminum in near-neutral aqueous chloride solutions [71]. The presence of NO_2^- due to reaction (9) is expected to aid the inhibition effect on aluminum by the competitive adsorption between nitrite and hydroxide anions on aluminum surface. As Raman spectrum showed the presence of nitrate on aluminum in 5 M LiNO₃ at pH 11, it is deduced that the chemical adsorption of nitrate occurred on the top surface of aluminum and the growth of the Al(OH)₃ layer is controlled by the mass transfer across the corrosion product layer.

The concentration of dissolved aluminum ions in test solutions depends on the rate of removal of the aluminum from the metal/passive film interface towards bulk solution by diffusion. The formation of basic aluminum sulfate in 2 M Li₂SO₄ electrolyte and Al(OH)₃ in LiNO₃ electrolyte at pH 11 could explain the different amounts of dissolved aluminum after CV tests. Basic aluminum sulfate was shown to have cation-selectivity.[86] When a cation-selective diffusion layer is formed on aluminum, the ion transportation between substrate metal and electrolyte is dominated by cations. The migration of OH⁻ through the passive film layer is impeded, which contributes to the stability of aluminum. The formation of the Al(OH)₃ film in 5

M LiNO$_3$ electrolyte is attributed to a general corrosion process over the entire aluminum surface. More importantly, this film is not ion-selective and its solubility in alkaline solution is high. Therefore, free exchange of Al^{3+} and OH$^-$ still occur between the aluminum matrix and the aqueous solution until the formed layer is sufficiently thick to impede the migration of ions. These conclusions are further confirmed by comparing the results obtained in chronoamperometry tests. In 2 M Li$_2$SO$_4$ electrolyte of pH 11, the stability at the start of the test is primarily ascribed to the formation of the cation-selective film. In 5 M LiNO$_3$ electrolytes, the continuous growth of the Al(OH)$_3$ layer resulted in the gradual decline of current density.

3.4.2 Material selection for current collector in ARLB

According to the Pourbaix diagram, within the potential range defined by the stability window, aluminum is stable when pH value is between 4 and 8 but corrosion will occur beyond this pH range. Although it describes the fundamental thermodynamics of reactions that determines the corrosion behavior of aluminum, it does not take account of the passive film formed on aluminum that may impede aggressive anions, which may act as corrosion rate limiting step. Based on the results obtained, aluminum presented high electrochemical stability within the pH range between 5 and 9 in both electrolytes. At pH 11 the existence of high concentration of sulfate and nitrate anions both result in the formation of protective passive films, by the previously proposed inhibiting mechanisms. However, the surface layer formed in Li$_2$SO$_4$ could not survive under the effect of anodic potential and a rapid dissolution of aluminum current collector occurred. At the same pH condition in 5 M LiNO$_3$ electrolytes, although the surface layer of oxide-hydroxide passive film protects aluminum well against dangerous localized corrosion, the considerable thickness of corrosion products formed by reaction (9), (10)

and (11) could increase the resistance between the current collector and cathode active material to the detriment of cell performance. Also a considerable amount of dissolved aluminum was detected in $LiNO_3$ electrolyte after CV test. Considering the aforementioned three possible harmful effects on battery performance when current collector corrodes, it risks the adverse impacts of (i) reduction of effective interfacial area between electrolyte and cathode electrode and (iii) contamination of electrolytes when aluminum is used at pH 11 in 2 M Li_2SO_4 electrolyte, (ii) increased internal impedance and (iii) contamination of electrolytes at pH 11 in 5 M $LiNO_3$ electrolyte. In these high pH conditions, the use of materials that are resistant to alkaline attack, e.g. stainless steel, may be preferred.

3.5 Conclusion

In aqueous electrolytes, the electrochemical stability of aluminum was influenced by the pH value, the concentrated anion and the anodic polarization potential. The results are concluded as follows:

1. The pH value of ARLB electrolyte has a direct impact on the stability of aluminum. Under anodic polarization aluminum remains passivated in pH 5, 7 and 9 in aqueous electrolytes. It risks severe localized dissolution at pH 11 in 2 M Li_2SO_4 electrolyte but it is well protected from pitting in 5 M $LiNO_3$ electrolyte at pH 11 due to the formation of thick corrosion product barrier layer.

2. Both concentrated sulfate and nitrate anions could assist inhibiting aluminum pitting though competitive chemical adsorption with OH⁻ in slightly alkaline solutions. Sulfate ions were incorporated into the aluminum surface passive film in alkaline solution and form an ion-selective basic aluminum salt film while nitrate ions weren't.

3. Aluminum presented good electrochemical stability at pH 5, pH 7 and pH 9 in both aqueous electrolytes. At pH 11, although sulfate and nitrate anions are capable of inhibiting aluminum pitting corrosion, however, the limited inhibiting effects of sulfate anions and the thick corrosion product layer formed in nitrate-contained electrolytes would eventually lead to deterioration of battery performance.

CHAPTER 4 Effects of Sulfate and Nitrate Anions on Aluminum Corrosion in Slightly Alkaline Solution

4.1 Introduction

Aluminum finds a wide range of technology applications due to its distinct properties such as low density, high energy density and considerable corrosion resistance. Study on the mechanism and the kinetics of aluminum corrosion, especially the localized corrosion of aluminum, is a particular research interest because the corrosion, especially localized corrosion, often leads to the sudden failure of materials and impair the function of aluminum components. In lithium-ion batteries, commercial purity AA1085 is widely used as current collector material. Corrosion of aluminum current collector irreversibly increases the internal battery resistance, contaminates electrolyte, attacks the electrode material and consequently degrade the battery performance, life and even safety.[2,29,31] The recent developed aqueous rechargeable lithium-ion battery (ARLB) technology has raised concerns on the possible corrosion of current collector in aqueous battery electrolytes. To ensure the chemical stability of specific cathode active materials, the electrolytes of ARLB are usually adjusted to slightly alkaline condition, e.g. pH 11, which is beyond the stability window of aluminum predicated by Pourbaix diagram as pH 4 - 8.[17] Prior works have identified 2 M Li_2SO_4 and 5 M $LiNO_3$ aqueous solutions as high performing ARLB electrolytes.[67] The highly concentrated salt solution and the alkaline pH value adds more complexities on the stability of aluminum in ARLB systems.

Attempts have been made to understand the effects of sulfate and nitrate anions on aluminum corrosion, but so far there are some discrepancies in the literature. Poggi et al. claimed that addition of 0.01 to 0.1M SO_4^{2-} mitigates high-purity aluminum corrosion in slightly

alkaline solution by competitive adsorption mechanism.[87] It was claimed that the sulfate anions significantly retard the crystallization of gibbsite from amorphous aluminum oxide in aqueous solution.[88] Using electrochemical noise analysis, K.H. Na reported that the presence of SO_4^{2-} and NO_3^- enhance the alkaline corrosion of high-purity aluminum.[89] Branzoi reported that addition of 0.05 M and 0.1M hydroxyl anions and 1 M NaNO₃ solution lead to extensive localized attack on aluminum.[70] While it was also described that nitrate combining with other inorganic anions could effectively inhibit aluminum corrosion in alkaline solutions.[90] The highly concentrated Li₂SO₄ and LiNO₃ electrolytes used in ARLB, which allows desirable stability of lithium anode and high conductivity, may intensify the effects of sulfate and nitrate anions on aluminum corrosion. Research on the stability of aluminum in alkaline solutions containing sulfate and nitrate anions is required for a better understanding on the role of ARLB electrolyte on the corrosion behavior of aluminum current collector. Yamada et al. reported that concentrated LiFSA-based electrolytes effectively suppress aluminum corrosion up to 4.5V versus Li⁺/Li.[91] The inhibiting effect of the concentrated electrolytes was explained by the declined activity of free solvent molecules. Therefore, it is helpful to understand the relationship between the stability of aluminum and the structure of concentrated aqueous electrolytes. The purpose of present work is to throw more light on the specific role of sulfate anions and nitrate anions play on aluminum corrosion in slightly alkaline solution. Detailed discussion was made on the influence of the type of anion, anion concentration and applied anodic potential on the kinetics of aluminum corrosion. This study is rendered necessary by the importance of corrosion management in the design of aqueous based energy storage systems and the extensive use of aluminum and aluminum alloys in many industrial applications.

4.2 Experimental

4.2.1 ARLB electrolyte

The electrolytes are prepared by dissolving specific weight of LiOH (anhydrous, 98%, Alfa Aesar) in de-ionized water to adjust the pH to 11, followed by addition of lithium salts to target concentrations of 0.1M, 0.5M and 2M of Li_2SO_4 (anhydrous, 99.7%, Alfa Aesar); 0.1M, 2M and 5M of $LiNO_3$ (anhydrous, 99.98%, Alfa Aesar) equivalent. The solution was magnetic stirred until the salts were fully dissolved and the pH of electrolytes was again adjusted to 11. The pH value was monitored using a Mettler FE20 Ag/AgCl pH electrode.

4.2.2 Electrochemical tests

Electrochemical tests were conducted using PARSTAT-4000 in a conventional three-electrode plate material evaluating cell (BioLogic Science Instruments) that allows a constant electrode area of 0.5 cm^2. Ag/AgCl with saturated KCl (0.197 V vs SHE) solution was used as the reference electrode. The reference electrode was separated from the body of the cell using a luggin capillarty to minimize the IR drop. A platinum wire with surface area of approximately 1 cm^2 was used as the counter electrode. The stability window of prepared aqueous electrolytes was determined by performing linear sweep voltammetry on high purity platinum foil in aqueous electrolytes scanned from open circuit potential either to the anodic or the cathodic direction with a scanning rate of 1 mV/s until significant gas evolution occurs The platinum foil and the platinum counter electrode were cleaned with dilute nitric acid, rinsed with distilled water and air dried before each measurement. As received AA1085 foil of thickness 20 μm was rinsed with isopropyl alcohol, acetone and air-dried prior to testing. The open circuit potential (OCP) of AA1085 was measured after stabilization in aqueous electrolytes for 2.5

hours. The OCP on AA1085 in 0.1 M, 0.5 M, and 2 M Li_2SO_4 electrolyte was -1.041 V, -1.12 V and -1.083 V, respectively. In 0.1 M, 2 M and 5 M $LiNO_3$ electrolytes, the measured OCP was -1.081 V, -0.834 V and -1.058 V, respectively. Chronoamperometry was carried out on fresh AA1085 foil in aqueous electrolytes at a selected anodic potential for a period of 24 hours. After the electrochemical tests, the aluminum electrode was immediately removed from the cell, gently rinsed with DI water and dried using a gentle stream of nitrogen for following characterization. Each test was performed at least three times and the representative data are reported. All potentials value in this paper are reported in Ag/AgCl, Saturated KCl (0.197 V vs SHE) scale.

4.2.3 Surface characterization

The surface morphology of the electrodes after choronoamperometry was examined by a Hitachi S-4800 scanning electron microscopy. X-ray photoelectron spectroscopy was performed using a Perkin Elmer 5440 X-Ray Photoelectron Spectrometer with Mg Kα source. The AA1085 electrode surface was sputtered by Ar^+ ion sputtering over an area of 4 mm^2 to analyze the chemical state of the passive film through the depth direction. The XPS spectra were recorded after the passive film was sputtered by Ar^+ ion for 0, 5, 10, 15, 20 and 25 minutes. Before the sputtering treatment, the etching rate was calibrated as 1 nm/min using atomic layer deposited alumina film of known thickness grown on silicon wafer surface. The carbon *1s* peak with a binding energy of 284.6 eV was used as the reference for spectrum calibration. The core level peaks were analyzed using a Tougaard-type background. The peak positions and areas were optimized using a weighted least squares fitting method with 80% Gaussian, 20% Lorentzian line shapes. Raman spectroscope microscopy was performed using a Renishaw Inc. 1000B. The Raman spectrum was excited by a helium-neon laser producing highly polarized light at 633 nm and collected in the range between

200 and 4000 cm^{-1}. The spectra were calibrated using the 519.5 cm^{-1} of a piece of silicon wafer. Raman spectrum was acquired with a 10 s integration time and the power at the sample was 10 mW. All measurements were taken at fixed parameters of the instrument to ensure a constant response function.

4.3 Results and Analysis

4.3.1 Stability window of solutions measured by LSV

The operating voltage range of ARLB is confined within the stability window of aqueous electrolyte. According to thermodynamic basics, the theoretical gas evolution potential can be calculated by: $E_{H^+/H_2} = -0.059pH$ and $E_{O_2/H_2O} = 1.23 - 0.059pH$. At pH 11, the theoretical stability window of aqueous electrolyte is 1.23 V, between -0.846 V and 0.384 V vs Ag/AgCl, KCl (sat'd) reference electrode. The actual stability windows of test electrolyte were measured by carrying out linear sweep voltammetry on platinum foil in aqueous solutions of different lithium salt concentration at pH 11. E_H and E_O, which denote the onset potential of hydrogen and oxygen evolution of aqueous solutions, are obtained and presented in table 4.1. The results show that the concentrated aqueous electrolytes reduce water activity and extend the stability windows beyond the theoretical value, which is in consistent with the phenomenon observed in prior works. [23]

Table 4.1 Gas evolution potentials and stability window of aqueous electrolytes measured by LSV.

Electrolyte	Concentration (M)	E_O (V)	E_H (V)	Stability Window(V)
Li$_2$SO$_4$, pH 11	0.1	0.893	-0.803	1.696
	0.5	0.895	-0.802	1.697
	2	0.88	-0.83	1.71
LiNO$_3$, pH 11	0.1	0.859	-0.807	1.666
	2	0.857	-0.844	1.701
	5	0.887	-0.898	1.785

4.3.2 Chronoamperometry

4.3.2.1 Effect of Anion Concentration

To investigate the effects of sulfate and nitrate anions on the kinetics of aluminum corrosion in slightly alkaline ARLB electrolyte, chronoamperometry was performed on AA1085 foil at 0.85 V, an anodic potential below the positive vertex of the operational stability windows, in solutions of different salt concentrations for 24 hours. As it is shown in figure 4.1, aluminum exhibited remarkable different current-time response in test solutions containing sulfate (figure 4.1a) and nitrate anions (figure 4.1b). In 0.5 M and 2 M Li$_2$SO$_4$ solution, the current density-time curves depicted four distinct stages, including an immediate decline of current density at the initiation of test, followed by a steady state for certain time period, then abrupt increase to considerable high values at mA scale and gradual decline to µA scale at the final stage, as is evident from the insets of figure 4.1a. In 0.1 M Li$_2$SO$_4$ solution, the first two stages occurred within 20 seconds and then the current density increase rapidly. The considerable level of current density and the apparent signal noise obtained in LiOH pH 11 solutions indicates the occurrence of pitting corrosion on electrode. The addition of 0.1 M Li$_2$SO$_4$ in pH 11 LiOH alkaline solution

88

resulted in significant higher current densities, which proves that the existence of sulfate anions promotes the growth of pitting on aluminum at slightly alkaline solution. After the polarization tests, severe pitting was visible on all aluminum foil tested in Li_2SO_4 electrolytes and LiOH pH 11 solution, which confirms that the rapid increase of current density was due to the growth of stable pitting. It is notable that the current density of AA1085 in 0.5 M and 2 M remained at μAcm^{-2} scale, one order of magnitude lower than that in LiOH pH 11 solution, before the occurrence of rapid pitting growth, which indicates that the pitting corrosion is suppressed for a period in these electrolytes. While in $LiNO_3$ electrolytes, the data plots only depicted an initial decline of current density and then it remained stable at μAcm^{-2} scale. No pitting was observed on the electrode after the chromoamperometry tests. The current density on AA1085 in $LiNO_3$ electrolytes is obviously lower than that obtained in LiOH pH 11 solution, which shows that pitting growth is suppressed in $LiNO_3$ electrolytes.
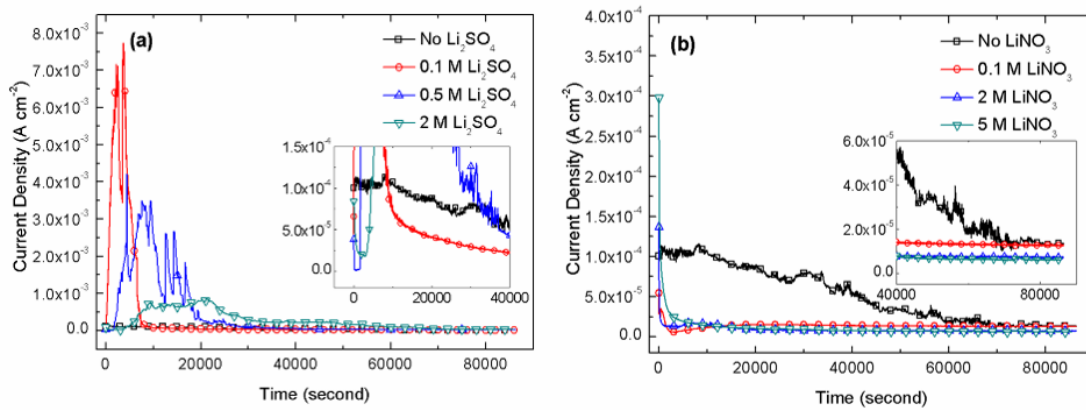
Figure 4.1 Chronoamperometry measured on AA1085 foil at 0.85 V in (a) Li_2SO_4 electrolytes and (b) $LiNO_3$ electrolytes at pH 11 for 24 hours.

The overall current density J in chronoamperometry are primarily contributed by the following four possible process, (i) charging of the electric double layer (J_c); (ii) growth of

89

passive film layer on aluminum due to repassivation (J_{gr}); (iii) dissolution of passive film or electro-dissolution of metal matrix (J_{diss}); and (iv) rapid dissolution of aluminum by pitting (J_{pit}). [80,92] These process can proceed concurrently on electrode thus in any stage thus the overall current density J is depicted by the following relationship,

$$J = J_c + J_{gr} + J_{diss} + J_{pit} \tag{1}$$

When an individual process dominated the reaction on electrode, the current corresponds to other processes are considered relatively small enough to be neglected. Each distinct stage of the chronoamperommetry curve represents one specific or combined process therefore the corrosion kinetics can be analyzed and compared.

In the curve obtained in 2 M Li_2SO_4 solution, the different stages in the curve are interoperated as follows: the initial decline in current density was primary caused by the growth of hydrated aluminum passive film on aluminum surface; the steady-state current stage was ascribed to a close proceeding rate of electro-dissolution and growth of passive film process; the abrupt increase of the current in Li_2SO_4 solutions corresponds to the rapid growth of pitting on electrode; the hydrolysis of aluminum during pitting growth results in decreased pH value in the pit environment, therefore, the current density finally declined to low magnitudes at the final stage. The concentration of sulfate anions played a significant role on the current response. The peak value of pit growth current density (j_{pit}) reduced with increasing sulfate concentrations. To further study the kinetics of pitting growth on AA1085 in Li_2SO_4 electrolytes, the data in chromoamperometry curves where the current density increased sharply in figure 4.1a was extracted, fitted and presented in figure 4.2a. The current corresponds to pitting growth J_{pit} was

found proportional to the square root of time, $t^{1/2}$, which agrees with Hill's model described by the following relation,[93]

$$J_{pit} = At^{1/2}$$

The coefficient A, which describes the rate of pit growth, is defined by $A = 2.83zF\pi N_o D^{3/2} C^{3/2} M^{1/2} \rho^{1/2}$, z is the valence number, N_o is the number of sites for pitting growth, D is the diffusion coefficient, C is the concentration of aggressive ions, M and ρ are the molecular weight and the density of dissolve metal.[93] This type of current-time relation was depicted as a three-dimensional pitting growth under diffusion control.[92] When the linear portion of the curve is extrapolated to horizontal axis where J_{pit} is zero, the interception defines the incubation time t_i, which is required for pitting initiation before rapid growth. t_i marks the complete destruction of regional passive film layer and the attack of the aluminum substrate begins after t_i. The rate of pit nucleation t_i^{-1} is associated with the ingress rate of aggressive ions and determined by the ion selectivity of passive films.[94] The fitted pitting growth rate, incubation time t_i and rate of pit nucleation t_i^{-1} are presented in table 4.2. The fitted pitting growth rate and rate of pit nucleation declined with increasing Li_2SO_4 concentrations, which indicated that there are less available pitting nucleation sites at a higher concentration of sulfate anions. The results indicated that increasing the electrolyte concentration decreases the susceptibility of aluminum towards pitting corrosion. It is reasonable to assume that the highly concentrated sulfate anions are capable of inhibiting aluminum and impeding the pitting initiation under an applied anodic potential, although this protection is only functional within the limited incubation time period.
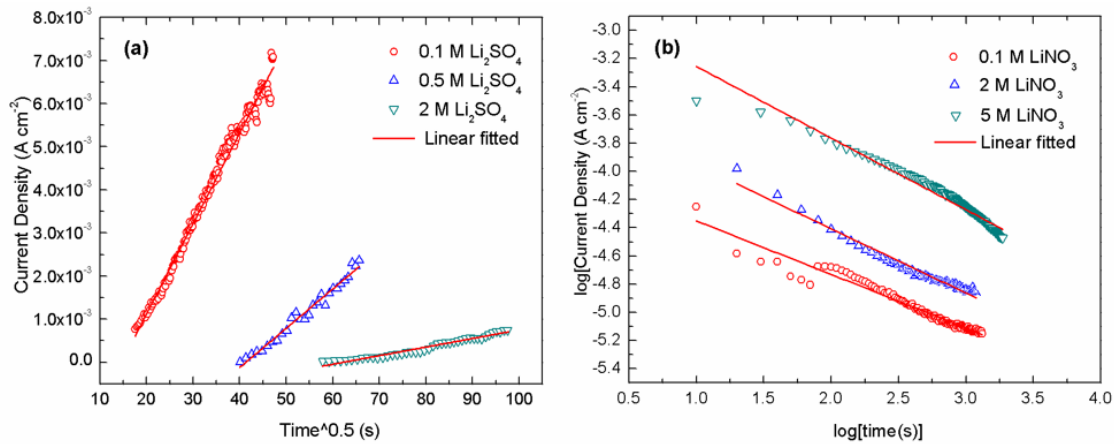
Figure 4.2 Fitted linear portion of (a) Jpit vs t0.5 and (b) Jgr vs log(time) extracted from chromoamperometry obtained in Li₂SO₄ and LiNO₃ electrolytes.

The chronoamperometry response of AA1085 in LiNO$_3$ solutions depicted an initial current decline from the scale of 10^{-4} to 10^{-6} Acm^{-2} and then remained at stable current density values through the end of the tests. Compared to the pitting growth observed in Li$_2$SO$_4$ electrolyte, the remarkable different response of AA1085 in LiNO$_3$ solution proved that in the presence of nitrate anions, the growth of passive film dominated the surface process, which protected aluminum from pitting corrosion. As it is shown in figure 4.2b, the declining current density showed a linear relationship with respect to elapsing time in logarithmic scale. According to the kinetics of repassivation on aluminum,[95,96] the relationship between current density response and elapsing time can be described by the following equation,

$$J_{gr} = bt^{-n}$$

where J_{gr} is the anodic current density associated to repassivation, t is the elapsing time, b is a constant and n represents the repassivation parameter. The value of n, which can be obtained by fitting the slope of the log(j) vs log(t) plot, is an indirect measure of the passive film growth rate.[97] The current density was plotted versus time in logarithmic scale and the slope of the plot

92

was fitted and compared. The passivation kinetics of aluminum is influenced by the concentration of nitrate anions. In 5 M, 2 M and 0.1 M of LiNO$_3$ solution, the value of n was -0.508, -0.454 and -0.379, respectively, which indicates that increasing the concentration of nitrate anions slightly enhance the growth rate of passive films on AA1085 in slightly alkaline condition.

4.3.2.2 Effect of anodic potential

Figure 4.3a and 4.4a present the chronoamperometry responses obtained on AA1085 at various applied anodic potentials in 0.1 M Li$_2$SO$_4$ and 5 M LiNO$_3$ solutions at pH 11. The effects of anodic potentials on the kinetics of pitting corrosion in 0.1M Li$_2$SO$_4$ electrolyte and the repassivation rate in 5 M LiNO$_3$ electrolyte were analyzed and fitted in figure 4.3b and 4.4b. The fitted kinetics parameters of pitting corrosion in 0.1 M Li$_2$SO$_4$ at various applied anodic potentials are presented in table 4.2. The fitted rate of pit growth (A) and the rate of pit nucleation t_i^{-1} increased with increasing anodic potentials. When the applied anodic potential was 0.775V, the current density remained at low values and no rapid increase of current density was observed during the 24-hour test, which indicates there is no occurrence of pitting at this condition. The dependence of pitting current (j$_{pit}$) response, rate of pit growth (A) and i the rate of pit nucleation t_i^{-1} on anodic potential suggests that there is a distribution of necessary anodic potentials for the proceeding activity at pit nucleation sites. There are larger numbers of activated pitting nucleation sites available for pitting growth at higher applied anodic potentials.
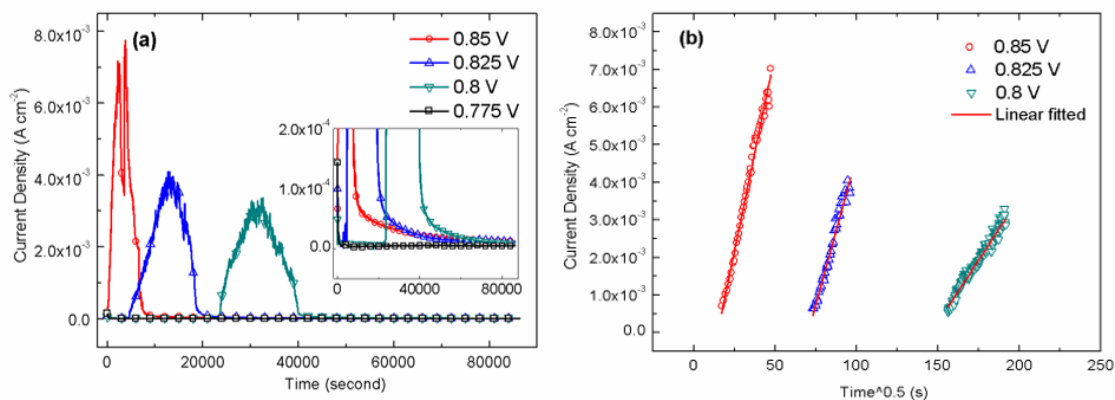
Figure 4.3 (a) Chromoamperometry measured on AA1085 foil in 0.1 M Li$_2$SO$_4$ at pH 11 and (b) fitted linear portion of Jpit vs t0.5 under different anodic potentials.
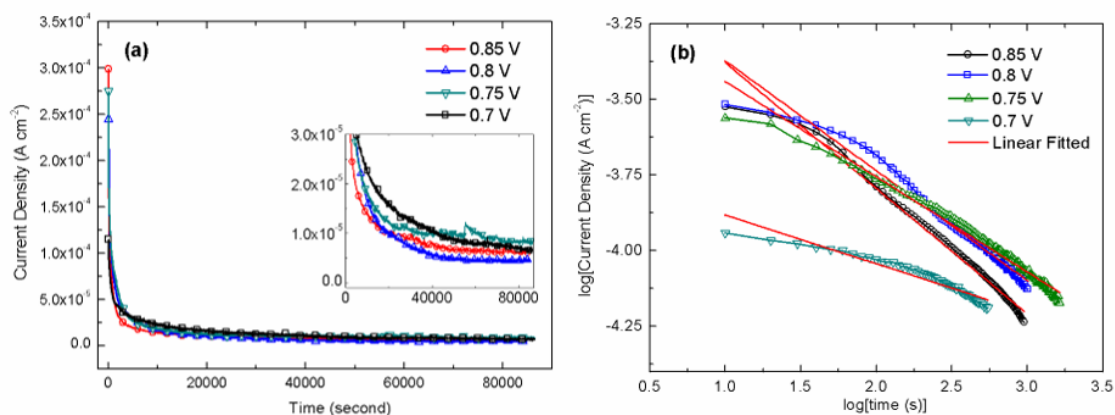
Figure 4.4 (a) Chromoamperometry measured on AA1085 foil in 5 M LiNO$_3$ at pH 11 and (b) fitted linear portion of Jgr vs log(time) under different anodic potentials.

The fitted passivation rates of AA1085 at different anodic potentials in 5 M LiNO$_3$ electrolyte are presented in table 4.3. In LiNO$_3$ solutions, the fitted repassivation rate increased with increasing anodic potentials, which confirmed that the growth of passive film was enhanced under a higher anodic potential.

Table 4.2 Kinetics parameters of the pitting corrosion on AA1085 in Li_2SO_4 electrolytes.

Electrolyte	Concentration (M)	Anodic Potential (V)	Rate of pit growth	Incubation time t_i (s)	Rate of pit nucleation t_i^{-1} (s^{-1})
Li_2SO_4 pH 11	0.1	0.85	2.10E-04	2.20E+02	4.55E-03
	0.5	0.85	9.13E-05	1.73E+03	5.79E-04
	2	0.85	1.99E-05	3.90E+03	2.56E-04
	0.1	0.825	1.56E-04	4.28E+03	2.34E-04
	0.1	0.8	6.76E-05	2.26E+04	4.43E-05
	0.1	0.775	-	-	-

Table 4.3 Fitted parameters for the repassivation rate on AA1085 in $LiNO_3$ electrolytes.

Electrolyte	Concentration (M)	Anodic Potential (V)	Repassivation Constant
$LiNO_3$ pH 11	0.1	0.85	0.379
	2	0.85	0.454
	5	0.85	0.508
	5	0.8	0.363
	5	0.75	0.315
	5	0.7	0.161

4.3.3 Surface morphology of electrodes after chromoamperometry

The surface morphology of AA1085 electrodes after chronoamperometry in 0.1 M Li_2SO_4 at 0.85 V for 24 hours is presented in figure 4.5. The AA1085 electrode polarized in 0.1M Li_2SO_4 solutions has the highest current density and pitting growth rate thus its representative surface morphology is shown to present the pit formed in Li_2SO_4 electrolytes. Clearly severe pitting corrosion was observed on the electrode surface and there is clear evidence of "crystallographic etching" with {100} facets inside the pits. The presence of the geometric facets inside pits is the result of preferable attack along well-defined crystallographic directions.[72] This form of pitting corrosion was presumably caused by the minimum elastic modulus, lowest

intensity, and lowest interatomic bonding force in specific crystallographic direction of aluminum.
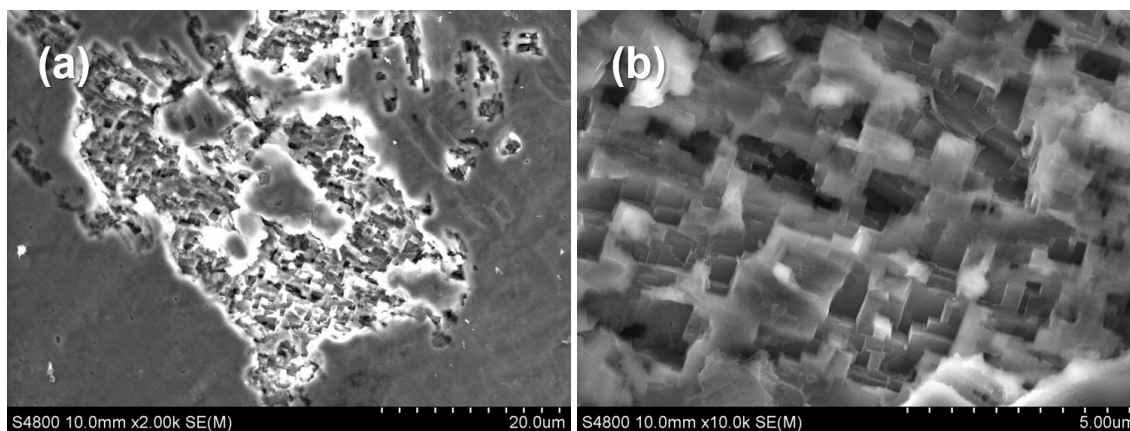
Figure 4.5 Surface morphology of AA1085 electrodes after chronoamperometry in 0.1 M Li_2SO_4 at 0.85 V for 24 hours (a) ×2000 and (b) ×10,000.

Figure 4.6a shows the surface morphology of AA1085 electrode after chronoamperometry at 0.85 V for 24 hours in 5 M $LiNO_3$ electrolyte. There was no sign of any pitting corrosion on the electrode surface. However, a layer of corrosion product film with considerable thickness covered on the electrode surface. The "cracking" feature on the corrosion product film formed due to the expansion difference between the corrosion product and the substrate during drying. The cross-section profile of the electrode was obtained and shown in figure 4.6b. The thickness of the corrosion product layer was approximately 2 μm.

4.3.4 Effect of sulfate and nitrate anions on composition of surface passive film

It is well accepted that a layer of amorphous alumina with the thickness of 2-4 nm forms on aluminum at ambient conditions. In alkaline solutions, the existence of a film layer on aluminum was proved in previous works.[88,98] Since the film can act as a barrier for the charge

transfer process between aluminum and aqueous solution, studying how the presence of anions species influence the structure and composition of aluminum passive film is important for better understanding of aluminum corrosion mechanism in aqueous solutions. The above electrochemical results revealed that the type of anions, the anion concentration and the applied anodic potentials played important role on the corrosion resistance of AA1085. It is presumed that the existence of concentrated sulfate and nitrate anions may change the chemical composition or the physical property of the passive film on AA1085. It was reported that sulfate and nitrate anions are effective pitting inhibitors for pure aluminum in NaCl solution by surface adsorption mechanisms.[68,99] At open circuit potentials nitrate ions can incorporate into aluminum passive film and its inhibiting mechanism against aggressive chloride ions was ascribed to chemical adsorption. It was claimed that sulfate anions do not incorporate into aluminum passive film and its inhibiting effect was due to the competitive adsorption with Cl^- ions, which was described as a physical adsorption process.[68] To investigate the effects of concentrated sulfate and nitrate anions on the chemical state of aluminum passive film in slightly alkaline solutions, chronoamperometry was carried out on AA1085 at 0.85V in 2 M Li_2SO_4 and 5 M $LiNO_3$ electrolytes at pH 11 for 2000 seconds, before the occurrence of rapid pitting growth. The AA1085 electrodes were subsequently disassembled, rinsed with deionized water, gently dried with air and immediately transferred into the vacuum chamber of XPS. The electrode surface was etched by Ar^+ sputtering by 0, 5, 10, 15, 20 25 minutes. The survey spectrum was measured and high-resolution XPS scans of Al *2p*, O *1s,* N *1s* and S *2p3/2* core-level peaks were also performed and analyzed.
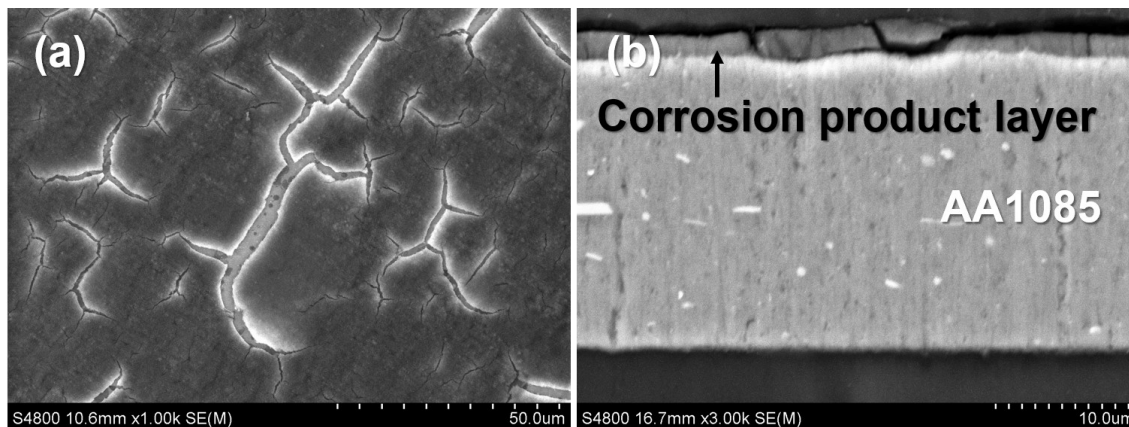
Figure 4.6 (a) Surface morphology and (b) cross sectional profile of AA1085 electrode after chronoamperometry at 0.85 V for 24 hours in 5 M LiNO$_3$ electrolyte.

Figure 4.7 shows the XPS survey scan results of AA1085 electrode surface without Ar$^+$ sputtering after 2000-seconds of chronoamperometry at 0.85 V. The presence of carbon signal was due to the adsorption of carbon dioxide on sample surface. In figure 4.7a, the survey spectrum of aluminum after chronoamperometry in 2 M Li$_2$SO$_4$ solution at pH 11 showed signals for oxygen, aluminum and sulfur. The presence of sulfur peak in survey spectrum is associated to the surface adsorption or incorporation of sulfate anions on aluminum surface. The survey spectrum (figure 4.7b) of aluminum after chronoamperometry in 5 M LiNO$_3$ solution at pH 11 only showed peaks of oxygen and aluminum. There was no evidence indicating the presence of nitrogen species, which suggests that nitrate anions were not chemically incorporated into the passive film on AA1085.
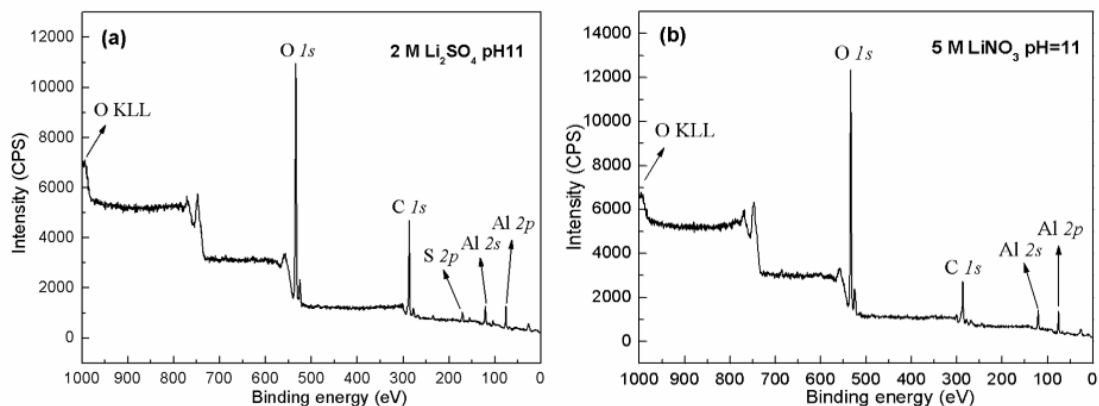
Figure 4.7 XPS survey scan results of AA1085 electrode surface without Ar+ sputtering after 2000-seconds of chronoamperometry at 0.85 V.

After cheomoamperometry in 2M Li_2SO_4 solution at pH 11, high resolution XPS scans of Al *2p* core-level peaks of AA1085 electrode after 0, 5, 10, 15, 20 and 25 minutes of Ar^+ etching are shown in figure 4.8. The spectrum without sputtering can be deconvolved into two Gaussian-Lorentzian subpeaks, centered at 73.62 and 74.23 eV. Considering the elemental composition of the electrode surface and reported binding energy values from literatures, these two subpeaks are assigned to aluminum sulfate $[Al_2(SO_4)_3 18H_2O]$[100] and basic aluminum sulfate $[(Al(OH)SO_4)]$.[101] After 5 min of Ar^+ sputtering, the subpeak corresponds to $Al_2(SO_4)_3 18H_2O$ disappeared, and the spectrum was deconvolved into two subpeaks centered at 74.24 and 75.22 eV, which were assigned to basic aluminum sulfate $[Al(OH)SO_4]$[101] and aluminum hydroxide $[Al(OH)_3]$.[102] and The spectrum showed another subpeak centered at 70.83 eV after 15 min of Ar^+ sputtering, which was associated to the aluminum matrix.[103] After 25 min of etching, the subpeak corresponds to basic aluminum sulfate disappeared and the shape of the spectrum remain the same even upon further Ar^+ sputtering, which indicates the completely removal of the passive film on electrode surface. The presence of the subpeak at 74.79 was due to the inevitable

99

residuals of oxygen species on aluminum surface. Figure 4.9 shows the high resolution XPS scans of the S $2p$ peaks for AA1085 electrode after chromoamperometry in 2 M Li_2SO_4 electrolyte at pH 11, which further confirms the above peak assignments. The S $2p$ core-level peak without Ar^+ sputtering was curve fitted into two peaks centered at 168.47 and 169.8 eV, which were assigned to $Al_2(SO_4)_3 18H_2O$ [100] and $Al(OH)SO_4$, [101] respectively. The $Al_2(SO_4)_3 18H_2O$ spectrum at 168.47 eV disappeared after 5 min of Ar^+ sputtering. $Al(OH)SO_4$ existed on electrode surface after 20min of Ar^+ sputtering while the peak corresponds to sulfur completely disappeared after 25 min of etching. The analysis results on the core-level peaks confirmed that the sulfate anions were chemically incorporated into the passive film on AA1085. The thickness of the passive film can be estimated by the sputtering time at which the area ratio of the hydroxide peak to the aluminum matrix peak remains constant. Assuming that the etching rate on the passive film is the same as the calibrated etching rate of 1 nm/min on alumina, the thickness of the passive film formed on AA1085 electrode was approximately 25 nm.

The Al $2p$ core-level peaks measured on AA1085 electrode in 5 M $LiNO_3$ of pH 11 after 0, 5, 10, 15, 20 and 25 min of Ar^+ sputtering is shown in figure 4.10. The Al $2p$ spectra showed one peak after 0 and 5 min of sputtering centered at 74.83 and 74.76 eV. This peak has identical binding energies as the aforementioned $Al(OH)_3$ subpeak and it is assigned to aluminum hydroxide. [102] The Al 2p spectra after 10, 15, 20 and 25 min of Ar^+ sputtering depicted another subpeak centered at 75.95, 75.72 and 76.25 eV, respectively, which was assigned to aluminum oxy-hydroxide (AlOOH).[102] It is notable that with the increasing Ar^+ ion sputtering time, the ratio of the AlOOH sub peak area to the $Al(OH)_3$ sub peak area increases, which suggests that the primary phase that composes the aluminum passive film transforms from aluminum

hydroxide on top surface to aluminum oxy-hydroxide along the depth direction. This chemical status change of aluminum passive film can be explained by the precipitation mechanism of aluminate in alkaline solutions. At sufficient concentrations, aluminate precipitates as the most soluble phase first and subsequently precipitate as the next soluble phase. At neutral solutions or alkaline conditions, aluminate first precipitate as aluminum hydroxide and then the aluminum hydroxide transforms into less soluble boehmite.[88] The passive film formed on aluminum in $LiNO_3$ is too thick to sputter through using standard sputtering conditions in the apparatus. Therefore, the Al 2p spectra did not show the presence of aluminum matrix after 25 min of Ar^+ sputtering.

3.5 Influence of Li_2SO_4 and $LiNO_3$ on solution structure
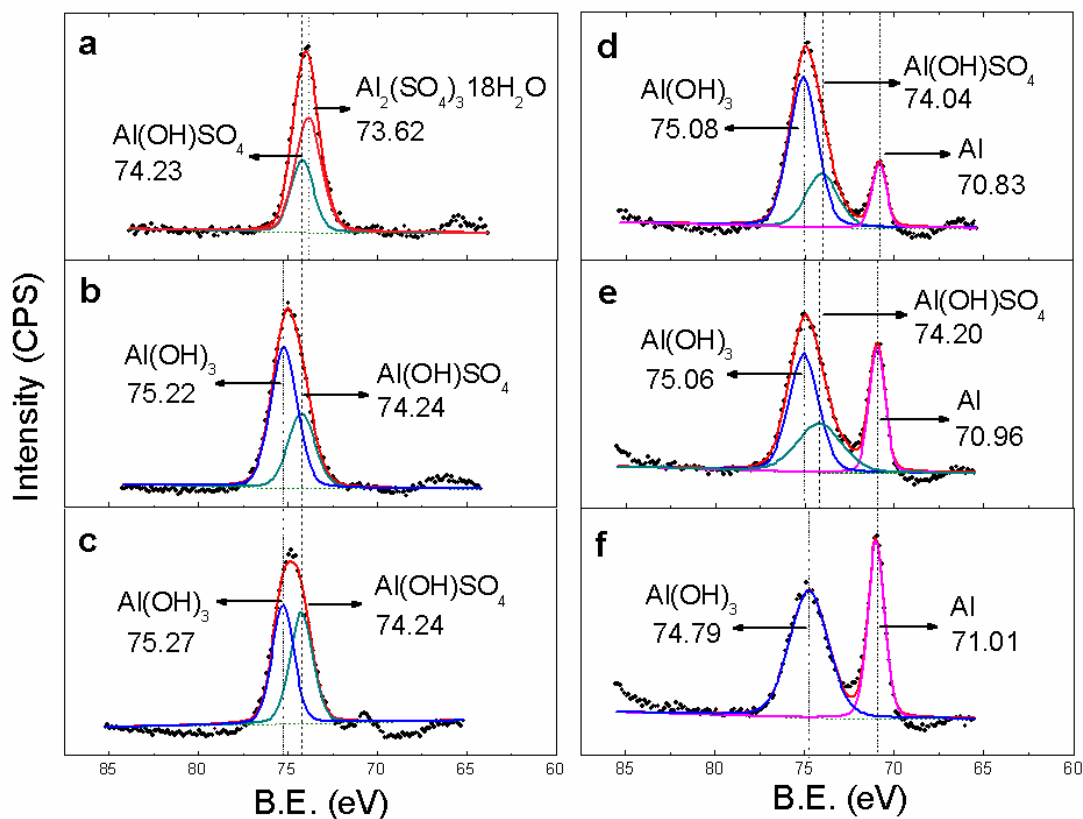
Figure 4.8 High resolution XPS scans of Al 2p core-level peaks of AA1085 electrode after 0, 5, 10, 15, 20 and 25 minutes of Ar+ etching.
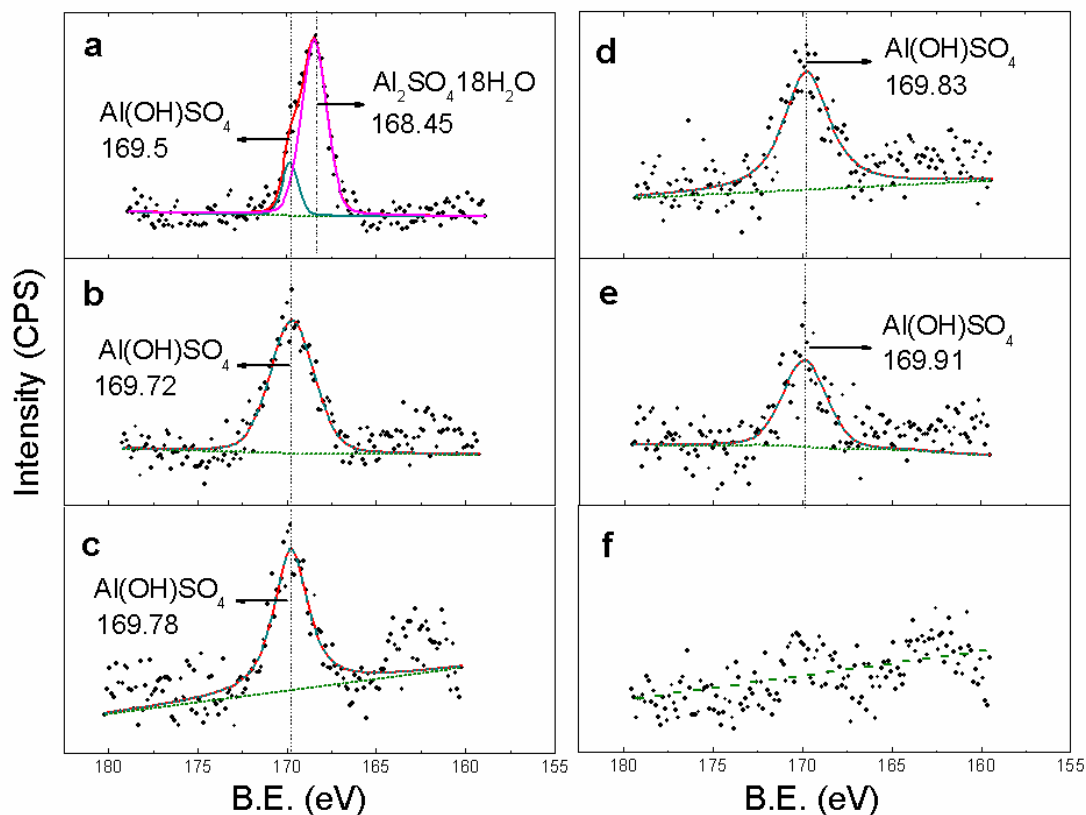
Figure 4.9 High resolution XPS scans of S 2p peaks for AA1085 electrode after chromoamperometry in 2 M Li$_2$SO$_4$ electrolyte at pH 11.

To gain insights into the dependency of electrolyte solution nature on concentration, the structure of the 2M Li$_2$SO$_4$ and 5M LiNO$_3$ electrolytes at pH 11 was investigated using Raman Spectroscopy. The Raman spectra of the aqueous electrolytes with different concentrations were compared to that of deionized water and LiOH solution at pH 11. The Raman spectrum of deionized water (figure 11) presents a broad band in the wavenumber range between 2800 and 3800 cm^{-1}. The Raman spectra of the other electrolytes exhibit the same –OH stretching feature and they are compared in figure 12. The broad band, which is associated to the –OH stretching of free water molecules,[104,105] was extracted and analyzed. As it is illustrated in Figure 11, the –OH stretching band of the tested solutions can be geometrically fit into three Gaussian-Lorentzian

contributions. The fitted signal positions, individual peak areas and the band areas of deionized water, LiOH solution and the aqueous electrolytes are listed in table 4.4. Increasing the lithium salt concentration weakened the amplitude of the –OH stretching band. The suppression of the –OH stretching feature indicates that the amount of free water molecules as free solvent decreases at higher electrolyte concentration levels.[105] A major portion of the water molecules exist as free solvent in electrolytes with low concentration of Li_2SO_4 or $LiNO_3$. With increasing salt concentration, the amount of solvating water molecules increases and the relative amount of free water molecule decreases. The structure change is obvious in 2 M Li_2SO_4 and 5 M $LiNO_3$ electrolytes. It should be noted that the spectra of all the electrolytes exhibited a weak band at 1640 cm^{-1}. The band centered at 1640 cm^{-1} is associated to deformation vibration of water molecules. The band is not presented here because its position, intensity and line shape are less sensitive to the factors that affect the hydrogen bonding than the broad band in 3400 cm^{-1} regions.

Table 4.4 The fitted band positions, individual peak areas and the band areas of deionized water, LiOH solution and the aqueous electrolytes.

Solution		Peak 1 Position (cm^{-1})	Peak 2 Position (cm^{-1})	Peak 3 Position (cm^{-1})	Peak 1 Area	Peak 2 Area	Peak 3 Area	Area Sum
DI Water		3237	3452	3613	1.34E+06	1.48E+06	9.79E+04	2.92E+06
LiOH pH 11		3235	3449	3613	1.14E+06	1.31E+06	9.33E+04	2.55E+06
Li_2SO_4 pH 11	0.1 M	3247	3457	3617	1.07E+06	9.61E+05	8.68E+04	2.11E+06
	0.5 M	3263	3460	3610	8.47E+05	6.22E+05	9.01E+04	1.56E+06
	2 M	3282	3458	3598	8.70E+05	5.37E+05	1.18E+05	1.52E+06
$LiNO_3$ pH 11	0.1 M	3254	3460	3614	1.34E+06	1.03E+06	1.52E+05	2.52E+06
	2 M	3282	3458	3598	8.70E+05	5.37E+05	1.18E+05	1.52E+06
	5 M	3262	3470	3603	4.59E+05	8.49E+05	4.66E+04	1.35E+06
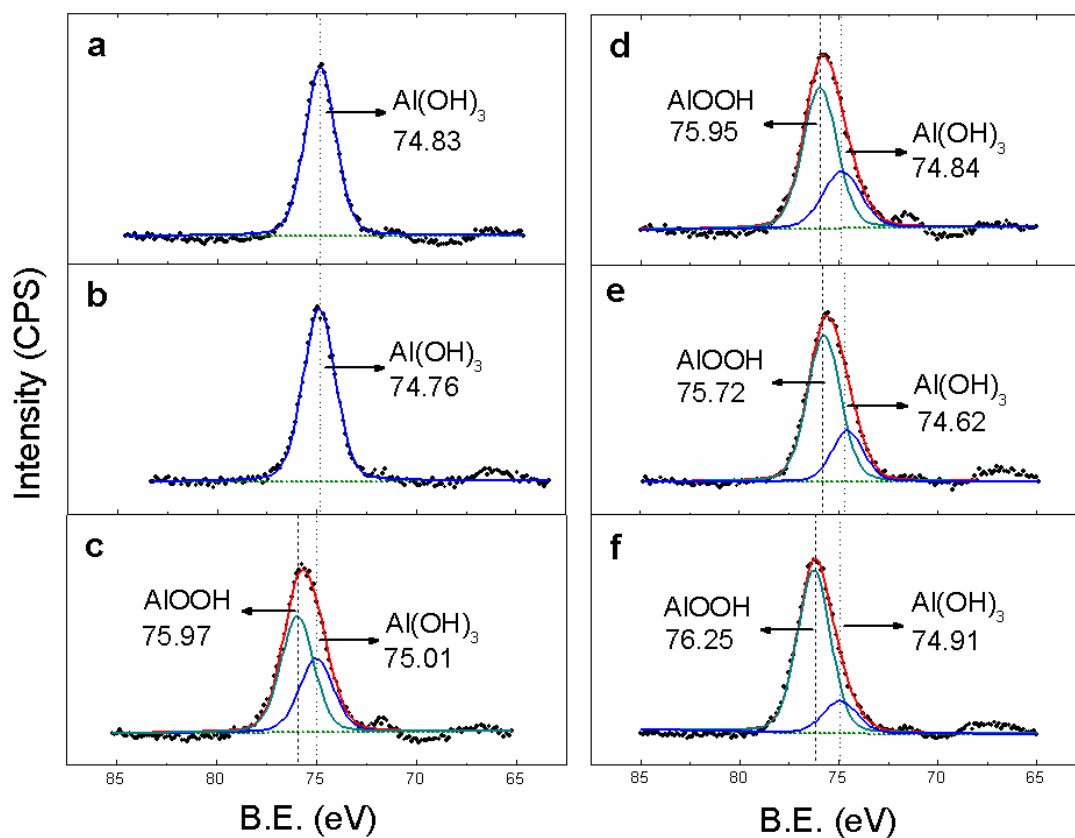
Figure 4.10 High resolution XPS scans of Al 2p core-level peaks measured on AA1085 electrode in 5 M LiNO$_3$ of pH 11 after 0, 5, 10, 15, 20 and 25 min of Ar+ sputtering.
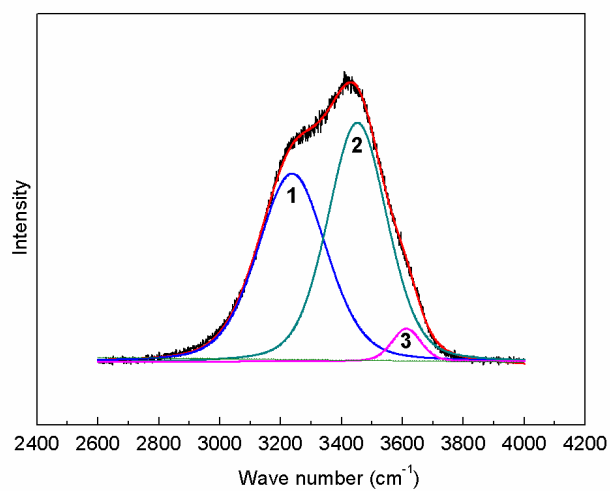
Figure 4.11 The Raman spectrum obtained on deionized water.
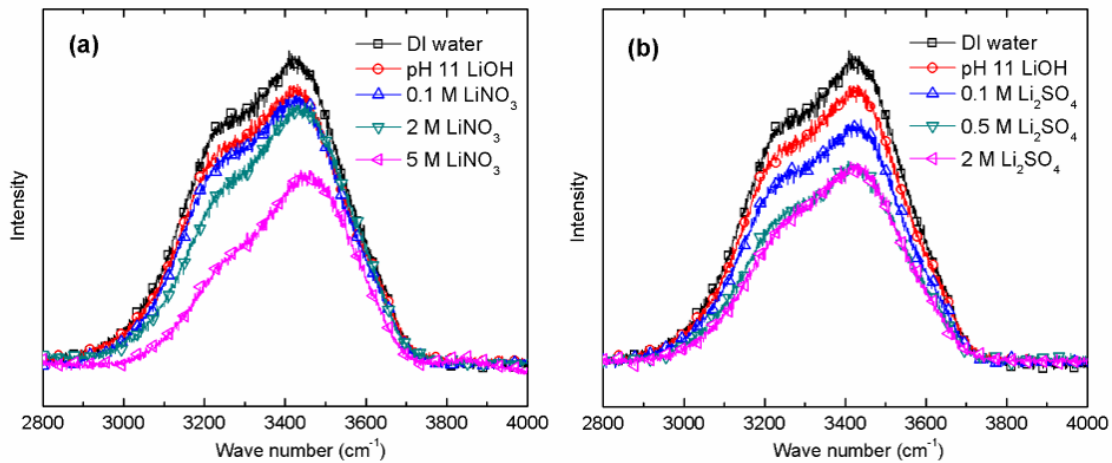
Figure 4.12 Comparison of Raman spectra obtained on (a) Li₂SO₄ electrolytes and (b) LiNO₃ electrolytes with that of de-ionized water and LiOH at pH 11 solution.

4.4 Discussion

4.4.1 The role of anion adsorption on corrosion kinetics

In alkaline solutions, the aluminum oxide passive film and aluminum matrix dissolve due to the attacking of hydroxyl ions by the following reactions,[81,106]

$$Al_2O_3(s) + 2OH^- + 3H_2O \rightarrow 2Al(OH)_4^- \tag{1}$$

$$2Al(s) + 2OH^- + 6H_2O(l) \rightleftarrows 2Al(OH)_4^- + 3H_2(g) \tag{2}$$

Pitting corrosion initiates preferably at surface defect sites and microstructural heterogeneities. For instance, the inevitable existence of Fe as impurity element in AA1085 results in the formation of Al₃Fe intermetallic particles that exhibit more noble electrochemical potentials than the aluminum matrix in aqueous solutions.[98] The protectiveness of aluminum oxide passive film is weak at the intermetallic sites. Due to the formation of galvanic cells between aluminum matrix and the intermetallic particles, accelerated dissolution of aluminum matrix adjacent to the intermetallic particles by reaction (2) is expected and subsequently stable pitting growth occurs.

Notably, at sufficient high concentration levels, the soluble $Al(OH)_4^-$ could precipitate as $Al(OH)_3$ as a result of crystallization by:[88]

$$Al(OH)_4^- \rightarrow Al(OH)_3(s) + OH^- \tag{3}$$
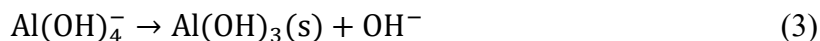
As evident by high-resolution XPS spectra, a thin layer of sulfate-incorporated passive film formed on AA1085 during anodic polarization in 2 M Li_2SO_4 electrolyte. The 25 nm passive film is primarily composed of $Al(OH)_3$ and $Al(OH)SO_4$, with $Al_2(SO_4)_3 18H_2O$ and $Al(OH)SO_4$ on the top surface. The aluminum sulfate hydrate $Al_2(SO_4)_3 18H_2O$ was often reported as possible solid aluminum corrosion product on aluminum surface resulting from exposure to environment containing sulfate.[107108] In alkaline solutions containing sulfate, competitive adsorption of chemical species such as sulfate, OH⁻ and H_2O dipoles occur on aluminum surface.[92] The adsorption process is often followed by chemical reaction between aluminum cations in passive film and adsorbed anion species, which lead to the formation of $Al(OH)_aX_b$ complexes.[109] The presence of basic aluminum sulfate can be explained by the formation energy of intermediates between aluminum and anions. Basic aluminum sulfate $Al(OH)SO_4$ has a lower free energy than $Al(OH)_4^-$ and $Al(OH)_3$. The formation energy is -342.7 kcal for $Al(OH)SO_4$, -271.9 kcal for $Al(OH)_3$ and -310.2 kcal for $Al(OH)_4^-$.[109] It was well accepted that in aqueous solutions Al^{3+} can also exist as hydrated form $Al(OH)^{2+}$ and $Al(OH)_2^+$ but these ions are also less stable compared to basic aluminum sulfate in terms of formation energy. Therefore, the formation of basic aluminum sulfate is favored in alkaline solutions containing sulfate by the following reaction pathways,

$$Al^{3+} + SO_4^{2-} = AlSO_4^+ \tag{4}$$

$$AlSO_4^+ + OH^- = Al(OH)SO_4 \tag{5}$$

$$AlOH^{2+} + SO_4^{2-} = Al(OH)SO_4 \qquad (6)$$
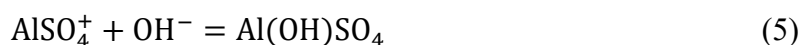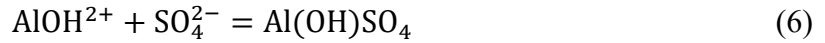
It was reported that basic aluminum sulfate have cation selectivity.[86] In the presence of such cation-selective diffusion layers, the ion transportation between aluminum and the test solution is mainly carried by cations. Then the dissolution of substrate aluminum transform from active to passive mode. Although pitting corrosion occurs in local area, the kinetics of pitting initiation depends on the transportation of species through the passive film. The sulfate-incorporated passive film repairs the defects in passive film and impede the migration of aggressive hydroxyl anions so a higher concentration of OH- in the double layer is required to initiate pitting, which is believed to contribute to the decreased pit nucleation rate in 2 M Li_2SO_4 electrolyte. This sulfate-incorporated passive layer is not capable inhibiting aluminum matrix over long periods under a high anodic potential. The breakdown of the basic aluminum sulfate film may be explained by its low thermodynamic stability in alkaline solutions.[83]

As it was shown in figure 4.12, a 2μm thickness corrosion product layer formed on AA1085 after 2000 seconds of anodic polarization at 0.85V in 5 M $LiNO_3$ electrolyte. The top 5 nm of the corrosion product layer is confirmed to be $Al(OH)_3$ while further Ar^+ etching showed the presence of both $Al(OH)_3$ and AlOOH. The peak intensity ratio of AlOOH to $Al(OH)_3$ increases with increasing sputtering depth, which indicates that the primary phase of the corrosion product layer change from $Al(OH)_3$ at top surface to AlOOH along the depth direction In alkaline solutions, nitrate anions could react with aluminum vigorously by the following reaction:[110]

$$8Al + 3NO_3^- + 5OH^- + 18H2O \rightarrow 8Al(OH)_4^- + 3NH_3 \qquad (7)$$
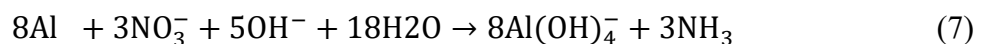
At sufficient concentration levels, the soluble aluminate ion $Al(OH)_4^-$ first precipitate as $Al(OH)_3$ on aluminum surface by reaction (3). In solutions at pH 7 or high pH conditions, however, the transformation of aluminum hydroxide $Al(OH)_3$ to boehmite $AlOOH$ is thermodynamically favored upon aging, especially under an applied anodic potential condition. [5] The phase transformation from $Al(OH)_3$ to $AlOOH$ explains the variation of the corrosion product layer chemical status with increasing depth. The soluble aluminate ions always precipitate as $Al(OH)_3$ first on top electrode surface. After anodic polarized over a period of time, the prior formed $Al(OH)_3$, which is beneath the freshly formed corrosion product on top surface, transforms to more stable phase, $AlOOH$. This hydroxide/oxy-hydroxide corrosion product film is not ion-selective thus free exchange of Al^{3+} and OH^- still occur between the aluminum matrix and the aqueous solution until the formed layer is sufficiently thick enough to impede the migration of ions. The thickness of passive film formed on aluminum determines the electric field gradient across the metal/solution interface. Considering the effect of the thick passive film on anodic potential field gradient across the passive film, application of 0.85V across the 25 nm film formed in 2 M Li_2SO_4 electrolyte produces 3.4×10^4 V/cm across the passive film. When the film thickness increased to 1 micron, the field gradient is expected to decrease by 40 times. The formation of the thick, compact and stable corrosion product film serves as a physical barrier to aggressive ions and protect the underlying aluminum matrix is well from pitting corrosion.

Increasing the anion concentration shifts the equilibrium of the reactions (4-7) to the right and in turn promotes the growth of passive films by the adsorption of anions. Similarly, an increase in applied anodic potential enhances the electric field across the passive film thus it consequently accelerates the anion adsorption. The enhanced anion adsorption at higher

electrolyte concentration and anodic potentials attributes to the change of aluminum corrosion kinetics, as it was depicted in chromoamperometry. The promoted growth of passive film serves slowing down the pitting growth rate in 2 M Li_2SO_4 electrolyte, and slightly enhances the inhibiting effect in 5 M $LiNO_3$ electrolyte.

4.4.2 The influence of solution structure on corrosion kinetics

As discussed above, the aluminum corrosion process is influenced by (i) extrinsic factors such as the pH, the applied potential that affects the dissolution reaction; and (ii) intrinsic factors such as the chemical status of the passive film, which may influence the transportation of aggressive ions. Another important intrinsic factor, which is often neglected in the discussion of corrosion kinetics, is the existence of ligands that could change the dissolution ability of the electrolytes. The electrolyte concentration level affects both the solution structure and corrosion kinetics of AA1085 in Li_2SO_4 and $LiNO_3$ electrolytes, which suggests that there is a possible correlation between the amount of free solvent water molecules and aluminum corrosion in ARLB electrolytes. The basics of this correlation may contribute to the suppression of aluminum pitting rate at higher concentrations of Li_2SO_4 electrolyte and the slightly enhanced inhibiting effects of concentrated $LiNO_3$ electrolytes by the following proposed mechanism.

Al^{3+} ion is not a stable form in aqueous solutions thus it is usually stabilized by forming complexes with ligands.[88] In alkaline solutions, the dissolution of aluminum occurs primarily by reaction (2) and result the formation of $Al(OH)_4^-$. With the addition of sulfate and nitrate anions, other soluble complexes such as $Al(OH)^{2+}$, $Al(OH)_2^+$ and $AlSO_4^+$ may form at the electrode/solution interface. Considering $Al(OH)_4^-$ alone as the dissolved species for simplicity, the dissolution rate of aluminum depends on the concentration of soluble complexes $Al(OH)_4^-$

109

and OH^- at the solution/aluminum interface, according to thermodynamic basics. The pitting corrosion during growth period is usually diffusion controlled.[88,111] In a dilute electrolyte, a large amount of water molecules in the electrolyte are free solvent. The soluble aluminum complexes produced by the aluminum dissolution reaction can be easily solvated by the free water molecules and transported from the electrode/solution interface to the bulk solution through diffusion, which keep the interfacial concentration of aluminum complexes low. The rapid removal of the interfacial soluble aluminum complexes contributes to the continuous proceeding of the aluminum dissolution reaction. In highly concentrated electrolytes, however, since the amount of free solvent molecules available for solvating soluble aluminum complexes is much less, which is confirmed by Raman spectroscopy, the dissolution ability of the solution is remarkably lower than that of dilute electrolyte. In this scenario, the dissolution of aluminum soluble complexes is not as quick as that in dilute electrolyte and a sluggish transportation of the aluminum complexes into bulk electrolyte through diffusion is expected. Consequently, the concentration of the aluminum soluble complexes builds up at the electrode/solution interface, which shifts the equilibrium of the dissolution reaction to the left and mitigates the dissolution of aluminum. As is evident from chromoamperometry, increasing the concentration of Li_2SO_4 electrolyte reduces the pitting growth rate. Meanwhile, concentrated $LiNO_3$ slightly contributes to the inhibition on aluminum. The suppression of aluminum corrosion in both cases was contributed by the decreased mass transport kinetics of soluble aluminum complexes from the electrode/solution interface into the bulk electrolyte.

4.5 Conclusion

1. The corrosion kinetics of AA1085 in slightly alkaline ARLB Li_2SO_4 and $LiNO_3$

electrolytes was investigated using chronoamperometry within the stability window. AA1085 was prone to pitting corrosion in Li_2SO_4 electrolytes at the anodic potential of 0.85 V. In $LiNO_3$ electrolytes, AA1085 was protected from pitting corrosion due to repassivation phenomenon. The kinetics of pitting corrosion and repassivation process on AA1085 is influenced by the electrolyte concentration level and the applied anodic potentials.

2. The passive film formed on AA1085 in 2 M Li_2SO_4 electrolyte before the occurrence of pitting corrosion comprises cation-selective $Al(OH)SO_4$, which contributes to the slowing down of pitting corrosion kinetics. In 5 M $LiNO_3$ electrolyte, a corrosion product layer, which is composed of $Al(OH)_3$ and $AlOOH$, formed on AA1085. Although this corrosion product layer does not have ion-selectivity, it serves as a barrier layer which impedes the ingression of aggressive anions and protect aluminum from rapid pitting corrosion.

3. Raman spectroscopy showed that the amount of free water molecular as solvents for dissolved aluminum complexes reduces with increasing electrolyte concentration. The reduced dissolubility of the electrolyte is believed to affect the transportation of dissolved aluminum species from the electrode/solution interface to bulk solution, which consequently impede the dissolution of aluminum.

CHAPTER 5 Effects of Sulfate and Nitrate on the Electrochemical Behavior of Al-Fe and Al-Fe-Si Intermetallic in Alkaline Solutions

5.1 Introduction

Commercial purity grade aluminum AA1xxx, is widely used as conductive substrate in energy storage systems such as lithium-ion battery, super capacitors and sacrificial anodes due to its advantages in high conductivity, lightweight, low cost and considerable mechanical strength. The inevitable presence of impurity elements results in the formation of intermetallic particles in aluminum alloys. The phase diagram for Al-Fe indicates the maximum solubility of Fe in Al is approximately 0.04 wt.% at 655 °C and it decreases to less than 0.001 wt.% below 430 °C. AA1100 contains up to 0.95 wt% of Si and Fe, which is significantly above the solid solubility of Fe in Al at room temperature.[65] The most commonly found intermetallic compound in AA1100 is Al-Fe and Al-Fe-Si. Under equilibrium conditions, the excessive iron exist as phase Al_3Fe, however iron usually exist as a number of non-equilibrium intermetallic phases in AA1100.[13] In some aluminum alloys, intermetallic are intentionally created by addition of alloy elements and heat treatments to achieve desirable properties, such as mechanical strength, resistance to high temperature oxidation and creep, shape memory effects and hydrogen storage capability. However, theses intermetallic is usually considered detrimental on corrosion resistance. The structure heterogeneity caused by the constitutional intermetallic may increase the risks of localized corrosion on aluminum because the intermetallic often exhibits electrochemical properties that differ from the aluminum matrix.[49]

The increase in hydrogen evolution due to the galvanic corrosion is detrimental to energy storage systems because it significantly reduces the faradic efficiency. The development of

protection methodologies and approaches that could suppress such catalytic effects, such as design of alloy composition and addition of inhibitors, are rendered necessary due to the vast applications of aluminum alloys in industries. The role of the elemental composition of intermetallic compounds on the galvanic corrosion of aluminum alloys has been extensively studied.[13,14,15, 112,113] Many of the available work consider the corrosion potential differences between the intermetallic and the aluminum matrix in the environment of interest as the driving force of galvanic corrosion. The formation of noble intermetallic act as cathodic sites and promote galvanic corrosion. Hydrogen evolution reaction occurs preferably at intermetallic sites because of their low over potential for hydrogen evolution reaction. As the primary intermetallic in AA1100 alloy, Al_3Fe can act as cathodic sites for hydrogen evolution, resulting in the higher self-corrosion rates of AA1100.[114] Using micro-capillary electrode method, Birbilis et. al revealed that the corrosion potential difference may not fully reflect the electrochemical activity of intermetallic compounds.[12] The change of elemental composition and structure during the polarization behavior of the intermetallic plays more important role on the long-term corrosion behavior of aluminum alloys. As a result of the predominant cathodic reaction on intermetallic particle, local variation of pH, anodic dissolution of adjacent aluminum matrix occurs.

K.C. Emregul investigated the electrochemical behavior of intermetallic containing Fe in neutral chloride solutions.[115] Enrichment of iron occurs on the intermetallic due to the selective aluminum dissolution. In the potential range between -1.175V and -0.72V (SCE), the surface is oxidized into $Fe(OH)_2$ and Fe_3O_4. A trans-passive region was associated to the selective dissolution of aluminum and oxidation of iron into non-protective oxide, possibly FeOOH. At higher potentials, the surface is passivated by Fe_2O_3. The multi-component phase in intermetallic

compounds accelerates selective dissolution. Reduction reactions such as hydrogen evolution $2H^+ + 2e^- \rightarrow H_2$ and oxygen reduction: $O_2 + 2H_2O + 4e^- \rightarrow 4OH^-$ produce excess of hydroxyl ions around the intermetallic. Nisancioglu studied the electrochemical behavior of Al_3Fe, AlFeSi in 0.1 N NaOH alkaline solution.[14] Al_3Fe undergo a preferable dissolution of aluminum and the intermetallic surface became rich in Fe, which affects both the cathodic behavior of intermetallic and the anodic behavior of aluminum matrix. It was claimed that the addition of Si in intermetallic reduces the effect of Fe, slows down the preferable dissolution of aluminum, possibly because Si atoms can incorporate into Al_2O_3 passive film, which reduce defects in the oxide layer and the dissolution rate of passive film.

It was revealed in above chapters that the addition of sulfate and nitrate anions affects the chemical status of passive films and the dissolubility of aqueous electrolyte, which in turn influence the corrosion kinetics and mechanisms of aluminum in alkaline solutions. As the intermetallic particles play an important role on the initiation and growth of localized corrosion, it is not clear how the addition of sulfate and nitrate anions influence the electrochemical behavior of Al from Al-Fe in alkaline solutions. By choosing bulk intermetallic alloys that are representative of the constituents in AA1100, Al_xFe_y and $Al_xFe_ySi_z$ are used as matrix analog. The electrochemical characteristics of the synthesized intermetallic can be catalogued and used to rationalize the corrosion behavior of the bulk alloy. The most accessible methods to prepare the intermetallic bulk alloys is direct casting. It is well known that many possible intermediate phases may form during the solidification. Metastable orthorhombic Al_6Fe and monoclinic $Al_{13}Fe_{14}$ may form as secondary phase in Al_3Fe. The ternary phase diagram of Al-Fe-Si system indicates that a variety of $Al_xFe_ySi_z$, Al_xFe_y and Fe_xSi_y polyphase structure may form during

solidification. It is impossible to obtain a single homogeneous phase structure with the same ratio of Al/Fe in synthesized Al_xFe_y and $Al_xFe_ySi_z$. As the electrochemical property of intermetallic compounds is primarily determined by the individual electrochemical behaviors of the elemental components, Al-Fe and Al-Fe-Si alloys with the same ratio of Al/Fe were synthesized to compare the role of element Fe and Si in the electrochemical behavior of the intermetallic. Since pH of solution surrounding the intermetallic often becomes alkaline due to oxygen reduction and hydrogen evolutions, the electrochemical tests are carried out in an alkaline solution. The objective of this work is to study the influence of the noble components and the anion species in environment on the electrochemical behavior of Al-Fe and Al-Fe-Si intermetallic compounds in Al1100. Both the anodic and the cathodic behavior of synthesized intermetallic were examined. Their anodic behavior is emphasized in discussion because it affects the efficiency of the intermetallic as cathodes. The outcomes of this work can be applied in predicting the corrosion behavior of aluminum alloys, design of corrosion-resistant alloys and aluminum alloy corrosion inhibitors.

5.2 Experimental

5.2.1 Synthesis of Al-Fe and Al-Fe-Si alloy

AA1100 sheets of 3mm in thickness were machined into square pieces with the size of 25mm×25mm. The composition of the AA1100 sheet is shown in table 5.1. Intermetallic bulk alloys were synthesized by mixing the target proportions of constituent metals and alloys. Synthesizing such alloys require knowledge of equilibrium conditions under which the intermetallic of interest could form. The equilibrium Al-Fe and Al-Fe-Si phase diagram that predicts the final phase, which are readily available in literature,[116] were used for the synthesis.

Al-Fe alloy was made by direct casting a mixture of 99.99% Al and 99.9 Fe powder in alumina crucibles. Al-Fe-Si alloy was casted using a mixture of 99.99% Al, 99.9 Fe powder and AlSi alloy. The mixture was heated from room temperature to 1300 °C for 2 hours in a Lindberg tube furnace with controlled atmosphere. The heating rate was 10 °C per minute. The protective inert gas was a mixture of H_2 gas and argon gas with the ratio of 1 to 10 and the gas flow rate was 200ml/min. After homogenization, the ingots were cooled down in the furnace to room temperature. For the simplicity of comparison, the atomic ratio of Al to Fe was artificially picked as 2:1 so a homogeneous Al_2Fe alloy is expected. The atomic ratio of Al:Fe:Si in Al-Fe-Si alloy was picked as 6:3:2 so that three phases present in the final structure. The final structure of the Al-Fe-Si is expected to have the minimal amount of phases and its two primary phase has the same Al:Fe ratio of 2:1 as Al_2Fe.[116] It should be noted that the synthesis of a completely homogeneous bulk intermetallic ingot is not possible because most intermetallic does not develop into only one phase. Although the final structure might be heterogeneous and three Al-Fe-Si phase are expected, it is believed that the obtained alloy could serve well in revealing the effect of element Si on the electrochemical property of intermetallic compounds.

Table 5.1 Chemical composition of AA1100 sheet.

Grade	Composition Specification (max wt.%)					
	Si+Fe	Cu	Zn	Mn	Others	Al
1085						
	0.95	0.05-0.2	0.1	0.05	0.05	Bal.

The casted alloys were grinded with silicon carbide paper to 1200 grit, polished with 1 μm alumina suspensions, cleaned with ethanol and gently dried using a stream of nitrogen.

Subsequent identification of intermetallic composition was done by backscatter electron microscopy, electron-dispersive spectroscopy (EDS) using Hitachi S-4800 field emission scanning microscope and X-ray diffraction (XRD) using Bruker D8 DISCOVER X-ray diffractometer. XRD was conducted using Cu K_α radiation at a scan rate of 0.5°/min.

5.2.2 Surface treatment of AA1100

Some AA1100 electrodes were surface-treated to create intermetallic compound-free surface. The as polished AA1100 electrodes ere cleaned and pickled 10% NaOH solution at 353 K for 60 seconds followed by water rinsing. The specimen was then passivated in a 30% HNO_3 solution at room temperature for 60 seconds, rinsed with distilled water and gently dried using a stream of nitrogen gas. The electrodes were galvanostatically kept at a current density of -200 mA/cm^2 in a deaerated, 17% HNO_3 solution for 1000 seconds. The electrode was cleaned, dried and subsequently dipped into a 4% $Na_2CrO_44H_2O$ in 10% H_3PO_4 aqueous solution at 353 K for 4 min to remove the adhered corrosion products.

5.2.3 Electrolyte preparation

The electrolytes are prepared by dissolving specific weight of LiOH (anhydrous, 98%, Alfa Aesar) in de-ionized water to achieve concentration of 0.001 M and 1 M, followed by addition of targeted concentration of 0.1M and 2M of Li_2SO_4 (anhydrous, 99.7%, Alfa Aesar) or 0.1 M, 2 M and 2 M of $LiNO_3$ (anhydrous, 99.98%, Alfa Aesar) equivalent. The solution was magnetic stirred until the salts were fully dissolved. The pH value was monitored using a Mettler FE20 Ag/AgCl pH electrode.

5.2.4 Electrochemical testing

Electrochemical measurements were carried out using a conventional three-electrode system in a 250 ml BioLogic flat cell with 1 cm^2 electrode area. Ag/AgCl with saturated KCl (0.197 V vs SHE) solution was used as the reference electrode. The reference electrode was separated from the body of the cell using a luggin capillary to minimize the IR drop. A platinum mesh was used as the counter electrode. The test solutions were deaerated by purging high purity nitrogen gas into the solution for 1 hour before the electrolyte come into contact with the sample. The electrode was first stabilized at open circuit potential for 30 min. Potentiodynamic polarization was carried out in the potential range from -0.5 V vs open circuit potential (OCP) to 2 V above the OCP, followed by a reverse scan with a scanning rate of 0.5 mV/s. EIS measurements were taken in the 0.01-10,000 Hz frequency range with perturbation amplitude of 10mV root mean square (RMS) and sampling rate of 10 points per decade at open circuit potentials. After each measurement, the flat cell and the platinum mesh counter electrode were rinsed by distilled water, isopropyl alcohol and air-dried. At least three measurements were performed and the representative results are presented.

5.2.5 Surface characterization

The surface morphology of AA1100, surface treated AA1100, synthesized alloys and electrodes before and after potentiodynamic polarization was examined by a Hitachi S-4800 field emission scanning microscope in secondary electron mode or backscattered electron mode. The surface elemental composition of the alloys before and after tests was analyzed by energy dispersive spectrum (EDS). Raman spectroscope microscopy was performed using a Renishaw Inc. 1000B. The Raman spectrum was excited by a helium-neon laser producing highly polarized

light at 633 nm and collected in the range between 200 and 4000 cm^{-1}. The spectra were calibrated using the 519.5 cm^{-1} of a piece of silicon wafer. Raman spectrum was acquired with a 10 s integration time and the power at the sample was 10 mW.

5.3 Results and Discussion

5.3.1 Intermetallic identification

Satisfactory identification of synthesized intermetallic requires both chemical and structural analysis. The surface morphology of synthesized Al-Fe and Al-Fe-Si intermetallic alloy was characterized via a scanning electron microscopy which allows backscattered electron (BSE) imaging. EDS was used to examine the details of the composition of the phase probed. Further identification on the structure of the synthesized alloy was done by X-ray diffraction on the synthesized alloys. Figure 1 shows the BSE image of and the EDS spectra of the synthesized Al_xFe_y and $Al_xFe_ySi_z$ alloy. In figure 5.1a, the Al_xFe_y alloy showed only one phase. Figure 5.1b shows that the synthesized $Al_xFe_ySi_z$ alloy, however, constituted a polyphase system with three phases identifiable in BSE. EDS analysis on Al_xFe_y alloy shows the elemental ratio of Al to Fe is exactly 2:1, which indicates the presence of homogeneous Al_2Fe phase. Two phase in the synthesized $Al_xFe_ySi_z$ alloy have Al/Fe atomic ratio very close to 2:1, although the content of Si is slightly different. The composition of the two phase are $Al_{55}Fe_{28}Si_{10}$ and $Al_{53}Fe_{27}Si_{17}$. The third phase, which gave the highest contrast in backscatter electron imaging, is rich in element Fe and the composition is $Al_{30}Fe_{41}Si_{29}$. Figure 5.2 shows the secondary electron microcopy on AA1100 and surface treated AA1100. AA1100 revealed considerable amount of intermetallic particles on surface. After the surface treatment, AA1100 with intermetallic-free surface is

obtained. The mechanisms for the removal of intermetallic can be explained by the preferable dissolution and physical activation of intermetallic particles during hydrogen evolution.[117]
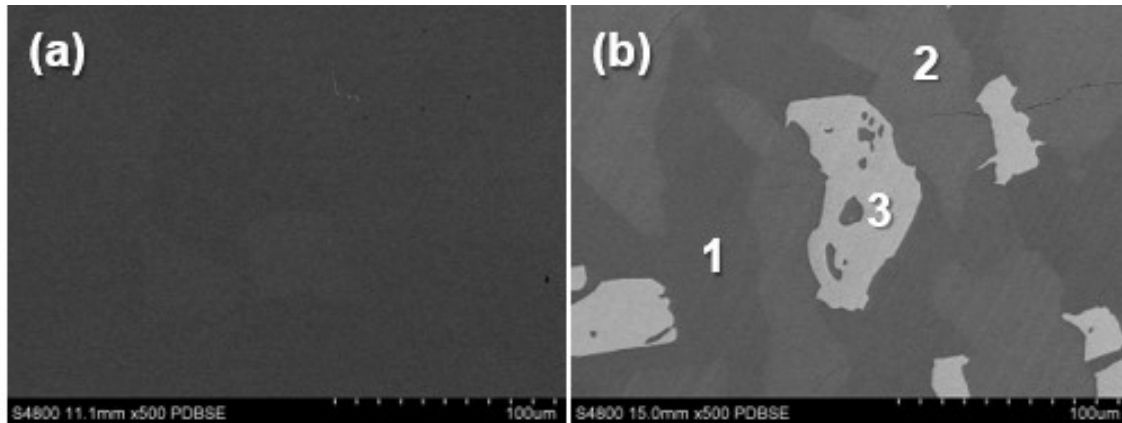
Figure 5.1 BSE image of and the EDS spectra of the synthesized (a) Al_xFe_y and (b) $Al_xFe_ySi_z$.
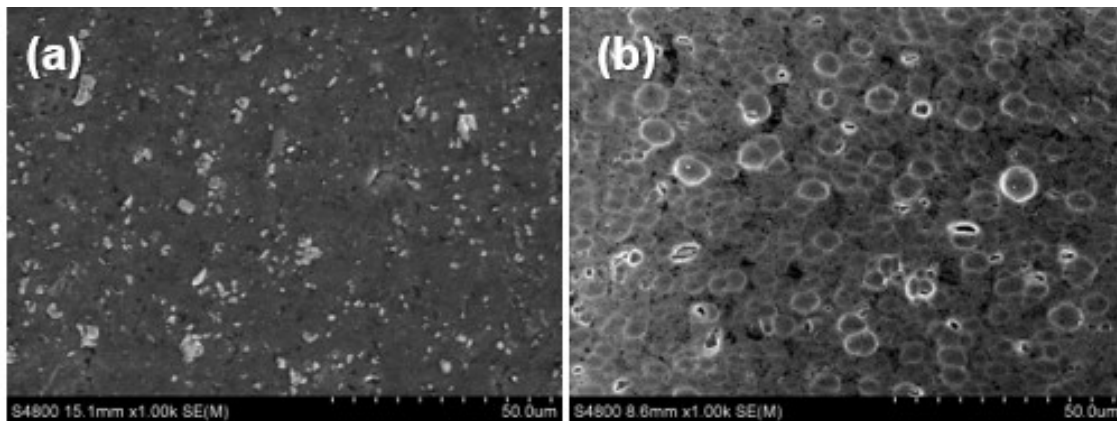
Figure 5.2 Secondary electron microcopy on the surface morphology of (a) AA1100 and (b) surface treated AA1100.

Figure 5.3 presents the XRD patterns of AA1100, surface treated AA1100, synthesized Al-Fe and Al-Fe-Si intermetallic alloys. The XRD spectra of AA1100 and surface-treated AA1100 depict α-Al phase. Several non-indexed reflections, which are too weak to be identified, are believed to belong to the intermetallic particles. As expected, the primary phase in synthesized Al-Fe alloy is Al_2Fe phase. The XRD spectrum of the synthesized Al-Fe-Si alloy

showed indexed reflections of $Al_4Fe_{1.7}Si$, Al_2FeSi and Al_8Fe_2Si mixture phase. The presence of $Al_4Fe_{1.7}Si$, Al_2FeSi spectra agrees with the elemental composition results of $Al_{55}Fe_{28}Si_{10}$ and $Al_{53}Fe_{27}Si_{17}$ phase obtained by EDS. The third indexed phase, whose composition is Al_8Fe_2Si, is believed to have same structure with $Al_{30}Fe_{41}Si_{29}$ phase. The EDS and XRD results is not entirely in consistent with the prediction of equilibrium phases by Marker et al.[116] The predicted equilibrium phase in the synthesized Al-Fe-Si alloy were τ_1 ($Al_{21.0-41.5}Fe_{37.5-38.5}Si_{41.5-21.0}$), τ_3 ($Al_{52.0-54.5}Fe_{25.0-26.5}Si_{23.0-19.0}$) and τ_{11} ($Al_{62.5-65.0}Fe_{26.0}Si_{11.5-9.0}$) phases. The $Al_{30}Fe_{41}Si_{29}$ and the $Al_{53}Fe_{27}Si_{17}$ are identified as τ_1 and τ_3 phase. However, as the two major phase both have the same Al:Fe ratio of 2:1, the synthesized Al-Fe-Si serves the purpose of investigating the role of Si on the electrochemical property of $Al_2FeSi_{0.67}$.
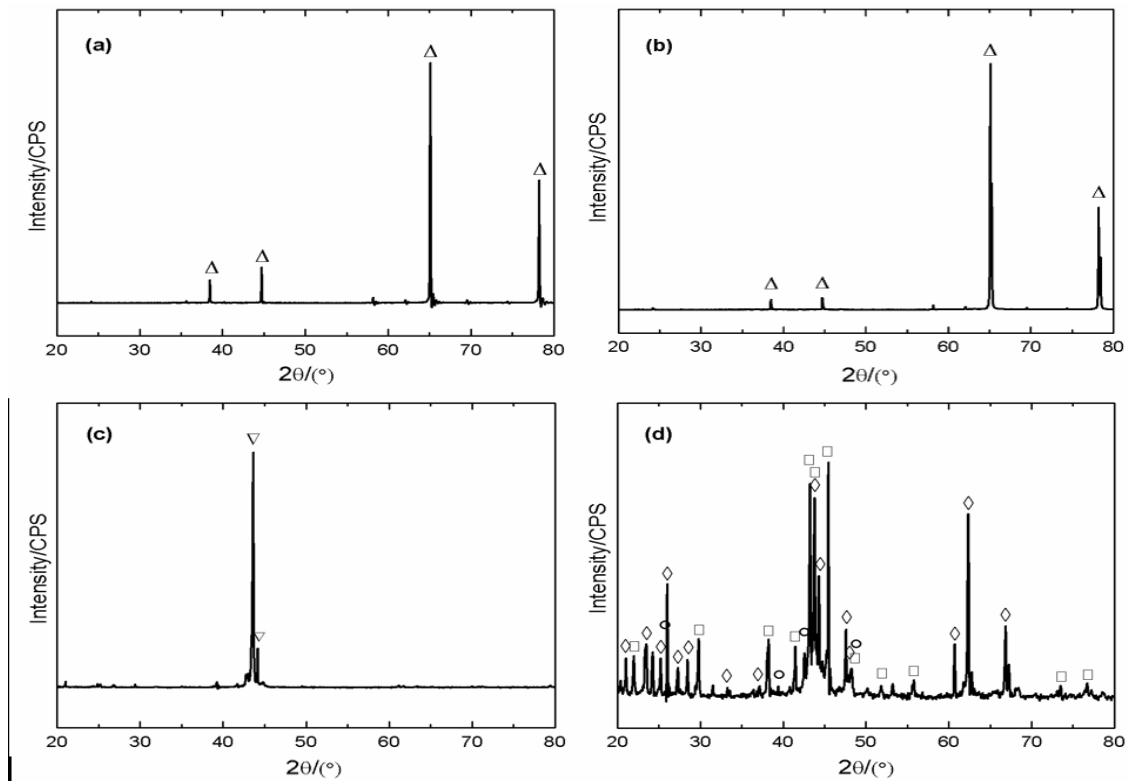
Figure 5.3 XRD patterns of (a) AA1100 and (b) surface treated AA1100 with Δ-Al (c) synthesized Al-Fe with ∇-Al_2Fe and (d) Al-Fe-Si with $\square$-Al_2FeSi, $\lozenge$-$Al_4Fe_{1.7}Si$ and $\bigcirc$-Al_8Fe_2Si

5.3.2 Potentiodynamic polarization

The characteristic potentials on potentiodynamic polarization curves of the specimens, including the corrosion potential E_{corr}, and the potential E_b at which break down of passivity occurs are obtained and the average values are presented in table 5.2. In general, Al_2Fe has the noblest corrosion potential in all tested solutions. $Al_2FeSi_{0.67}$ is less noble than Al_2Fe in all tested solutions but its corrosion potential is more positive than Al1100 and surface treated Al1100. The difference in corrosion potential is due to the presence of noble element component, Fe and Si, in the intermetallic alloys. Therefore, the intermetallic particles are expected to act as cathodic sites on aluminum surface.

Table 5.2 The characteristic potentials obtained from potentiodynamic polarization curves.

Salt	LiOH (M)	AA1100		Surface treated AA1100		Al_2Fe		$Al_2FeSi_{0.67}$	
		E_{corr}(V)	E_b (V)	E_{corr}(V)	E_b (V)	E_{corr}(V)	E_b (V)	E_{corr}(V)	E_b (V)
-	1	-1.322	0.71	-1.344	0.75	-1.16	0.604	-1.188	0.623
0.1 M $LiNO_3$	0.001	-0.956	1.82	-1.162	1.34	-0.815	0.794	-0.941	0.023
2 M $LiNO_3$	0.001	-0.79	1.642	-0.966	1.64	-0.746	1.338	-0.835	-0.114
0.1 M Li_2SO_4	0.001	-1.254	1.532	-1.341	1.559	-1.045	1.495	-1.093	-0.026
2 M Li_2SO_4	0.001	-1.183	1.468	-1.288	-	-0.971	1.424	-1.048	0.115
0.1 M $LiNO_3$	1	-1.162	0.716	-1.188	0.717	-0.986	0.607	-1.006	0.628
2 M $LiNO_3$	1	-0.949	0.704	-0.965	0.694	-0.916	0.628	-0.92	0.665
0.1 M Li_2SO_4	1	-1.341	0.7064	-1.344	0.89	-1.156	0.62	-1.194	0.619
2 M Li_2SO_4	1	-1.392	0.747	-1.35	0.731	-1.12	0.647	-1.146	0.636

The potentiodynamic polarization curves of electrodes tested in 0.001M LiOH, with the addition of Li_2SO_4 are presented in figure 5.4. Increasing the concentration of Li_2SO_4 from 0.1 M to 2 M slightly shifts the E_{corr} to more noble values. The anodic current on AA1100 and surface treated AA1100 are very close and both electrodes showed passivity above E_{corr}. In 0.001 M LiOH, 2 M Li_2SO_4 electrolyte, the surface-treated AA1100 did not show the breakdown of passivity in the potential scanning range, which is possibly due to the low heterogeneity on the surface-treated electrode surface. Based on prior works, the chemical adsorption of sulfate is expected to occur on the intermetallic-free surface, which results in the formation of sulfate-incorporated, protective passive film. Increasing the concentration of Li_2SO_4 reduced the anodic dissolution rate of Al_2Fe, by one order of magnitude. On intermetallic alloys, the high anodic dissolution rate above E_{corr} indicates that the selective dissolution of Al occurred, regardless of the concentration of sulfate. The enrichment of Fe in intermetallic increases the electrochemical potential difference between the intermetallic and the aluminum matrix, and in turn increases the susceptibility to pitting corrosion. The electrochemical behavior of Al-Fe-Si alloy is merely affected by the change of Li_2SO_4 concentrations. Notably the E_{corr} of AA1100 and surface treated AA1100 are both less noble than Al_2Fe and Al-Fe-Si alloy, but their anodic dissolution rate is much lower with wide range of passivity, which confirms that the corrosion potentials do not necessarily predict the corrosion kinetics of alloys.

Figure 5.4 The potentiodynamic polarization curves of specimens tested in 0.001M LiOH, with the addition of (a) 0.1 M and (b) 2 M Li_2SO_4.

In 0.001 M LiOH, increasing the concentration of $LiNO_3$ from 0.1 M to 2 M shifts the E_{corr} of all electrodes to more noble potentials and reduces the electrochemical potential difference between intermetallic alloys and Al1100. As it is shown in figure 5.5, both AA1100 and surface treated AA1100 showed a wide range of passivity and break down characteristics on passive film. Anodic polarization on Al_2Fe and $Al_2FeSi_{0.67}$ intermetallic reveals that the selective dissolution of Al above corrosion potential was suppressed on intermetallic alloys. The surface treated AA1100 showed the least noble corrosion potential and relatively high dissolution rates in the anodic range above E_{corr} in 2 M $LiNO_3$ electrolyte. The reactivity is possibly due to the chemical adsorption of nitrate anions on aluminum surface.

Figure 5.5 The potentiodynamic polarization curves of specimens tested in 0.001M LiOH, with the addition of (a) 0.1 M and (b) 2 M LiNO$_3$.

The potentiodynamic polarization curves of the specimens in 1 M LiOH electrolyte is shown in figure 5.6. All electrodes showed large current density due to the high dissolution rates in concentrated hydroxide solution. AA1100, surface treated AA1100 and Al$_2$Fe all showed rapid aluminum dissolution above the E$_{corr}$. Al$_2$FeSi$_{0.7}$ alloy, however, presented clear passivity in the same potential range and the anodic current on Al$_2$FeSi$_{0.7}$ is one order of magnitude lower than the other electrodes, indicating that the preferable dissolution of aluminum is suppressed. Since the anodic current is in mA scale, the dissolution rate is still considered high. The active dissolution process is followed by a reduced current density on all electrodes. On AA1100 and surface treated AA1100, the reduced current density is probably due to the formation of a thick aluminum hydroxide layer on surface. The passivity on intermetallic alloys is caused by the formation of oxidized iron species on electrode surface. Al$_2$Fe and Al-Si-Fe showed break down of passivity at 0.604 V and 0.623 V, presenting a narrow range of passivity. After the break

down of passivity, the active aluminum dissolution resumes and the dissolution rate is significantly higher than that of AA1100 electrodes.
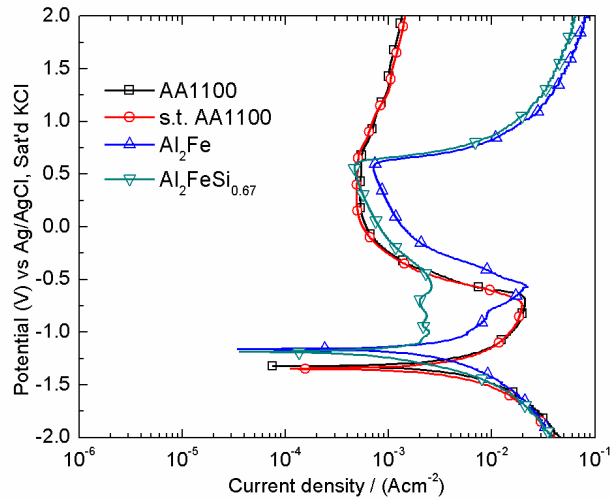
Figure 5.6 The potentiodynamic polarization curves of the specimens in 1 M LiOH electrolyte.

The E_{corr} all electrodes merely change after the addition of 0.1 M and 2 M Li_2SO_4 in 1 M LiOH. Fgure 5.7 shows the anodic polarization curves of electrodes in 1 M LiOH with addition of 0.1 M Li_2SO_4 and 2 M Li_2SO_4. It was found that the anodic dissolution rate above E_{coor} of all electrodes was slightly reduced after the addition of sulfate anions but the effect of sulfate is minor. Increasing the concentration of sulfate anions from 0.1 M to 2 M does not have an obvious impact on the anodic current response. The anodic current on AlSiFe alloy was significantly lower than other electrodes, which is again an indication that the existence of silicon may mitigated the preferable dissolution of Al.
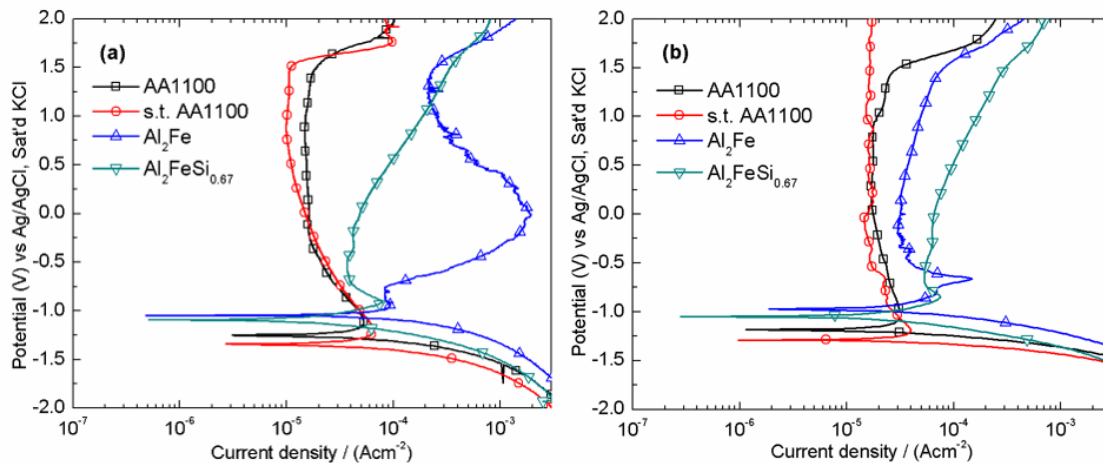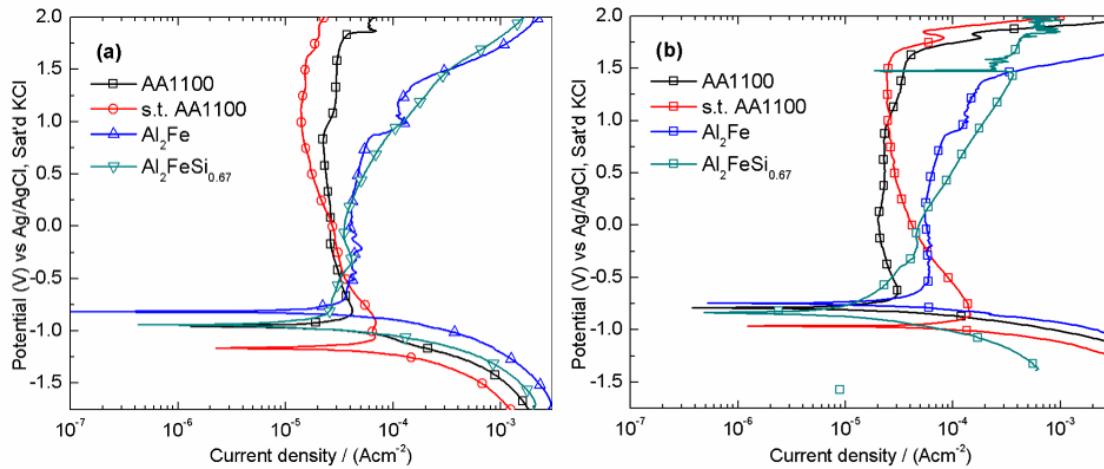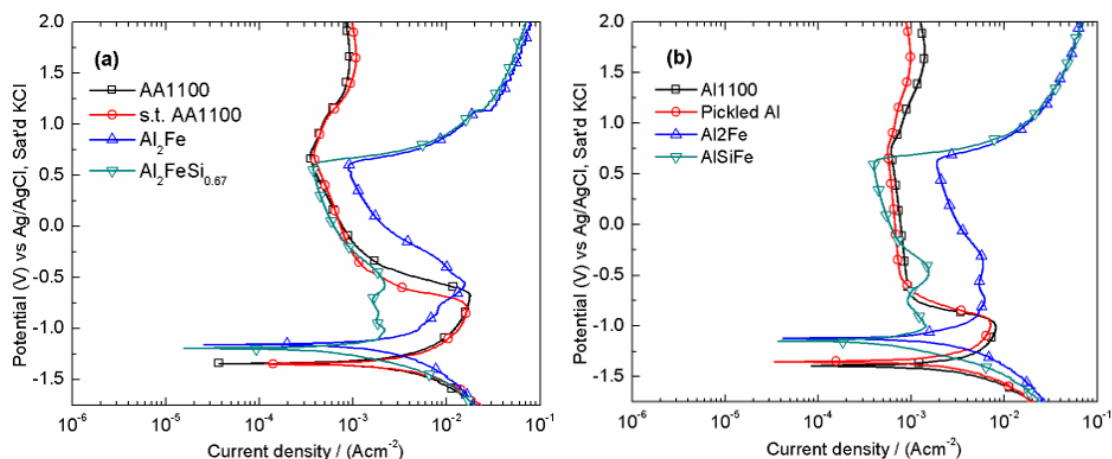
Figure 5.7 The potentiodynamic polarization curves of specimens tested in 1 M LiOH, with the addition of (a) 0.1 M and (b) 2 M Li_2SO_4.

The addition of 0.1 M $LiNO_3$ in 1 M LiOH solution shifts the E_{corr} of all electrodes to more noble values. It is found that the electrochemical potential difference between the intermetallic alloy and AA1100 reduced significantly after nitrate anions were added to the solution. In 0.1 M $LiNO_3$ electrolyte, the E_{corr} for AA1100, surface treated AA1100, Al_2Fe and $Al_2FeSi_{0.67}$ are -1.162, -1.188, -0.986 and -1.006 V, respectively. The electrochemical potential difference is even more close when 2 M $LiNO_3$ is added. the E_{corr} for AA1100, surface treated AA1100, Al_2Fe and $Al_2FeSi_{0.67}$ are -0.949, -0.965, -0.916, and -0.92 V, respectively. Addition of 2 M $LiNO_3$ in 1 M LiOH solutions also shifts the value of E_{corr} of all electrodes to more positive potentials. The pitting potential of other three electrodes shifts to more noble values, except AA1100 electrode. The polarization curves in figure 5.8a showed that the addition of 0.1 M $LiNO_3$ in 1 M LiOH solution significantly reduce the anodic dissolution rate of all electrodes above the E_{corr}. As it is shown in figure 5.8b, the inhibiting effect is strengthened when 2 M $LiNO_3$ is added to the solution, reducing the anodic current density by two orders of magnitude.

All electrodes presented passivity immediately above E_{corr}, which indicates that the addition of 2 M $LiNO_3$ effectively retards the selective aluminum dissolution from Al_2Fe and $Al_2FeSi_{0.67}$ alloy. In addition, addition of 2 M $LiNO_3$ effectively suppress the aluminum dissolution and the enrichment of Fe in intermetallic alloys in 1 M LiOH solution. Notably AA1100 electrodes did not show the breakdown of passivity in the scanned potential range.
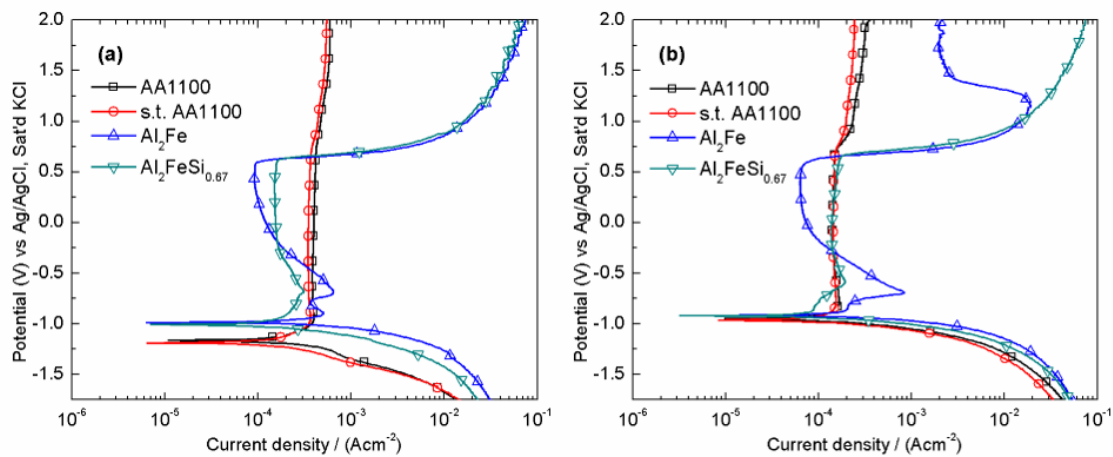
Figure 5.8 The potentiodynamic polarization curves of specimens tested in 1 M LiOH, with the addition of (a) 0.1 M and (b) 2 M $LiNO_3$.

In general, the cathodic polarization curves showed that the intermetallic alloys sustain higher cathodic current than AA1100 and surface-treated Al. The magnitude of cathodic current density measured follows the following order: $Al_2Fe>Al_2FeiSi_{0.67}>AA1100>$surface-treated AA1100.

5.3.3 Surface morphology after potentiodynamic polarization

Figure 5.9 shows the surface morphology of AA1100 electrode after polarization in 0.001 M LiOH, 2 M Li_2SO_4 electrolyte and the EDS mapping results. Circumferential pitting formed

due to the galvanic corrosion of aluminum matrix adjacent to intermetallic particles. EDS mapping results showed the distribution of Al-Fe and Al-Fe-Si intermetallic particles on surface and uniformly adsorbed sulfate species on electrode. The surface morphology and the EDS elemental distribution of surface-treated AA1100 in 2M Li_2SO_4, 0.001 M LiOH is presented in figure 5.10. The electrode surface retained the "dimples" feature by surface treatment and there was no presence of any intermetallic particles. The EDS mapping only showed the presence of Al, O and S elements on electrode surface. As the potentiodynamic polarization curves revealed that in 0.001 M LiOH 2 M Li_2SO_4 electrolyte, surface treated Al100 showed a wider range of passivity than AA1100. The increased pitting resistance is ascribed to the removal of intermetallic and the corresponding galvanic corrosion by surface treatment, as is evident from the surface morphologies after polarization. EDS mapping showed uniform distribution of sulfur on AA1100 eledtrodes, but there was no presence of sulfur on Al_2Fe and $Al_2FeiSi_{0.67}$ alloy. Sulfate anions were not incorporated into the surface passive layer of Al_2Fe and $Al_2FeiSi_{0.67}$ possibly due to the formation of a more stable oxidized iron passive film with low solubility in 0.001 M LiOH solutions.

Figure 5.11 shows the surface morphology of Al_2Fe after polarization in 1 M LiOH and the elemental distribution. It is evident that a corrosion product film formed on electrode surface during the polarization. Break down of such film layer occurred at E_p and leads to the exfoliation of the film and exposure of the relatively fresh alloy matrix beneath the surface layer. The corroded electrode surface clearly revealed grains of the Al_2Fe alloy, which indicates that there is a correlation between the grain orientations and the dissolution of aluminum in alkaline solution. EDS mapping showed the film covered on top only comprises Fe and O, with the presence of

only 3.5 wt.% of Al in matrix beneath the film, indicating that almost all of the Al in the intermetallic are selectively dissolved. As the atomic ratio of Fe to O is almost 4:1 on the film at area 1 and 1:1 on the exposed surface at area 2, considering that $Fe(OH)_3$ has the highest ration of Fe/O, 3:1 among the oxidized Fe species, pure Fe is generated in the corrosion product film due to the depletion of aluminum. Selective dissolution of Al was detected by EDS on all three components of the Al-Fe-Si alloy. The addition of 0.1 M and 2 M Li_2SO_4 in 1 M LiOH, impose no visible impact on the surface morphology and composition of the electrodes. EDS mapping results did not show the presence of sulfur on electrode, indicating that the surface adsorption of sulfate on AA1100 is weak in electrolytes containing high concentrations of OH^-.
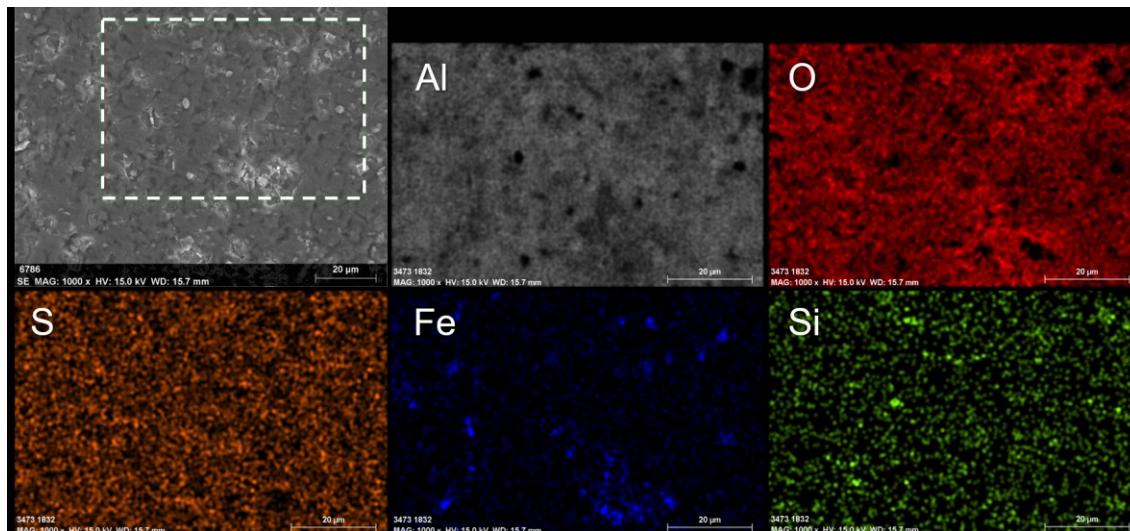
Figure 5.9 The surface morphology of AA1100 electrode after polarization in 0.001 M LiOH, 2 M Li_2SO_4 electrolyte and the EDS mapping results.
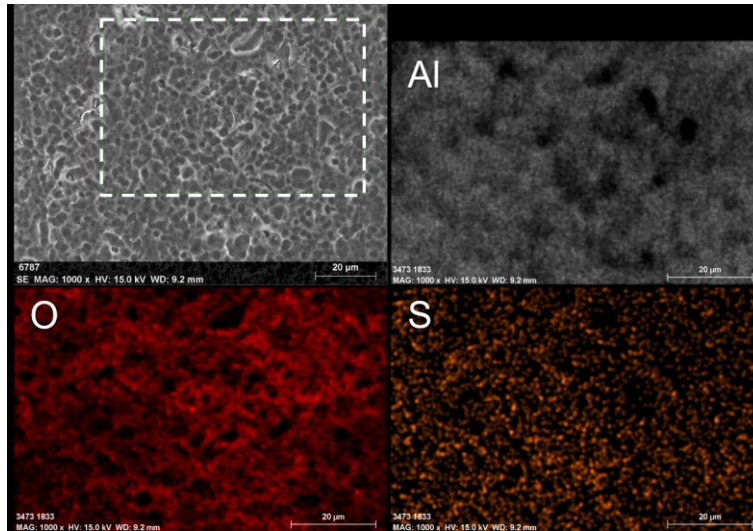
Figure 5.10 The surface morphology and the EDS mapping results on surface-treated AA1100 in 2 M Li_2SO_4, 0.001 M LiOH.

Figure 5.12 shows the surface morphology and EDS mapping results of surface treated AA1100 in 1 M LiOH, with the addition of 2 M $LiNO_3$. The surface of electrode AA1100 and surface-treated AA1100 was covered by a uniform layer of corrosion product. EDS mapping results only showed Al and O on the surface of surface treated AA1100, indicating that the electrode surface retained passivity so that the intermetallic particles in matrix are not exposed due to severe general corrosion. EDS mapping results shows that there is no evidence of nitrate adsorption on electrode surface. The suppression of Al dissolution is probably due to the chemical adsorption of nitrate and formation of hydroxide and oxy-hydroxide species on aluminum in alkaline solutions. Figure 5.13 shows that a thin layer of corrosion product covered uniformly on Al_2Fe electrode, although small areas of the passive film exfoliated possibly due to rapid hydrogen evolution on the electrode. Under high magnification, the corrosion product film revealed agglomerated nanoparticles that are around 200 nm in size. EDS point analysis results showed that the composition of the film at spot 1 and the matrix at spot 2 is $Al_{11}Fe_{44}O_{44}$ and

$Al_{20}Fe_{41}O_{38}$, respectively. The ratio of Fe to O is close to 1:1 all over the electrode. The surface composition is a reflection of the occurrence of selective dissolution of Al and oxidation of Fe on electrode surface, which well corresponds to the results depicted in anodic polarization curves. On $Al_2FeSi_{0.67}$ electrodes, generally the selective dissolution of Al occurred in the $Al_{54}Fe_{28}Si_{10}$ phase, which has the lowest content of Si, which might have resulted in its weak resistance to aluminum dissolution. $Al_{54}Fe_{28}Si_{10}$ phase has the least noble electrochemical potential in the multi-component system because $Al_{54}Fe_{28}Si_{10}$ has the least amount of noble component Fe and Si in composition.
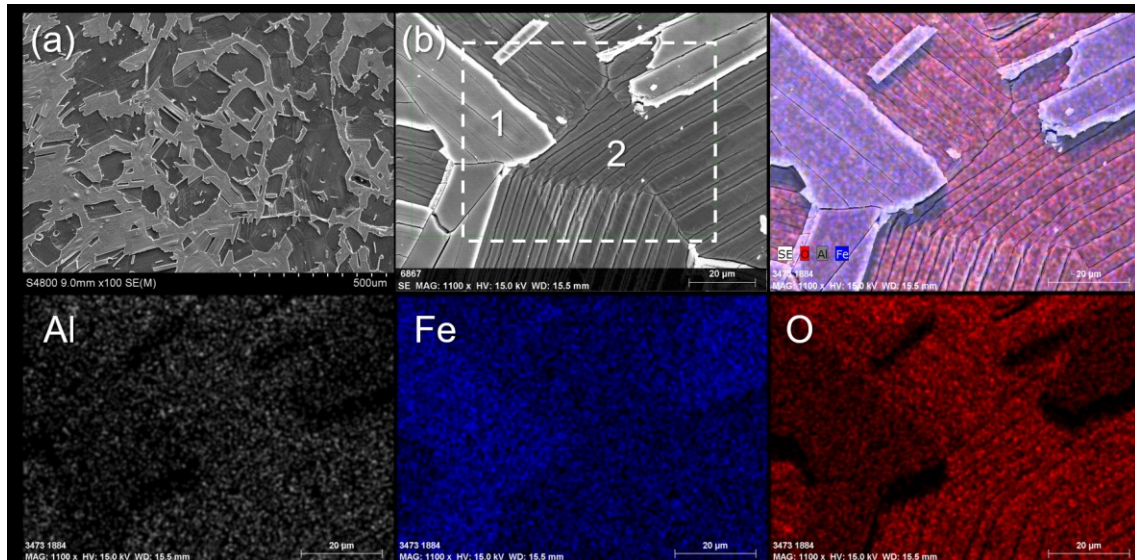
Figure 5.11 (a) The surface morphology of Al_2Fe after polarization in 1 M LiOH and (b) EDS mapping results.
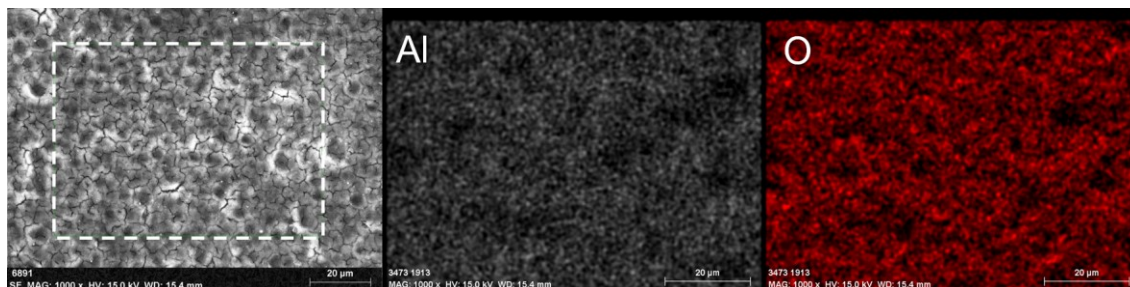
Figure 5.12 The surface morphology and EDS mapping results of surface treated AA1100 in 1 M LiOH, with the addition of 2 M LiNO$_3$ and EDS mapping results.

5.3.4 Raman Spectroscopy

The chemical status of passive film or corrosion product on electrode surface plays important role on determining the corrosion kinetics of aluminum and its alloys. The different surface morphologies and elemental composition on electrodes detected by SEM and EDS indicate that the surface of AA1100, surface treated AA1100, Al$_2$Fe and Al$_2$FeSi$_{0.67}$ may be composed of different corrosion products. As it was depicted in the electrochemical tests and surface elemental composition results, the alloys presented remarkable different corrosion behaviors in electrolytes with 1 M LiOH. Therefore, a comparison on the surface chemical status of these electrodes is believed to help understanding the different corrosion kinetics, such as the selective dissolution of aluminum, passivation, and break down of passivity. Raman spectroscopy was carried out on electrodes before and after potentiodynamic polarization in 1 M LiOH, and 1 M LiOH with the addition of 2 M Li$_2$SO$_4$ or 2 M LiNO$_3$ electrolytes. The Raman spectra of each electrode in 1 M LiOH, 1 M LiOH with addition of 2 M Li$_2$SO$_4$, 1 M LiOH with addition of 2 M LiNO$_3$ are presented in figure 5.14. The band positions are compared to band parameters reported in prior works and carefully analyzed. The band components and the tentative assignments for the spectrums are presented in table 5.3. All of the four freshly

133

prepared electrodes presented a very broad band in the range between 600 and 1200 cm^{-1} with low signal intensities, showing the presence an amorphous Al_2O_3 passive film forms on all the electrodes. The Raman spectra of AA1100 tested in 1 M LiOH depicted sharp bands at 1058, 1390 and 1513 cm^{-1}, which correspond to the aluminum hydroxide corrosion products formed on electrode during the polarization. In general, AA1100 and surface treated AA1100 all depicted the same bands in 1 M LiOH, and 1 M LiOH with the addition of 2 M $LiNO_3$. Surface treated AA1100 showed signal at 545 cm^{-1}, which is associated to Al-O-Al deformation, indicating the possible presence of a different hydroxide phase. In 1 M LiOH with the addition of 2 M Li_2SO_4 electrolyte, two bands with relatively low intensities presented on AA1100 and surface treated AA1100, which were assigned to v_2 and v_1 of SO_4^{2-}. However, considering the low intensity of the signal and the above compositional analysis, the adsorption of sulfate is believed to be weak, possibly because the competitive adsorption on aluminum surface is dominated by the highly concentrated hydroxide ions in solution.
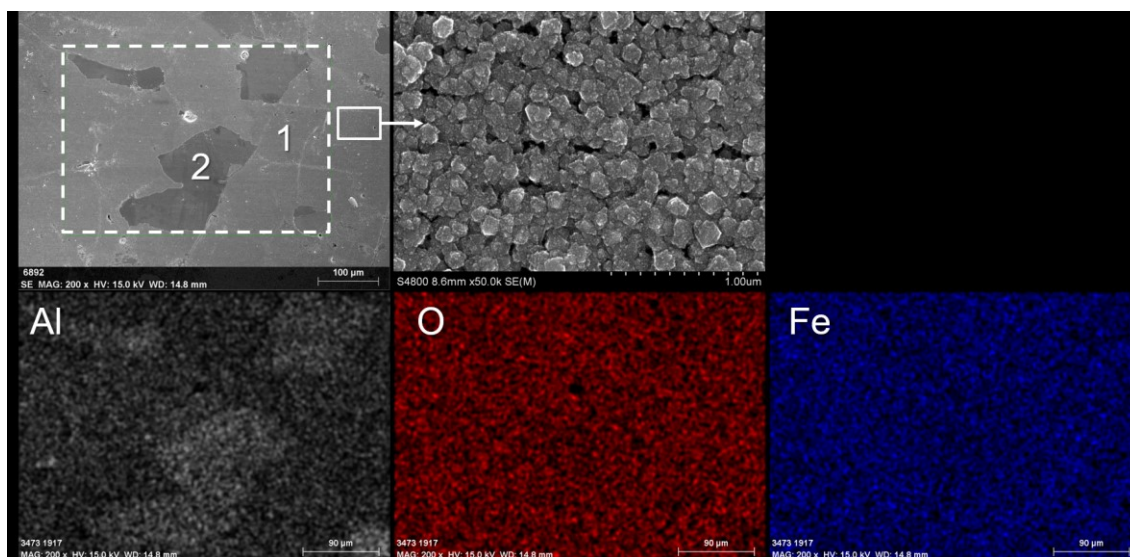
Figure 5.13 Surface morphology and EDS mapping results of Al_2Fe in 1 M LiOH, with the addition of 2 M $LiNO_3$.

134
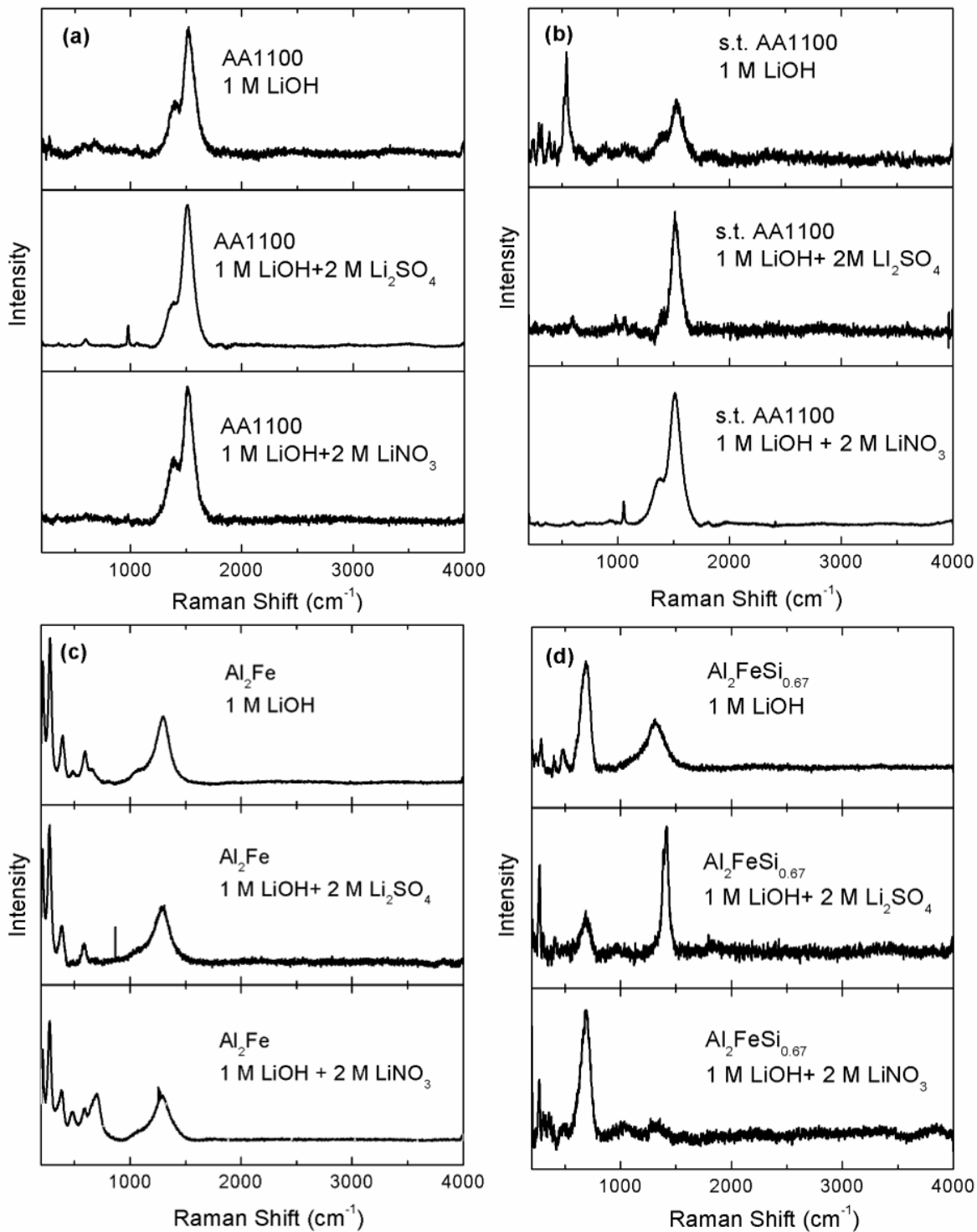
Figure 5.14 The Raman spectra of (a) AA1100, (b) surface treated AA1100, (c) Al_2Fe and (d) $Al_2FeSi_{0.67}$ in 1 M LiOH, 1 M LiOH with addition of 2 M Li_2SO_4, 1 M LiOH with addition of 2 M $LiNO_3$.

Table 5.3 Raman bands measured on AA1100 and intermetallic alloy surface after potentiodynamic polarization.

Test Condition	Specimen	peak (cm^{-1})	Tentative assignments
bare	Al1100	827	Amorphous Al_2O_3
	S Surface treated AA1100	819	
	Al_2Fe	820	
	$Al_2FeSi_{0.67}$	812	
1 M LiOH	Al1100	1058	Al-O and Al-OH bending mode
		1390	H_2O coordinated to AlO_4
		1513	H_2O coordinated to AlO_6
	Surface treated AA1100	545	Al-O-Al deformation
		1385	H_2O coordinated to AlO_4
		1517	H_2O coordinated to AlO_6
	Al_2Fe	216, 486,	A_{1g} modes, Fe_2O_3
		281, 395, 596	E_g modes, Fe_2O_3
		1303	Magnon scattering Fe_2O_3
	$Al_2FeSi_{0.67}$	193, 490, 688	A_{1g} modes, Fe_2O_3
		288, 401	E_g modes, Fe_2O_3
		1308	Magnon scattering Fe_2O_3
		688	A_{1g} modes, Fe_3O_4
1 M LiOH 2 M Li_2SO_4	Al1100	600	ν_2 SO_4 triplet
		976	ν_1 SO_4
		1387	H_2O coordinated to AlO_4
		1511	H_2O coordinated to AlO_6
	Surface treated AA1100	593	ν_2 SO_4 triplet
		984	ν_1 SO_4
		1387	H_2O coordinated to AlO_4
		1511	H_2O coordinated to AlO_6
	Al_2Fe	215, 486	A_{1g} modes, Fe_2O_3
		284, 396, 591	E_g modes, Fe_2O_3
		1300	Magnon scattering Fe_2O_3
	$Al_2FeSi_{0.67}$	215, 482,	A_{1g} modes, Fe_2O_3
		287. 402	E_g modes, Fe_2O_3
		1313	Magnon scattering Fe_2O_3
		688	A_{1g} modes, Fe_3O_4
1 M LiOH 5 M $LiNO_3$	Al1100	1058	Al-O and Al-OH bending mode
		1395	H_2O coordinated to AlO_4

	1522	H_2O coordinated to AlO_6
	1061	Al-O and Al-OH bending mode
Surface treated AA1100	1378	H_2O coordinated to AlO_4
	1512	H_2O coordinated to AlO_6
	214, 485,	A_{1g} modes, Fe_2O_3
	278. 387, 592	E_g modes, Fe_2O_3
Al₂Fe	1299	Magnon scattering Fe_2O_3
	701	A_{1g} modes, Fe_3O_4
	215, 478,	A_{1g} modes, Fe_2O_3
	282, 405	E_g modes, Fe_2O_3
Al₂FeSi₀.₆₇	1318	Magnon scattering Fe_2O_3
	685	A_{1g} modes, Fe_3O_4

After anodic polarization 1 M LiOH and 1 M LiOH with the addition of 2 M Li_2SO_4 electrolytes, the Raman spectra of Al_2Fe alloy was characterized by sharp bands at 216, 281, 395, 486, 596 and 1303 cm^{-1}. The bands are assigned to the A_{1g} modes, E_g modes, and magnon scattering of hematite, Fe_2O_3. [118,119] Since hematite is an antiferroumagnetic material, and the collective spin movement can be exited in a magnon. The intense signal at 1303 cm^{-1} is assigned to a two-magnon scattering which arises from the interaction of two magnons created on antiparallel close spin sites. [119] The same bands and another strong band at 688 cm^{-1} were detected on $Al_2FeSi_{0.67}$ alloy. The band revealed at 688 cm^{-1} was assigned to the A_{1g} mode of Fe_3O_4.[120,121] In 1 M LiOH with the addition of 2 M $LiNO_3$, the Raman spectra measured on Al_2Fe and $Al_2FeSi_{0.67}$ depicted different band features. The surface of Al_2Fe was characterized by bands associated to Fe_2O_3 and Fe_3O_4. Only one band at 697 cm^{-1} was detected on $Al_2FeSi_{0.67}$ alloy, indicating that there only Fe_3O_4 exists on the electrode surface.

5.4 Discussion

5.4.1 The role of sulfate and nitrate on anodic behavior of intermetallic alloys

In 0.001 M LiOH, the addition of sulfate anions inhibits the selective addition of AA1100 electrodes by surface chemical adsorption mechanism. When the concentration of hydroxyl is low, a competitive adsorption between sulfate and sulfate anions occurs and the hydroxyl anions are repelled from electrode surface. In addition, the incorporation of sulfate anions in passive film results in the formation of protective basic aluminum sulfate passive film, which attributes to the inhibition on aluminum dissolution. Since EDS mapping did not show the presence of sulfur on Al_2Fe surface, the reduced selective dissolution of Al on Al_2Fe alloy in 2 M Li_2SO_4 is due to the structural change of the aqueous electrolytes. However, the adsorption of hydroxyl anions dominants the surface adsorption process at 1 M concentration level, as evident by the absence of sulfur from EDS mapping and the weak signal of sulfate detected in Raman spectra. Thus sulfate does not impose any inhibiting effect on AA1100 electrodes and intermetallic alloys in 1 M LiOH electrolyte.

Although the addition of nitrate anions in 0.001 M LiOH does not suppress the dissolution rate of Al in intermetallic alloys, notably the electrochemical potential difference between Al_2Fe and AA1100 became smaller after the addition of nitrate. The small electrochemical potential difference between AA1100 and intermetallic weakens the electrochemical driving force for galvanic corrosion, indicating that the addition of nitrate anions reduces the tendency of AA1100 towards pitting corrosion. In 1 M LiOH electrolyte, the addition of $LiNO_3$ effectively inhibits the dissolution of AA1100 and the selective dissolution of Al in intermetallic alloys. The electrochemical potential of AA1100 and intermetallic alloys is small after nitrate is added. The improved corrosion resistance against pitting may be explained by (i)

the reduced electrochemical potential difference and (ii) the suppression of cathodic activities on intermetallic alloys.

Raman spectra results showed that the formation of Fe_2O_3 film on Al_2Fe in 1 M LiOH. Meanwhile EDS point analysis confirmed that aluminum on the alloy surface is almost depleted. The same phenomenon was observed on Al_2Fe in 1 M LiOH, 2 M Li_2SO_4. With the addition of 2 M $LiNO_3$ electrolyte, the surface passive film depicted the presence of Fe_3O_4 and Fe_2O_3. The concurrent formation of Fe_3O_4 and the decreased anodic dissolution activity above E_{corr} indicates Fe_3O_4 attributed to the suppressed selective dissolution occurred on Al_2Fe. This can be proved by the fact that the selective dissolution of Al is only retarded in 1 M LiOH with the addition of $LiNO_3$. Notably, Fe_2O_3 formed on intermetallic surface in all test conditions, which contributed to the reduced current following selective dissolution of aluminum at higher anodic potentials.

5.4.2 The role of Fe and Si on the electrochemical behavior of intermetallic alloys

Both the anodic and cathodic activities of intermetallic alloys are dominated by the electrochemically noble components, Fe and Si. The amount of Fe in intermetallic particles has significant effect on the cathodic reaction, as is evident by the high cathodic reactivity on Al_2Fe alloy. It is possible that the addition of Si in intermetallic improves the corrosion resistance of the alloy possibly because the incorporation of Si into Al_2O_3 passive film repairs defects in the oxide layer and reduce the dissolution rate of passive film. Si may contribute to the suppression of the preferable dissolution of Al in intermetallic alloy by the same mechanism. However, as Raman spectra didn't show any bands that corresponds to Si, the suppressed aluminum dissolution in Si-rich phase may be simply due to the lower content of Fe in the same phase.

5.5 Conclusion

The corrosion behavior of AA1100, surface treated AA1100 with "intermetallic-free" surface, synthesized Al_2Fe and $Al_2FeSi_{0.67}$ intermetallic alloys was studied in 0.001 M LiOH, 1 M LiOH with the addition of $LiNO_3$ and Li_2SO_4 electrolytes. The obtained results are summarized as follows:

1. The potentiodynamic polarization curves showed that the intermetallic alloys have noble corrosion potentials than AA1100 and surface treated AA1100. The anodic dissolution above E_{corr} measured on intermetallic alloys is associated to the selective dissolution of Al. The addition of sulfate anions does not impact the selective dissolution process. The addition of nitrate anions, however, reduces the electrochemical differences between AA1100 and synthesized intermetallic alloys and suppresses the selective dissolution of Al from intermetallic alloys. Nitrate anions suppress the pitting due to galvanic corrosion on aluminum. The cathodic polarization curves showed that the intermetallic alloys sustain higher cathodic current than AA1100 and surface-treated Al. The magnitude of cathodic current density measured on the electrodes follows the following order: $Al_2Fe>Al_2FeSi_{0.67}>AA1100>$surface-treated AA1100.

2. The surface morphology and EDS results showed that the depletion of Al on Al_2Fe intermetallic alloys occurred in alkaline solutions, which agrees with the potentiodynamic polarization measurements. The adsorption of sulfate on Al occurred in 0.001 M LiOH but not in 1 M LiOH solution due to the competitive adsorption between sulfate and hydroxyl anions. Nitrate inhibited the corrosion of Al in alkaline solutions by chemical adsorption reaction with hydroxyl and Al.

3. Raman spectra revealed that the inhibiting effect of $LiNO_3$ on selective dissolution of aluminum is due to the formation of Fe_3O_4 passive film above the corrosion potential. Fe_2O_3 film formed on all intermetallic alloys, which accounts for the occurrence of passivity following selective dissolution of Al at higher anodic potentials.

CHAPTER 6 Summary

The development of next-generation energy storage systems requires sophisticated materials design and comprehensive knowledge of the compatibility of materials in the system. The recent developed aqueous-based cathode slurry solvent and aqueous-rechargeable lithium ion battery eliminates the use of toxic, flammable organic solvents, reduces the production cost, and improves the design flexibility. However, such new aqueous-based technologies often use basic aqueous solutions with high pH value, which brings concerns on the possible occurrence of aluminum current collector corrosion. Corrosion of aluminum current collector results in solid corrosion products that increases the internal impedance, localized corrosion that degrades the adhesion between active materials and conductive substrate, and dissolved aluminum species that contaminates the electrolyte, which impairs the cell performance, service life and safety. Evaluating the corrosion-resistance and electrochemical stability of Al current collector is important for the management of component corrosion during the design of energy storage systems. In addition, development of protection methodologies and approaches that could suppress aluminum corrosion, such as design of alloy composition, addition of inhibitors, is rendered necessary by the vast applications of aluminum alloys in industries. A throughout understanding on the corrosion mechanisms, corrosion kinetics, structural and compositional change of aluminum in alkaline solutions would shed lights on the development of such corrosion inhibiting strategies. The outcomes of this work, which are summarized below, are considered useful in predicting the corrosion behavior of aluminum alloys, design of corrosion-resistant alloys and aluminum alloy corrosion inhibitors.

6.1 Effect of Aqueous-based Cathode Slurry pH and Immersion Time on Corrosion of Aluminum Current Collector in Lithium-ion Batteries

In the fabrication of lithium ion battery cathode using aqueous based cathode slurries, the corrosion process on aluminum current collector is controlled by the slurry pH and the time period that aluminum exposes to the wet slurry. Localized corrosion occurred on AA1085 in the form of circumferential pitting, which was ascribed to galvanic corrosion between aluminum matrix and Al-Fe and Al-Fe-Si intermetallic particles. The density and size of the pitting corrosion increased with increasing slurry alkaline pH value and the elapsing immersion time. The chemical state of passive film on AA1085 foil is not affected by the active materials such as NMC (nickel manganese cobalt oxide) in aqueous slurry. The film on AA1085 surface gradually degrade into hydroxide with elapsing immersion time. The electrochemical characteristics of AA1085 in aqueous slurry was measured by potentiodynamic polarization and electrochemical impedance spectroscopy. The corrosion resistance of AA1085 showed a strong dependence on pH value and the immersion time, which are in consistent with the corrosion results obtained from exposure tests in aqueous slurries. The time-pH-variant electrochemical response was ascribed to the change of passive film and electric double layer properties.

6.2 Electrochemical Stability of Aluminum Current Collector in Aqueous Rechargeable Lithium-ion Batteries

The electrochemical stability of AA1085 current collector in 2 M Li_2SO_4 and 5 M $LiNO_3$ electrolytes with pH in the range of 5 to 11 was evaluated by cyclic voltammetry, linear sweep voltammetry and chromoamperometry. Aluminum current collector showed high corrosion resistance in neutral and close neutral electrolytes (pH 5, 7 and 9). Crystallographic pitting

corrosion occurred on AA1085 in 2 M Li$_2$SO$_4$ at pH 11. A uniform layer of corrosion product with the thickness of 2 microns formed on AA1085 in LiNO$_3$ electrolyte at pH 11 and prevented aluminum from pitting corrosion. Raman spectra of electrode surface showed the presence of sulfate and nitrate species after CV in pH 11 condition. The chemical adsorption mechanisms of sulfate and nitrate anions on AA1085 in slightly alkaline solution was proposed. The adsorption of anions assists inhibiting aluminum pitting though competitive chemical adsorption with OH$^-$ in slightly alkaline solutions. Sulfate ions were incorporated into the aluminum surface passive film in alkaline solution and results in the formation an ion-selective basic aluminum salt film while nitrate ions weren't, although the inhibiting effect of the basic aluminum sulfate is limited due to its low stability in alkaline solutions. The occurrence of detrimental pitting corrosion in 2 M Li$_2$SO$_4$ electrolyte, and the considerable amount of corrosion product and high concentration of dissolved aluminum species in 5 M LiNO$_3$ is believed to eventually impair the battery performance. AA1085 current collector is not applicable to be used in both electrolytes at pH 11.

6.3 Effects of Sulfate and Nitrate Anions on Aluminum Corrosion in Slightly Alkaline Solution

The corrosion mechanism and corrosion kinetics of AA1085 in slightly alkaline Li$_2$SO$_4$ and LiNO$_3$ ARLB electrolytes was controlled by the type of anions, electrolyte concentration and applied anodic potentials. Concentrate sulfate anions inhibit aluminum from rapid pitting growth due to the formation of a cation-selective basic aluminum sulfate passive film. However, such inhibiting effect is not lasting under high anodic potentials. Repassivation occurs on AA1085 in LiNO$_3$ at pH 11 and a hydroxide-oxyhydroxide corrosion product film formed on surface. The thick corrosion product layer serves as a barrier film that reduces the potential gradient across the

electrode/solution interface and impede the aggression of hydroxyl anions thus pitting growth is suppressed. The kinetics of pitting corrosion and repassivation process on AA1085 is enhanced at higher anodic potentials. the amount of free water molecular as solvents for dissolved aluminum complexes reduces with increasing electrolyte concentration. The reduced dissolubility of the electrolyte is believed to affect the transportation of dissolved aluminum species from the electrode/solution interface to bulk solution, which consequently impede the dissolution of aluminum.

6.4 Effects of Sulfate and Nitrate on the Electrochemical Behavior of Al-Fe and Al-Fe-Si Intermetallic in Alkaline Solutions

The inevitable existence of intermetallic particles in high purity aluminum makes them an important role in corrosion process of aluminum. Due to the electrochemical potential variation between the intermetallic particles and its surrounding matrix, the intermetallic phases containing Fe act as cathode sites during galvanic corrosion. The electrochemical behavior of AA1100, surface treated "intermetallic free" AA1100, synthesized Al_2Fe and AlFeSi intermetallic alloys in alkaline solutions containing sulfate and nitrate anions are investigated. The addition of sulfate and nitrate anions played important role on the preferable dissolution of aluminum above corrosion potential and consequently affects the cathodic efficiency of intermetallic particles. In general, intermetallic alloys presented noble corrosion potentials compared to AA1100 specimens. The addition of sulfate anions in the solution does not suppress the selective dissolution of aluminum on intermetallic alloys in 0.001 M and 1 M LiOH solutions, which increases the cathodic efficiency of intermetallic alloys and promotes the galvanic corrosion. The corrosion potential difference is significantly reduced when 2 M $LiNO_3$ is added into the alkaline

solution. Meanwhile the anodic dissolution rate that corresponds to the preferable dissolution of Al also decreases. Raman spectra revealed that the inhibiting effect of $LiNO_3$ on selective dissolution of aluminum is due to the formation of Fe_3O_4 passive film above the corrosion potential. the cathodic polarization curves showed that the intermetallic alloys sustain higher cathodic current than AA1100 and surface-treated Al. The magnitude of cathodic current density measured follows the following order: $Al_2Fe > Al_2FeSi_{0.67} > AA1100 >$ surface-treated AA1100. The change of composition, structure during anodic polarization on the intermetallic surface influences the selective dissolution of aluminum, the passivity status and in turn affects the cathodic efficiency of the intermetallic.

6.5 Novelty of this work

Prior work focused on the corrosion of aluminum current collectors in organic-based lithium-ion battery systems. The effects of lithium salts and organic electrolyte solvents on the stability of current collector and the possible inhibiting methods was studied extensively. This work addresses the corrosion behavior, corrosion mechanisms and kinetics of aluminum current collector in aqueous-based cathode slurries and ARLB electrolytes, which expands the knowledge on the chemical and electrochemical stability of commercial purity aluminum in aqueous-based alkaline environments.

The influence of immersion time and pH on the corrosion behavior of aluminum current collector in alkaline aqueous-based slurry was qualitatively characterized by X-ray photon-electron spectroscopy, and quantitatively measured by electrochemical impedance spectroscopy approach. Tests were designed to characterize the change of surface composition, the corresponding equivalent circuit models and the fitted parameters for the corrosion elements

with increasing immersion time at various pH conditions. The discussion on the corrosion evolution of aluminum in aqueous slurry is useful for the design of aqueous-based binder chemistries to keep the continuity of aluminum current collector in long-term battery service.

The corrosion kinetics of AA1085 in alkaline aqueous solution containing sulfate anions and nitrate anions was investigated and discussed in detail for the first time. Combining all the findings on the electrochemical characteristics, composition and structure of passive film, corrosion behavior of aluminum, whether the corrosion process was accelerated or inhibited, the adsorption mechanisms of anions and their effects on the surface chemical and electrochemical process, and the reaction kinetics occurred on aluminum were revealed.

The dissolubility of water as solvent in electrolyte was considered as a factor that affects the equilibrium of the aluminum dissolution reaction in aqueous condition. The change of dissolubility of electrolyte shifts the equilibrium of aluminum dissolution reactions. The influence of solution structure on the mass transport rate of soluble aluminum species was correlated to the pitting growth kinetics of AA1085 as a part of the environmental factors.

By comparing the electrochemical polarization response of Al1100, synthesized bulk alloys with the same ratio of element components, and "intermetallic free" Al1100 by the use of "intermetallic removal" surface processing technique, the role of Al-Fe and Al-Fe-Si intermetallic particles on the corrosion behavior, especially the galvanic corrosion of commercial purity Al1100 was presented. The effect of sulfate and nitrate on the preferable dissolution of aluminum in intermetallic compound was revealed.

6.6 Limitation of this work

In this work, the electrochemical stability and corrosion kinetics of aluminum current collector are studied in simulated electrochemical conditions without considering more complex chemistries and service conditions involved in the service life of an actual lithium ion battery, which includes the composition of active electrode materials, the porous structure of cathode and the charge/discharge cycles. These electrochemical testing approaches are also employed in prior works. Further insights into corrosion of aluminum current collector in the environment of interest and its impacts on battery performance might be possible by investigating long term, cycle life tested batteries for evidence of corrosion, and possible effects like detachment of active materials and electrolyte contamination. Although a three-electrode cell with a small volume of electrolyte was used in electrochemical measurements, considerable larger amount electrolyte is used compared to that used in an actual lithium ion battery, considering the ratio of electrolyte volume to electrode area. The excessive amount of electrolyte might exaggerate their effects on corrosion of aluminum current collector and possibly introduce more environmental variables due the existence of solution impurities.

6.7 Future work

This work shows that sulfate and nitrate alone cannot serve as effective inhibitors on aluminum corrosion in alkaline solutions. The chemical adsorption of sulfate and nitrate occurs on aluminum in different mechanisms. Sulfate can incorporate into the passive film on aluminum surface, and results in the formation of a cation selective basic aluminum sulfate layer. This cation selective layer may impede the ingression of aggressive anions and retard the crystallization of hydroxide corrosion products on aluminum surface. However, the

148

protectiveness of this basic aluminum salt film is low due to its limited stability in alkaline solutions. Nitrate anions adsorb on aluminum surface through chemical reaction with hydroxide anion and aluminum. The reaction results in a thick corrosion product film. In addition, the presence of concentrated nitrate anions reduces the cathodic efficiency of noble intermetallic particles so the pitting growth is impeded. Although the hydroxide-oxyhydroxide corrosion product protects aluminum from severe localized corrosion, the formation of this thick barrier film results in high concentration of dissolved aluminum species.

Considering the inhibiting mechanisms of sulfate and nitrate anions and their unique effects on the composition and structure of passive film, these two anions may be combined with other oxidizers as an, non-toxic, environmental friendly inhibitor package for aluminum protection in aqueous solutions. The inhibiting efficiency can be optimized by tailoring their roles on enhancing the corrosion resistance and meanwhile minimizing effects due to their drawbacks as an inhibitor so that a passivating coating that inhibits both the anodic and cathodic reaction is developed. As a continuous research based on this work, design and evaluation of such environmental friendly inhibitor package for aluminum would be a research field that worth to work on.

REFERENCES

1. G. E. Trotten and D. S. MacKenzie, *Handbook of Aluminum*, p. 185-194, MARCEL DEKKER, INC, NEW YORK, (2003)

2. A. H. Whitehead and M. Schreiber, *J. Electrochem. Soc.*, **152**, A2105–A2113 (2005).

3. J. W. Braithwaite, *J. Electrochem. Soc.*, **146**, 448 (1999).

4. L. P. H. Jeurgens, W. G. Sloof, F. D. Tichelaar, and E. J. Mittemeijer, *J. Appl. Phys.*, **92**, 1649–1656 (2002).

5. B. C. Bunker, G. C. Nelson, K. R. Zavadil, J. C. Barbour, F. D. Wall, and J. P. Sullivan, C. F. Windisch Jr., M. H. Engelhardt, and D. R. Baer Pacific*, J. Phys. Chem. B*, **106**, 4705–4713 (2002)

6. N. Cai, G. Zhou, K. Müller, and D. E. Starr, *Phys. Rev. B - Condens. Matter Mater. Phys.*, **84**, 1–6 (2011).

7. Y. I. Seo, Y. J. Lee, D.-G. Kim, K. H. Lee, and Y. Do Kim, *Appl. Surf. Sci.*, **256**, 4434–4437 (2010)

8. X. Zhang et al., *Appl. Surf. Sci.*, **256**, 7300–7304 (2010)

9. O. Seri and K. Furumata, *Mater. Corros.*, **53**, 111–120 (2002).

10. F. Zhang, Y. Yang, W. S. Cao, S. L. Chen, and K. S. Wu, *ASM Handbook on Metals Process Simulation*, **22** (2010).

11. J. Xiao and S. Chaudhuri, *Electrochim. Acta*, **56**, 5630–5641 (2011)

12. N. Birbilis and R. G. Buchheit, *J. Electrochem. Soc.*, **155**, C117 (2008)

13. R. Ambat, A. J. Davenport, G. M. Scamans, and A. Afseth, *Corros. Sci.*, **48**, 3455–3471 (2006).

14. K. Nişancioğlu, *J. Electrochem. Soc.*, **137**, 69 (1990).

15. M. K. Cavanaugh, J.-C. Li, N. Birbilis, and R. G. Buchheit, *J. Electrochem. Soc.*, **161**, C535–C543 (2014)

16. J. M. Tarascon and M. Armand, *Nature*, **414**, 359–367 (2001)

17. N. Alias and A. A. Mohamad, *J. Power Sources*, **274**, 237–251 (2015)

18. D. Li, W., Dahn, J. R. & Wainwright, *Scienc.*, **264**, 1115–1118 (1994).

19. H. Buqa, M. Holzapfel, F. Krumeich, C. Veit, and P. Novák, *J. Power Sources*, **161**, 617–622 (2006).

20. B. Scrosati, J. Hassoun, and Y.-K. Sun, *Energy Environ. Sci.*, **4**, 3287 (2011)

21. F. Alloin et al., *J. Electrochem. Soc.*, **160**, A3171–A3178 (2013)

22. X. Wang, Y. Hou, Y. Zhu, Y. Wu, and R. Holze, *Sci. Rep.*, **3**, 1401 (2013)

23. C. Wessells, R. Ruffo, R. A. Huggins, and Y. Cui, *Electrochem. Solid-State Lett.*, **13**, A59 (2010).

24. H. Kim,J. Hong, K. Park, H. Kim, S. Kim and K. Kang, *Cheml Reviews,* **114** , 11788-11827 (2014).

25. Y. G. Wang, J. Y. Luo, C. X. Wang, and Y. Y. Xia, *J. Electrochem. Soc.*, **153**, A1425–A1431 (2006).

26. Y. Wang, J. Yi, and Y. Xia, *Adv. Energy Mater.*, **2**, 830–840 (2012).

27. R. Ruffo, C. Wessells, R. a. Huggins, and Y. Cui, *Electrochem. commun.*, **11**, 247–249 (2009)

28. K. Naito, T. Matsunami,K. Okuno,M.Matsuoka and C. Iwakura, *J. Appl. Electrochem.*, 23, 1051 (1993)

29. T. C. Hyams, J. Go, and T. M. Devine, *J. Electrochem. Soc.*, **154**, C390 (2007)

30. X. Zhang and T. M. Devine, *J. Electrochem. Soc.*, **153**, B344 (2006)

31. S. S. Zhang and T. R. Jow, *J. Power. Sources*, **109**, 458–464 (2002).

32. X. Zhang, B. Winget, M. Doeff, J. W. Evans, and T. M. Devine, *J. Electrochem. Soc.*, **152**, B448 (2005)

33. H. Yang, K. Kwon, T. M. Devine, and J. W. Evans, *J. Electrochem. Soc.*, **147**, 4399 (2000)

34. M. Morita, T. Shibata, N. Yoshimoto, and M. Ishikawa, *Electrochimica Acta*, **47**, 2787–2793 (2002).

35. E. Cho, J. Mun, O.B. Chae, O.M. Kwon, H.T. Kim, J.H. Ryu, Y.G. Kim and M.O. Seung, *Electrochem. commun.*, **22**, 1–3 (2012)

36. M. M. Fares, A. K. Maayta, and J. A. Al-Mustafa, *Corros. Sci.*, **65**, 223–230 (2012)

37. Y. Li and P. S. Fedkiw, *Electrochim. Acta*, **52**, 2471–2477 (2007)

38. Y. Li, X.-W. Zhang, S. a. Khan, and P. S. Fedkiw, *Electrochem. Solid-State Lett.*, **7**, A228 (2004).

39. X. Zhang and T. M. Devine, *J. Electrochem. Soc.*, **153**, B365 (2006)

40. S.-T. Myung, Y. Hitoshi, and Y.-K. Sun, *J. Mater. Chem.*, **21**, 9891 (2011)

41. I. Doberdò et al., *J. Power Sources*, **248**, 1000–1006 (2014)

42. M. C. Kimble, A. S. Woodman, and E. B. Anderson, **3** (1999).

43. B. Scrosati, J. Hassoun, and Y.-K. Sun, *Energy Environ. Sci.*, **4**, 3287 (2011).

44. J. B. Goodenough and K. S. Park, *J. Am. Chem. Soc.*, **135**, 1167–1176 (2013).

45. C. C. Li and Y. W. Wang, *J. Power Sources*, **227**, 204–210 (2013)

46. J. W. Braithwaite, *J. Electrochem. Soc.*, **146**, 448 (1999).

47. B. Zaid, D. Saidi, A. Benzaid and S. Hadji, *Corros. Sci.*, **50**, 1841–1847 (2008)

48. S. Adhikari and K. R. Hebert, *Corros. Sci.*, **50**, 1414–1421 (2008)

49. N. Birbilis and R. G. Buchheit, *J. Electrochem. Soc.*, **152**, B140 (2005)

50. B. C. Church, D. T. Kaminski, and J. Jiang, *J. Mater. Sci.*, **49**, 3234–3241 (2014)

51. R. Behavior, O. F. A.- Aluminum, and A. Sheets, *Light Met.* (2013).

52. J. Stojadinović, A. Dushina, R. Trócoli, and F. La Mantia, *Chempluschem*, **79**, 1507-1511 (2014)

53. M. R. Alexander, G. E. Thompson, and G. Beamson, **477**, 468–477 (2000).

54. C. D. Wagner, *J. Vac. Sci. Technol.*, **21**, 933 (1982).

55. B. J. Tan, K. J. Klabunde, and P. M. a Sherwood, *J. Am. Chem. Soc.*, **113**, 855–861 (1991)

56. J. A. Rotole, *Surf. Sci. Spectra*, **5**, 4 (1998)

57. J.-B. Wang, J.-M. Wang, H.-B. Shao, J.-Q. Zhang, and C.-N. Cao, *J. Appl. Electrochem.*, **37**, 753–758 (2007)

58. F. M. Reis, H. G. De Melo, and I. Costa, *Electrochim. Acta*, **51**, 1780–1788 (2006).

59. J. B. Wang et al., *Mater. Corros.*, **60**, 269–273 (2009)

60. G. J. Brug, A.L.G. van den Eeden, M. Sluyters-Rehbach, and J. H. Sluyters, *J. Electroanal. Chem. Interfacial Electrochem.*, **176**, 275–295 (1984).

61. M. I. Kazunari Soeda, Masaki Yamagata, *ECS Trans.*, **64**, 13–22 (2015).

62. C. Wessells, R. a. Huggins, and Y. Cui, *J. Power Sources*, **196**, 2884–2888 (2011)

63. W. Song, X. Ji, Y. Zhu, H. Zhu, F. Li, J. Chen, F. Lu, Y. Yao and C.E. Banks. *ChemElectroChem*, **1**, 871–876 (2014)

64. G.J.Wanga, N.H. Zhaoa, L.C. Yanga,Y.P. Wu, H.Q.Wua, R. Holze, *Electrochim. Acta*, **52**, 4911–4915 (2007).

65. B. C. Church, D. T. Kaminski, and J. Jiang, *J. Mater. Sci.*, **49**, 3234–3241 (2014)

66. S. Y. Li and B. C. Church, *Mater. Corros.*, **67**(9), 978-987 (2016)

67. M. Zhao, G. Huang, F. Qu, F. Wang, and X. Song, *Electrochim. Acta*, **151**, 50–55 (2015)

68. S.-I. Pyun and S.-M. Moon, *J. Solid State Electrochem.*, **3**, 331–336 (1999).

69. J. L. Trompette, L. Arurault, S. Fontorbes, and L. Massot, *Electrochim. Acta*, **55**, 2901–2910 (2010)

70. F. Branzoi, V. Branzoi, M. V. Popa, and F. Golgovici, *Mater. Corros.*, **51**, 635–641 (2000)

71. C. M. A. Brett, I. a R. Gomes, and J. P. S. Martins, *J. Appl. Electrochem.*, **24**, 1158–1163 (1994).

72. J. Ma, J. Wen, J. Gao, and Q. Li, *Electrochim. Acta*, **129**, 69–75 (2014)

73. H. D. Ruan, R. L. Frost, and J. T. Kloprogge, *J. Raman Spectrosc.*, **32**, 745–750 (2001).

74. J. Kloprogge and R. Frost, *J. Mater. Sci.*, **4**, 4199–4202 (1999)

75. A. M. Ahern, P. R. Schwartz, and L. A. Shaffer, *Appl. Spectrosc.*, **46**, 1412–1419 (1992).

76. N. J. Cherepy, T. H. Shen, A. P. Esposito, and T. M. Tillotson, *J. Colloid Interface Sci.*, **282**, 80–86 (2005).

77. J. T. Kloprogge and R. L. Frost, *Spectrochim. Acta Part A Mol. Biomol. Spectrosc.*, **55**, 1505–1513 (1999)

78. J. . Kloprogge and R. . Frost, *Spectrochim. Acta Part A Mol. Biomol. Spectrosc.*, **55**, 163–169 (1998)

79. D. Tromans, *J. Electrochem. Soc.*, **152**, B460 (2005)

80. M. A. Amin, S. S. Abd El Rehim, and A. S. El-Lithy, *Corros. Sci.*, **52**, 3099–3108 (2010)

81. F. N.-C. M.L. Doche, J.J. Rameau, R. Durand, *Corros. Sci.*, **41**, 805–826 (1999).

82. R. T. Foley and T. H. Nguyen, *J. Electrochem, Soc.,* 464–467 (1982).

83. I. Povar and O. Spinu, *Cent. Eur. J. Chem.*, **12**, 877–885 (2014)

84. J. C. Fanning, *Coord. Chem. Rev.*, **199**, 159–179 (2000)

85. R. T. Foley and T. H. Nguyen, *J. Electrochem. Soc.*, **129**, 27–32 (1982).

86. I. M. and N. H. Z.H. Dan, *ECS Trans.*, **25**, 23–33 (2010).

87. A.M. BECCARIA and G. POGGI, *Corrosion*, **43**, 153–158 (1987).

88. J. Zhang, M. Klasky, and B. C. Letellier, *J. Nucl. Mater.*, **384**, 175–189 (2009)

89. K. H. Na and S. Il Pyun, *Electrochim. Acta*, **52**, 4363–4373 (2007).

90. T. S. Humphries, *Low Toxic Corrosion Inhibitors for Aluminum in Fresh Water*, (1978).

91. Y. Yamada et al., *ChemElectroChem*, **2**, 1687–1694 (2015).

92. S. S. Abdel Rehim, H. H. Hassan, and M. A. Amin, *Corros. Sci.*, **46**, 1921–1938 (2004)

93. G. J. Hills, D. J. Schiffrin, and J. Thompson, *Electrochim. Acta*, **19**, 671–680 (1974).

94. H. Habazaki, R. Nishimura, K. Okisu, H. Inoue, I. Kiriyama, F. Kataoka, M. Sakairi, H. Takahashi. *J. Solid State Electrochem.*, **18**, 369–376 (2014).

95. M. Barbosa, *Corrosion*, **44**, 149–153 (1988).

96. S.-M. Moon and S.-I. Pyun, *J. Solid State Electrochem.*, 104–110 (1999).

97. S. S. El-Egamy and W. A. Badaway, *J. Appl. Electrochem.*, **34**, 1153–1158 (2004).

98. S. Y. Li and B. C. Church, *Mater. Corros.*, **67**, 978–987 (2016).

99. S. S. A. Rehim, H. H. Hassan, and M. A. Amin, *Appl. Surf. Sci.*, **187**, 279–290 (2002)

100. X. R. Yu, F. Liu, Z. Y. Wang, and Y. Chen, *J. Electron Spectros. Relat. Phenomena*, **50**, 159–166 (1990).

101. P. Klomjit and R. G. Buchheit, *Corrosion*, **72**, 486–499 (2015).

102. J. R. Lindsay, H.J. Rose, W.E. Swartz, Jr., P.H. Watts, Jr. and K.A. Raybrun. *Appl. Spectrosc.*, **27**, 1–5 (1973).

103. J. C. Klein and D. M. Hercules, *J. Catal.*, **82**, 424–441 (1983).

104. G. E. Walraten and R. T. W. Douglas, *J. Chem. Phys.*, **124** (2006).

105. J. Palacký, P. Mojzeš, and J. Bok, *J. Raman Spectrosc.*, **42**, 1528–1539 (2011).

106. S. Adhikari, Alkaline dissolution of aluminum: surface chemistry and subsurface interfacial phenomena (2008).

107. J. J. Friel, *Corrosion*, **42**, 422–426 (1986).

108. T. E. Graedel, *J. Electrochem. Soc.*, **139**, 1963–1970 (1992).

109. R. T. Foley and T. H. Nguyen, *J. Electrochem. Soc. Electrochem. Sci. Technol.*, **129**, 464–467 (1982).

110. T. H. Nguyen and R. T. Foley, *J. Electrochem. Soc.*, **127**, 2563–2566 (1980).

111. B. Deng et al., *Appl. Surf. Sci.*, **253**, 7369–7375 (2007).

112. O. Seri and M. Imaizumi, *Corros. Sci.*, **30**, 1121–1133 (1990).

113. K. D. Ralston, T. L. Young, and R. G. Buchheit, *J. Electrochem. Soc.*, **156**, C135 (2009).

114. D.R. Egan, C. Ponce de León, R.J.K. Woodb, R.L. Jones, K.R. Stokes and F.C. Walsh, *J. Power Sources*, **236**, 293–310 (2013).

115. K. C. Emregui, *Indian Journal of Chemistry* **42**, 1035–1039 (2003).

116. M. C. J. Marker, B. Skolyszewska-Khberger, H. S. Effenberger, C. Schmetterer, and K. W. Richter, *Intermetallics*, **19**, 1919–1929 (2011).

117. O. Seri, *Mater. Sci. Forum*, **519**–**521**, 729–734 (2006).

118. S. H. Shim and T. S. Duffy, *Am. Mineral.*, **87**, 318–326 (2001).

119. D. L. a. de Faria, S. V. Silva, and M. T. de Oliveira, *J. Raman Spectrosc.*, **28**, 873–878 (1997).

120. L. V. Gasparov and D. B. Tanner, *Phys. Rev. B - Condens. Matter Mater. Phys.*, **62**, 7939–7944 (2000).

121. M. Hanesch, *Geophys. J. Int.*, **177**, 941–948 (2009).

CURRICULUM VITAE

Shengyi Li

Place of Birth: China

Education

Ph.D. Materials Science, University of Wisconsin-Milwaukee, Aug 2012 – Dec 2016
Thesis: Corrosion of Aluminum Current Collector in Cost-effective Lithium-ion Batteries

M.S. Materials Science and Engineering, China University of Petroleum, Sep 2009 – Jun 2012
Thesis: Corrosion Behavior of Nickel-based Alloys in High Temperature and High Pressure H_2S Environment

B.E. Materials Science and Engineering, China University of Petroleum, Sep 2005 – Jul 2009

Project Experience

Screening of Additives Products in Lead Acid Battery Electrodes
Contribution: Developed, constructed and improved electrochemical test approaches for fast analysis on the gassing performance of chemical additives with different surface chemistries. Successfully screened the best-performing chemicals that enhance the dynamic charge acceptance of cathode among hundreds of products by statistical data analysis.

Polymer Solar Cell Incorporated with CuO Nanoparticles
Contribution: Performed materials characterization on nanoparticle enhanced solar cell structures using characterization tools such as SEM, EDX, DSC, AFM and XRD.

Professional Experience

Hitachi America, Ltd
Materials Research and development Intern, Jul 2016 – Dec 2016
- Designing advanced processing and joining techniques of dissimilar lightweight automotive materials, including aluminum alloys, magnesium alloys and 3-D printed carbon fiber reinforced polymer composites.
- Plant manufacturing support by materials characterization and failure analysis on prototypes

University of Wisconsin-Milwaukee
Lab Manager and Teaching Assistant, Aug 2012 – Jan 2016
- Achieved top instructor scores in college wide evaluation.
- Improved lab efficiency by scheduling proactive trainings, specifying lab documents on testing procedure, lab-activity tracking and routine maintaining-troubleshoot on equipment functions

Beijing Laboratory of Failure, Corrosion and Protection of Oil/Gas Facilities
Research Technician, Sep 2010 – Sep 2011
- Accomplished statistical analysis on corrosion-resistance and mechanical property for over 300 batches of low carbon steels products used in oil and gas industry by NACE and ISO standards
- Drafted assessment documents for customer and provided technical support for the materials selection process of the West-East Gas Pipeline Project in China

Publications

1. **S.Y. Li**, B.C. Church, Effect of aqueous-based cathode slurry pH and immersion time on corrosion of aluminum current collector in lithium-ion batteries. Materials and Corrosion. 67(9): pp978-987, (2016)

2. Aruna Wanninayake, **Shengyi Li**, Benjamin Church, Nidal Abu-Zahra. "Electrical and Optical Properties of Hybrid Polymer Solar Cells Incorporating Au and CuO Nanoparticles", AIMS Materials Science, 3(1): pp35-50, (2016)

3. Aruna P. Wanninayake, **Shengyi Li**, Benjamin C. Church, Nidal Abu-Zahra, Thermal Annealing on P3HT/PC70BM Solar Cells Incorporated with Au and CuO Nanoparticles. International Journal of Renewable Energy Research 5(4): pp1080-1091, (2015)

4. Aruna Wanninayake, Subhashini Gunashekar, **Shengyi Li**, Benjamin Church, Nidal Abu-Zahra. "CuO based Bulk Hetero-junction Solar cells: Investigations on Morphology and Performance", J. Sol. Energy Eng. 137(3), (2015)

5. Aruna P. Wanninayake, Subhashini Gunashekar, **Shengyi Li**, Benjamin C. Church, Nidal Abu-Zahra, "Effect of Thermal Annealing on the Power Conversion Efficiency of CuO-Bulk Heterojunction P3HT/ PC70BM Solar cells", J. Sustainable Energy Eng.3(2): pp107-126, (2015)

6. A. Wanninayake, S. Gunashekar, **Shengyi Li**, B. Church, N. Abu-Zahra. Performance enhancement of polymer solar cells using copper oxide nanoparticles. Semiconductor Science and Technology. (30), (2015).

7. S. Zheng, Y. Qi, C. Chen, **S.Y. Li**. Effect of hydrogen and inclusions on the mechanical properties and fracture behavior of A350LF2 steel in wet H_2S environment. Corrosion Science, 60: pp59–68, (2012)

Skills

Materials characterization tools such as SEM, EDS, XPS, XRD, DSC, TGA, Raman, FTIR, ICP, Mechanical property measurement, Electrochemical Testing, Reliability life data analysis NACE/ISO/ASTM standards and specifications, MS Office, Origin, SolidWorks, Matlab

Honors and Awards

NACE (National Association of Corrosion Engineers) Chicago Section Scholarship	Jan 2016
CEAS Dean's Scholarship, University of Wisconsin-Milwaukee	Jan 2014

Activities and Societies

Active Member of National Association of Corrosion Engineers	2009 – Now
Active Member of Electrochemical Society	2013 – Now
Volunteer of Beijing Olympic Game	